Imperial College of Science, Technology and Medicine
Department of Electrical and Electronic Engineering
Centre for Bio-Inspired Technology

Integrated Circuit & System Design for Concurrent Amperometric and Potentiometric Wireless Electrochemical Sensing

Daryl Ma

July 2022

Submitted in part fulfilment of the requirements for the degree of
Doctor of Philosophy of Imperial College London

Declaration of Originality

I hereby declare that this thesis and the work reported herein was composed by and originated entirely from me. Information derived from the published and unpublished work of others has been appropriately referenced. Any contribution made to this research by others is explicitly acknowledged in the text.

Copyright Declaration

The copyright of this thesis rests with the author. Unless otherwise indicated, its contents are licensed under a Creative Commons Attribution-NonCommercial 4.0 International Licence (CC BY-NC).

Under this licence, you may copy and redistribute the material in any medium or format. You may also create and distribute modified versions of the work. This is on the condition that: you credit the author and do not use it, or any derivative works, for a commercial purpose.

When reusing or sharing this work, ensure you make the licence terms clear to others by naming the licence and linking to the licence text. Where a work has been adapted, you should indicate that the work has been changed and describe those changes.

Please seek permission from the copyright holder for uses of this work that are not included in this licence or permitted under UK Copyright Law.

Abstract

Complementary Metal-Oxide-Semiconductor (CMOS) biosensor platforms have steadily grown in healthcare and commerial applications. This technology has shown potential in the field of commercial wearable technology, where CMOS sensors aid the development of miniaturised sensors for an improved cost of production and response time. The possibility of utilising wireless power and data transmission techniques for CMOS also allows for the monolithic integration of the communication, power and sensing onto a single chip, which greatly simplifies the post-processing and improves the efficiency of data collection.

The ability to concurrently utilise potentiometry and amperometry as an electrochemical technique is explored in this thesis. Potentiometry and amperometry are two of the most common transduction mechanisms for electrochemistry, with their own advantages and disadvantages. Concurrently applying both techniques will allow for real-time calibration of background pH and for improved accuracy of readings. To date, developing circuits for concurrently sensing potentiometry and amperometry has not been explored in the literature. This thesis investigates the possibility of utilising CMOS sensors for wireless potentiometric and amperometric electrochemical sensing.

To start with, a review of potentiometry and amperometry is evaluated to understand the key factors behind their operation. A new configuration is proposed whereby the reference electrode for both electrochemistry techniques are shared. This configuration is then compared to both the original configurations to determine any differences in the sensing accuracy through a novel experiment that utilises hydrogen peroxide as a measurement analyte. The feasibility of the configuration with the shared reference electrode is proven and utilised as the basis of the electrochemical configuration for the front end circuits.

A unique front-end circuit named DAPPER is developed for the shared reference electrode topology. A review of existing architectures for potentiometry and amperometry is evaluated, with a specific focus on low power consumption for wireless applications. In addition, both the electrochemical sensing outputs are mixed into a single output data channel for use with a near-field communication (NFC). This mixing technique is also further analysed in this thesis to understand the errors arising due to various factors. The system is fabricated on TSMC 180nm technology and consumes 28μW. It measures a linear input current range from 250pA - 0.1μW, and an input voltage range of 0.4V - 1V. This circuit is tested and verified for both electrical and electrochemical tests to showcase its feasibility for concurrent measurements.

This thesis then provides the integration of wireless blocks into the system for wireless powering and

data transmission. This is done through the design of a circuit named SPACEMAN that consists of the concurrent sensing front-end, wireless power blocks, data transmission, as well as a state machine that allows for the circuit to switch between modes: potentiometry only, amperometry only, concurrent sensing and none. The states are switched through re-booting the circuit. The core size of the electronics is 0.41mm^2 without the coil. The circuit's wireless powering and data transmission is tested and verified through the use of an external transmitter and a connected printed circuit board (PCB) coil.

Finally, the future direction for ongoing work to proceed towards a fully monolithic electrochemical technique is discussed through the next development of a fully integrated coil-on-CMOS system, on-chip electrodes with the electroplating and microfludics, the development of an external transmitter for powering the device and a test platform. The contributions of this thesis aim to formulate a use for wireless electrochemical sensors capable of concurrent measurements for use in wearable devices.

Acknowledgements

Undertaking the PhD has been a challenge that in hindsight has been one of the best experiences in my life. Personally, I have grown in both my confidence to deliver technical material, and the depth in which I am now expected to cover when discussing such topics. This growth can be attributed to both my supervisors (and research Mum and Dad), Dr Sara Ghoreishizadeh and Professor Pantelis Georgiou.

I would first thank Sara for my time back as a final year undergraduate student, clumsily rushing for deadlines and running experiments recklessly. Your supervision was key in driving that project into a publication, which ultimately led to me doing a PhD. Your constant drive for improvement has inspired my work, and generosity in introducing your team in UCL to help me along the way has led me to the culmination of my PhD. Working under Pantelis as a PhD student has also been an experience that is probably one of a kind. I've had the opportunity to explore so many different ideas under you, and it's been liberating having the freedom to think out of the box. The group you've created is the best group of people I've ever worked with, and this is in no small part to your supervision. Sara & Pantelis, words cannot express how much I appreciated your guidance these past 4 years. Thank you.

Special thanks also goes out to both my examiners, Professor Hadi Heidari and Professor Tim Constandinou for reading this thesis. The feedback you've both provided has helped improve this thesis tremendously. Particularly to Tim who has been through both my late stage review as well as correcting this thesis(till 2am at night) to its final form - really appreciate the time and effort. Been great working with you for the full custom course and planning events for CAS!

I would also like to thank all the students who I've supervised and learnt from over the past 3 years; Yaohua Zhang, Yiyang Chen, Siyuan Feng, Sophia Wang, Keming Chen, Tingyu Wang, Isabella Breslin, Xu Yuting, Shaheer Mapara, Abdullah Ehsan and Giuliana Emmolo. My research project is where it is now due to their contribution, and I am grateful to them.

The really important people of CAS - Wiesia, Iza, Christos and Joseph for their support with so many CAS events. I don't know what I would do without you. Last but not least, the gang from CBIT. I will miss everyone, but special thanks to the hardware team: Miscourides, Matthew, Miguel, Junming, Lei, Nic, Stefan, Lewis, Prateek and Costanza. Meetings with you on every alternate Friday was really fun. Particular thanks goes to Peilong who has saved me again and again with his wireless power expertise; To my seat buddies Khalid and Kat for taking all the nonsense I get up to; To the rest, for the drinks every Friday and possibly Wednesdays - it was something to look forward to at the end of a dreary week. Looking forward to the next away day with everyone!

To those who I've worked with in various forms from the EEE Department - Prof Tony who's been like a research Grandpa with all his advice he's given to me, Adria who's been a great friend, Anderson, Clare and Lina who have helped me out tremendously with the administrative tasks with the committee, to the friends I made in Germany on the research trips just before the pandemic hit - I can't thank you enough. To the group in UCL - Kerim, Atal and Minghao. Thanks for hosting me every time I arrived and always being so welcoming.

I've also had the chance to experience a social life (surprise!) outside the PhD.

The EEE PhD committee - Jochen, Alicia, Daphne, Maria, Brett and Jiyu. I took up the role because I thought it would be fun, and it was honestly pretty fun. The christmas parties and the debates over what the college needed were enlightening to me, as much as the free drinks we used to have after each pizza session. Thanks for helping me get so many things done especially during the transitioning phase to the lockdown. It was a pleasure working with everyone. Teaching at the graduate school was also a fascinating experience, especially with Marie and Richard. Thank you both for making the experience of teaching PhDs a pretty easygoing one. Finally, playing squash with Fan, Mark and Alex in the mornings was definitely the only way to make it into college at 6. I was really sleepy but it was great.

And to my family. Mum, Dad, Cheryl and Afian. Thanks for all the support you've provided over the years, and apologies for all the missed calls and messages. The pandemic has put things in perspective to a certain extent, and I hope to spend more time with everyone in the future. I owe you everything I have and I love you all very much.

Contents

Abstract **4**

Acknowledgements **7**

1 Introduction **21**

1.1 Wireless Electrochemical Sensors . . . 22
1.2 Motivation . . . 23
1.3 Research Objectives . . . 25
1.4 Report Structure . . . 27
1.5 Publications . . . 27
1.5.1 Conference . . . 27
1.5.2 Journal . . . 28

2 Background **31**

2.1 Applications for Wireless Electrochemical Sensing . . . 31
2.1.1 Concurrent Sensing of Analytes . . . 32
2.2 Electrochemical Sensing of Potentiometry and Amperometry . . . 33
2.2.1 Electrodes . . . 33
2.2.2 Potentiometry . . . 34
2.2.3 Amperometry . . . 35
2.2.4 Reference Electrode . . . 35
2.3 Sensor Front End Topologies . . . 37
2.3.1 Electrode Requirements . . . 37
2.3.2 Potentiometric Front End Circuits . . . 38
2.3.2.1 Potentiometric Front End Configuration . . . 38
2.3.2.2 Potentiometric Read Out Circuits . . . 38
2.3.2.3 Comparison of Potentiometric Topologies . . . 41
2.3.3 Amperometric Front End Circuits . . . 41
2.3.3.1 Potentiostat . . . 42
2.3.3.2 Amperometric Read Out Circuits . . . 43

2.3.3.3 Current to Frequency Converters . . . 44
2.3.3.4 Comparison of Current to Frequency converters . . . 46
2.4 Wireless Powering on CMOS . . . 46
2.4.0.1 Wireless Power/Data Management System Overview . . . 48
2.4.1 Inductive Receiver Coil . . . 48
2.4.1.1 Prior Work on Wirelessly Powered Coil on Chips . . . 50
2.4.2 Rectifier Architectures . . . 53
2.4.3 Bandgap Reference Architectures . . . 58
2.4.4 Low Dropout Regulator Architectures . . . 59
2.4.5 Power-On-Reset . . . 62
2.4.6 Load Shift Keying . . . 63
2.5 Chapter Summary . . . 64

3 Concurrent Sensing of Amperometry and Potentiometry 73

3.1 Experiment Design and Materials . . . 73
3.1.1 Materials . . . 73
3.1.2 Equipment . . . 74
3.1.3 IrOx Electrode Fabrication . . . 74
3.1.4 Sensing Circuitry . . . 74
3.2 Experimental Results . . . 75
3.2.1 Combined vs separate measurement: sensor sensitivity and correlation . . . 75
3.2.1.1 Potentiometric . . . 75
3.2.1.2 Amperometric . . . 76
3.2.2 Combined Configuration: Concurrent measurements for varying pH and H_2O_2 concentrations . . . 76
3.2.2.1 Amperometric Measurements . . . 77
3.2.2.2 Potentiometric Measurements . . . 77
3.3 Analysis and Discussion . . . 79
3.3.1 Comparison of Separate vs Combined . . . 79
3.3.2 Potentiometry with Cell Current . . . 79
3.4 Chapter Summary . . . 80

4 DAPPER: A Low Power, Dual Amperometric and Potentiometric Single-Channel Front End 83

4.1 System Design . . . 83
4.1.1 Amperometric Circuit . . . 85
4.1.2 Potentiometric Circuit . . . 86
4.1.3 Mixing the signals . . . 86
4.1.4 Amplifier . . . 87
4.2 Simulation Results . . . 87
4.3 Electrical Measurements . . . 88
4.3.1 Experimental Setup . . . 89
4.3.2 Focused-Ion Beam (FIB) Milling of Tahu . . . 89
4.3.3 Measurements . . . 90
4.4 Electrochemical Measurements . . . 92
4.4.1 Test Method . . . 92
4.4.2 Individual Readings . . . 92
4.4.3 Concurrent Readings . . . 94
4.5 Analysis . . . 95
4.6 Data Transmission Error Analysis . . . 96
4.6.1 D Flip-flop mixer . . . 96
4.6.1.1 Error resulting from varying input frequency ratios . . . 97
4.6.2 Experimental Set-Up . . . 98
4.6.2.1 Results and Analysis . . . 100
4.6.2.2 Power Consumption and Error Trade-Off . . . 101
4.7 Chapter Summary . . . 102

5 SPACEMan: Wireless SoC for Concurrent Potentiometry and Amperometry 105

5.1 Introduction . . . 105
5.2 System Architecture . . . 105
5.3 Implementation . . . 106
5.3.1 Concurrent Amperometric and Potentiometric Sensing Front End . . . 106
5.3.2 State Machine and Downlink Communication . . . 107
5.3.3 Power Management System . . . 108
5.3.3.1 Rectifier Topology . . . 109
5.3.3.2 BGR Topology . . . 110
5.3.3.3 LDO Topology . . . 111
5.3.4 Data Management . . . 112

5.4 Simulation Results . . . 113
5.5 Measurements . . . 114
5.5.1 Experimental Setup . . . 114
5.5.2 Electrical Measurements . . . 114
5.5.3 Electrochemical Measurements . . . 116
5.6 Chapter Summary . . . 117

6 Conclusion **121**
6.1 Original Contributions . . . 121
6.2 Ongoing Work . . . 122
6.2.1 Integration for in-vivo tests . . . 122
6.2.2 Electroplating and Microfludics . . . 122
6.2.3 Transmitter . . . 123
6.2.4 Platform . . . 123
6.3 Final Thoughts . . . 125

List of Tables

2.1 Comparison of potentiometric read-out topologies 40
2.2 Comparison of Current-to-frequency converters in the literature 46
2.3 Comparison of different types of coil implementations, and their various efficiencies . . 49
2.4 Comparison of On-Chip Coil Wireless Power Implementations 55
2.5 Comparison of Bandgap Reference Circuit Implementations 60

3.1 pH difference between measured and control results 78

4.1 Comparison of DAPPER with state-of-the-art 102

5.1 Performance Comparison of Various Rectifier Topologies 110
5.2 Comparison of Spaceman with state-of-the-art 119

List of Figures

1.1 Total value of investment in health tech and digital health raised over the past 7 years, with a 2.8 times increment in the past 3 years. Taken from [1] 21

1.2 Figure from Manickam et al. describing a CMOS integrated biosensor. Taken from [4]. 22

1.3 Example of a wirelessly powered sensor embedded in a contact lens. Taken from [18]. 23

1.4 Example applications for a monolithic chip in various scenarios. 24

1.5 Proposed System for the Wireless Monolithic Electrochemistry Platform 24

1.6 Thesis Organisation 26

2.1 Reconfigurable electrochemical circuit designed by Sun et al, capable of switching between potentiometric, amperometric and impedance spectroscopy. Taken from [11]. . 33

2.2 Simplified Randles Half-Cell Model that describes the electrode-electrolyte interface of a single electrode 34

2.3 Potentiometry set-up with a graphical description of the junction potential of an iridium oxide pH electrode 34

2.4 I-V curves for various materials - Non-polarisable, linear (Polarisable) or sensitive (Highly Polarisable). 36

2.5 Literature Review Mindmap for sensing topologies 37

2.6 Left: Conventional potentiometric front end. Right: Unconventional potentiometric front end. 38

2.7 Schematic of the voltage-to-frequency converter for a 0-10mV input described in [35]. This is notable in particular for their low input voltage range of 0-10mV. 39

2.8 Schematic of the potentiometric front end circuit described by Valero et al. [38]. . . . 40

2.9 Schematic of the potentiometric front end circuit described by Azcona et al. [39]. . . . 41

2.10 Three types of potentiostat configurations. 42

2.11 Example of a fully differential potentiostat described in [51]. 43

2.12 Example current conveyor circuit described by Ahmadi et al. [53] 43

2.13 Basic transimpedance amplifier circuit from Razavi et al. [58] 44

2.14 Schematic of the current to frequency converter circuit described in [62]. 45
2.15 Current starved ring oscillator utilised in [54]. 46
2.16 Inductive Coupling with Power and Data Transmission. Taken from [69] 47
2.17 Power and Data Management Block Components 48
2.18 Mindmap of various wireless power block toplogies 49
2.19 Illustration of various coils (a) around CMOS, (b) above CMOS and (c) in CMOS. Taken from [73] 49
2.20 Wireless energy harvesting chip developed by Rahmani et al. Taken from [75]. 50
2.21 Wireless circuit with digital adaptation designed by Zargham et al. Taken from [76]. . 51
2.22 433MHz wireless chip that employs adaptive matching with a frequency range. Taken from [77]. 51
2.23 Coil-On-Chip System designed by Nazari et al. Taken from [55]. 51
2.24 Glucose contact lenses system developed by Liao et al. Taken from [54]. 52
2.25 Alcohol Biomote developed by Jiang et al. Taken from [12]. 52
2.26 Demonstration of half-wave and full-wave rectification 54
2.27 Different rectifier topologies in CMOS. 57
2.28 Demonstration of a bootstrapped capacitor rectifier circuit that reduces V_{th}. 58
2.29 Fully CMOS bandgap reference described by Giustolisi et al. Taken from [101]. 59
2.30 Current mode bandgap reference described by Boni et al. Taken from [102]. 59
2.31 Bandgap reference described by Lee et al. Taken from [103]. 60
2.32 High PSRR bandgap reference described by Li et al. Taken from [104]. 61
2.33 Low Dropout Regulator Example 61
2.34 Basic RC Power-On-Reset Circuit adapted from [114] 62
2.35 Power on reset(POR) circuit utilised in this work. 63
2.36 Digital modulation examples. 63

3.1 Experiment Circuitry employed for this experiment. 75
3.2 Separate vs Combined potentiometric readings. 76
3.3 Separate vs Combined amperometric readings averaged across three trials. 77
3.4 A: Combined amperometric readings for cell current. B: Combined potentiometric measurements of pH values of buffers. 78

4.1 The block diagram showcasing the circuit in DAPPER, the proposed dual amperometric and potentiometric front end 84

4.2 Timing Diagram of Amperometric Circuit 84

4.3 Potentiometric Frontend Consisting of Current Starved Oscillator and Differential Pair . 86

4.4 Mixing Timing Diagram with the amperometric output, potentiometric output, and the mixed signals obtained, along with the error $t_e - t_a$ 87

4.5 A:Output frequency of amperometric circuit. B: Output frequency of potentiometric circuit. 88

4.6 Layout of DAPPER 89

4.7 Simulation of the output voltages for an Isense = 300pA and Vsense = 0.7V. This corresponds to 5Hz and 260Hz on the D flip-flop output. 90

4.8 Fabricated DAPPER circuit highlighting the circuit area and surface bondpads. This was fabricated on TSMC180 technology. 90

4.9 Experimental Setup of the Daughterboard and Motherboard, with the wirebonded IC along with the glob topping. 91

4.10 Layout of potential milling point - the track between the comparator output and the ground buffer 91

4.11 Images taken from the Scanning Electron Microscope (SEM) displaying the milling point. 92

4.12 Experiment setup for the measurements taken. 93

4.13 Left: Scope trace of the potentiometric output. Right: Zoomed in trace of the overall system output. 93

4.14 Plot of the measured amperometric readings above and potentiometric readings below. The linear region for the amperometric readings are from 200pA to 0.1μA. 94

4.15 Experiment Circuitry employed for this experiment with the separate potentiometric and amperometric modes along with the combined setup. 95

4.16 Measurements for potentiometric and amperometric outputs along with their derived voltage and currents. 96

4.17 Left: Measured output frequencies of both the amperometric and potentiometric outputs. Right: Derived input current and voltage for added peroxide. 97

4.18 Digital mixing errors arising from either the frequency ratio or the phase. 98

4.19 VHDL test setup. 99

4.20 Possible error arising from the synchronisation of the input signal with the clock. This error can be alleviated with a higher system clock frequency. 99

4.21 Timing Diagram showing the pulse counting process that determines the frequency values of the fast and slow frequency signals. 100

4.22 Error curves obtained from the experimental setup. (A) shows the average error calculated, (B) the maximum error, and (c) the minimum error. Taken from [3]. 100

4.23 Power vs Error trade off plot. Taken from [3]. 101

5.1 System Architecture of SPACEMan. 106

5.2 DAPPER system architecture for dual amperometric and potentiometric sensing. 106

5.3 Post-layout simulation of how the states are triggered. 107

5.4 Simulation of various rectifier topologies [2] 109

5.5 Bandgap Reference Circuit used in this work. Taken from [2] 110

5.6 Proposed Self-Tuned LDO circuit 111

5.7 Simulated line transient response of the conventional LDO vs self-tuned LDO circuit, with the voltage plot above and current plot below. 111

5.8 Layout of SPACEMan presenting the BGR, LSK, LDO, Rectifier Bridge and Sensor Front End. Note the relative size of C_{R1} compared to the rest of the electronics. 112

5.9 Timing Diagram of the first 26μs upon startup showing the most important voltages in the power management circuit at startup. 112

5.10 Simulated voltage levels at the input and output of the state machine from start up to t=600ms. 113

5.11 Micrograph of Spaceman fabricated in TSMC180BCD technology along with the bonded pads. 114

5.12 Experimental setup for Spaceman consisting of the transmitter. 115

5.13 Left: Overall setup of experiment. Right: Distance measurements. 116

5.14 Different voltage supplies captured in Spaceman. 116

5.15 Left: Frontend Tests for Spaceman. Right:Zoomed-in image of the amperometry and LSK showing the frequency halved by the D flip-flop mixing. 117

5.16 Measurements taken for the LSK output signals at the transmitter. 117

5.17 Electrochemical Measurement setup showcasing the pH solution under test on a magnetic stirrer, the ISE and RE electrodes connected to the motherboard 118

5.18 Frequency measured at the output of the transmitter of various pH values. 118

6.1 Left: CMOS integrated potentiostat developed for on-chip sensing by Nazari et al. Taken from [1]. Right: Soft epidermal sweat patch developed for sweat collection. 123

6.2 System diagram and image of the in-development portable transmitter. 124

6.3 Rasperry PI based platform for use with Spaceman Testing 125

6.4 Dexcom G6 glucose sensor starter kit from [2]. 125

Abbreviations

AC	**A**lternating **C**urrent
ADC	**A**nalog to **D**igital **C**onverter
AFE	**A**nalog **F**ront **E**nd
AgCl	Silver Chloride
ALDO	**A**nalog **L**ow **D**ropout **R**egulator
ASK	**A**mplitude **S**hift **K**eying
ATP	**A**denosine **Tri**p**h**osphate
BGR	**B**and **G**ap **R**eference
CBIT	**C**entre for **B**io-**I**nspired **T**echnology
CDMA	**C**ode **D**ivision **M**ultiple **A**ccess
CE	**C**ounter **E**lectrode
CMOS	**C**omplementary **M**etal **O**xide **S**emiconductor
CNF	**C**arbon **N**ano **F**ibre
DC	**D**irect **C**urrent
DLDO	**D**igital **L**ow **D**ropout **R**egulator
DNA	**D**eoxyribo **N**ucleic **A**cid
FDMA	**F**requency **D**ivision **M**ultiple **A**ccess
FSK	**F**requency **S**hift **K**eying
GUI	**G**raphical **U**ser **I**nterface
H_2O_2	Hydrogen Peroxide
IC	**I**ntegrated **C**ircuit
Ir	Iridium
IrOx	Iridium Oxide
ISE	**I**on **S**ensitive **E**lectrode
ISFET	**I**on **S**ensitive **F**ield **E**ffect **T**ransistor
ISM	**I**ndustrial, **S**cientific and **M**edical
ISO	International Organisation of Standards
LC	Inductor-Capacitor
LDO	**L**ow **D**ropout **R**egulator
LSK	**L**oad **S**hift **K**eying
MOSFET	**M**etal - **O**xide -**S**emiconductor **F**ield **E**ffect **T**ransistor
NMOS	**N**-channel **M**etal **O**xide **S**emiconductor
PCB	**P**rinted **C**ircuit **B**oard
PCE	**P**ower **C**onversion **E**fficiency

PMOS	**P**-channel **M**etal **O**xide **S**emiconductor
POR	**P**ower **O**n **R**eset
PSK	**P**hase **S**hift **K**eying
PSRR	**P**ower **S**upply **R**ejection **R**atio
Pt	Platinum
PTE	**P**ower **T**ransfer **E**fficiency
PTAT	**P**roportional **T**o **A**bsolute **T**emperature
RE	**R**eference **E**lectrode
RF	**R**adio **F**requency
RLC	Resistor - Inductor - Capacitor
RTL	**R**eal-**T**ime **L**ogic
Rx	**R**eceiver
SR	**S**et **R**eset
SCE	**S**tandard **C**alomel **E**lectrode
SEM	**S**canning **E**lectron **M**icroscope
SHE	**S**tandard **H**ydrogen **E**lectrode
SiO_2	Silicon Dioxide
SOC	**S**ystem **O**n **C**hip
TIA	**T**rans **I**mpedance **A**mplifier
Tx	**T**ransceiver
USB	**U**niversal **S**erial **B**us
VCO	**V**oltage **C**ontrolled **O**scillator
VCR	**V**oltage **C**onversion **R**atio
VHDL	**V**erilog **H**igh-level **D**escription **L**anguage
WE	**W**orking **E**lectrode

Chapter 1

Introduction

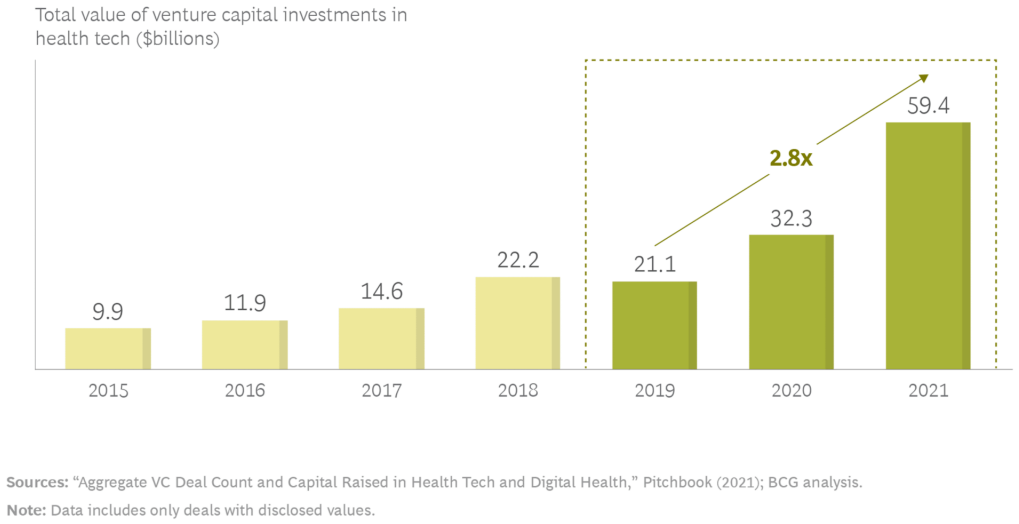


Figure 1.1: Total value of investment in health tech and digital health raised over the past 7 years, with a 2.8 times increment in the past 3 years. Taken from [1]

The application of Complementary Metal-Oxide-Semiconductor(CMOS) platforms in biosensors has steadily grown in healthcare and commercial applications [2]. This has shown clear potential in the field of commercial wearable technology due to the possibility of miniaturisation, along with improved cost of production and response time. With the Covid-19 pandemic bringing to the fore the importance of accurate and reliable diagnostics, it is key to begin looking into the development of a post-pandemic world for our future generations. This pandemic has highlighted overcrowding in hospitals due to inadequate hospital capacity or poor flow processes, and is an institution-wide issue [3]. A recent article by Boston Consulting Group has pressed on the need to develop remote-management technologies to monitor patients outside the traditional care settings for avoiding costly treatments, and raised the example of three hospitals in South London utilising remote-monitoring technology to observe patients with rheumatoid arthritis at home for reduced hospital visits [1]. Their research estimates an increased growth in investment across health tech in the past few years as shown in Fig. 1.1, and suggests that this adoption will continue beyond the resolution of the pandemic.

A recent call to action for the development of wearable sensors for remote patient monitoring and

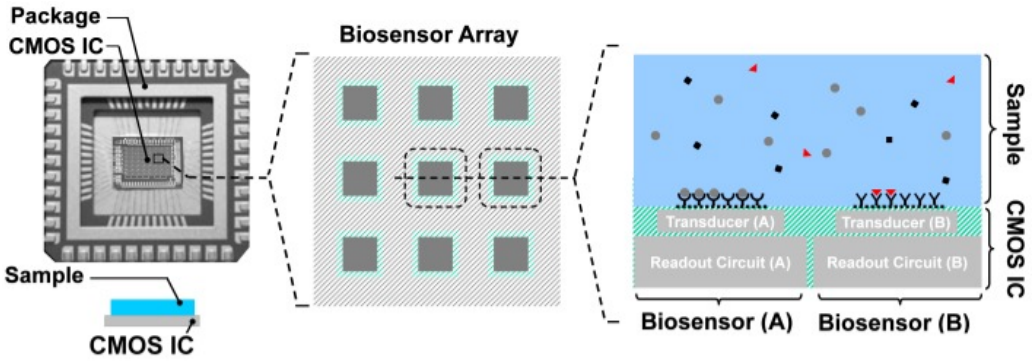


Figure 1.2: Figure from Manickam et al. describing a CMOS integrated biosensor. Taken from [4].

virtual assessments allows for a more nuanced monitoring of population health [5]. A review by Cheng et al. [6] describes the various possible wearable sensors that could be used for this purpose, from flexible electronic skins, smart bandages and contact lenses. Individual metrics measured with wearables could provide a possible indicator for the presence of an infection, while having the ability to monitor health symptoms in the population allows transmission rates to be tracked in real-time more accurately. However, challenges in integrating CMOS biosensors for commercialisation still remain at large. To utilise these CMOS sensors in biomedical applications, it is important that these sensors remain electrochemically stable and biocompatible at a low cost [7]. As CMOS technology itself is not biocompatible, lowering the costs of post-processing is vital for biomedical applications.

Developing wireless electrochemical sensors leads to the alleviation of this challenge. Without the need for these CMOS chips to be connected via bond pads for data or power transmission, and on-chip electrodes for the detection of biomarkers, these monolithic sensors give rise to the possibility of applying easy-to-use sensors that can be embedded into wearables.

1.1 Wireless Electrochemical Sensors

Electrochemical sensors are devices that obtain information from a medium through the means of an electrochemical transducer coupled with a chemically selective layer [8]. This may be in the form of a voltage or current value that varies depending on the concentration of the measured chemical. These biosensors have made enormous progress in recent years due to their high sensitivity, specificity and their ability for rapid and inexpensive detection in small sample volumes [9].

Moreover, they lend themselves for integration into lab-on-chip platforms and allows for the monitoring of the concentration of target analytes in real time [10], qualities that are further highlighted in emerging health crises such as infectious diseases [11].

Two of the most common transduction mechanisms for electrochemical sensing are potentiometry and amperometry. With the emergence of ion-sensitive electrodes with low detection limits up to ultra trace levels have given rise to the importance of potentiometric sensing [12]. Additionally, with ongoing research on miniaturising these electrodes further, potentiometry allows for the possibility of

low ion measurement values in tiny sample sizes for ions such as potassium, sodium, pH values and even bacteria or toxicities [13] [14].

On the other hand, amperometry is a measurement technique usually applied for the detection of biomolecules such as lactate, ATP, glucose and cholesterol [15]. In addition to this, it has also been extensively applied for gas sensors, most recently in the field of low-cost air quality control [16]. Amperometry is also particularly relevant in the field of glucose sensing, where numerous amperometric sensors are utilised [17].

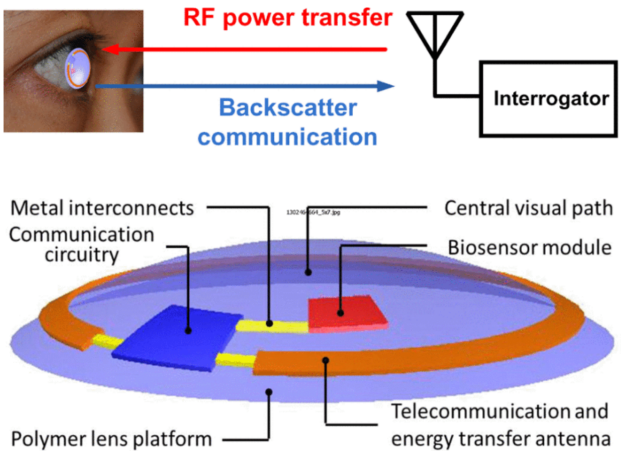


Figure 1.3: Example of a wirelessly powered sensor embedded in a contact lens. Taken from [18].

A *wireless* electrochemical sensor obtains information from its local environment and transmits this analytical data to a remote device [19]. This can be through the form of a wireless point to point link such as Near-Field Communications (NFC), or in the form of a wireless sensor network, where the device is simply one of many employed in the field to gather information.

Monolithic integration of a wireless electrochemical sensor implies that all communication, powering and sensing circuitry are integrated into a single chip. With the emerging trends of Sensor Internet of Things and the modern adoption of wireless communication techniques such as bluetooth and NFC, wireless chemical sensing has the potential to realise mass market adoption of chemical analytics. This brings into play new possibilities for healthcare wearables, enabling new approaches towards continuous monitoring of health. Wireless electrochemical sensors also allow for chemical analytics at the point-of-sample, and reduces the reliance on centralised analytical laboratories. This improves the efficiency of data collection, as time spent on transporting samples to-and-fro from larger laboratories are significantly reduced.

1.2 Motivation

The next generation of wireless electrochemical systems is envisioned as a chip with a fully integrated coil and on-chip electrodes. This chip itself is a device with on-chip electrodes for sensing of analytes such as glucose, lactate or pH. As shown in Figure 1.4, this can be used for point-of-sample diagnostics. This is helpful in situations where non-contact scenarios are important, particularly in the monitoring

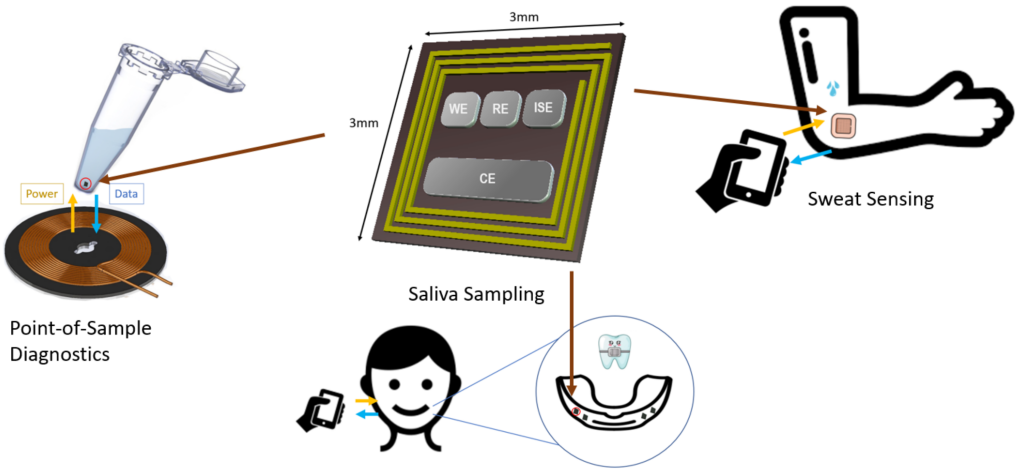


Figure 1.4: A representation of the potential monolithic chip, with applications in point-of-sample diagnostics, saliva sampling through integration into a bracket, as well as sweat sensing through a skin patch.

of infected patients. Having a wireless connection allows data to be collected much more efficiently than if a wired connection was required. This would be used once for analysis before being disposed of.

The device can also be applied to saliva sampling, particularly for the case of pH or glucose measurements for monitoring possible oral cancer symptoms. The chips can be affixed to a bracket that is then worn by a user. These chips are then powered up using a transmitter such as a smartphone, from which sampling can occur.

Finally, this system can also be embedded into skin patches for sweat sensing as a wearable device. This is potentially useful for the measurement of lactate - a particularly important biomarker for athletes, or even antibiotics for antimicrobial resistance monitoring.

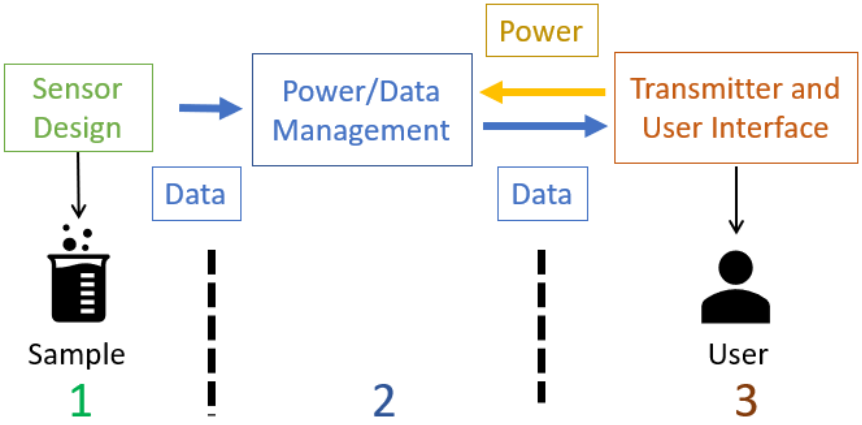


Figure 1.5: Proposed System for the Wireless Monolithic Electrochemistry Platform

A proposed system for the monolithic circuit is shown in **Figure 1.5**. There are three key design areas:

1. Sensor Design/Interface
2. Power/Data Management
3. Power Transmitter and User Interface

In this research we aim to advance the field in these three design areas. The first area would be around designing the sensor front end - a dual amperometry and potentiometry circuit. This will involve the development of the theory for the possibility of concurrent sensing utilising 4 electrodes along with the circuit design of the front end circuit. Concurrent sensing of amperometry and potentiometry will give rise to a multitude of possible configurations, and also allows for a more versatile analysis of biomarkers.

The next part of the design will look at the development of sensors with a large detection range at a low power. Once this power budget is determined, a power management block will be developed based on the requirements. The power and data management block will involve the transmission of the data collected, as well as the generation of the required power for the sensor to operate. This involves looking at various receiver coil designs, as well as the potential power budgets. Lastly, if time permits, a power transmitter circuit for the data acquisition of the received data will be designed to read and receive data from the wireless chip.

1.3 Research Objectives

The aim of this thesis is to develop the hardware capable of wireless concurrent measurements of potentiometry and amperometry. To do so first requires a thorough understanding of the concepts of the sensor chemistry behind both sensing modalities and designing tests for that purpose. The next objective would be to design a suitable front-end system capable of concurrent sensing. The validation of this system would aid the design of the final wireless power and telemetry circuit to integrate with the front-end system.

The investigation aims to answer the following key research questions:

1. How would potentiometry and amperometry electrochemical sensing be affected when done concurrently with a shared reference electrode? Utilising a new configuration for concurrent sensing brings possible challenges due to the additional of other factors such as current flow in a previously zero-current environment. The test method has to be developed as well as to trigger an observable change for both the amperometric and potentiometric sensor. The sensor configuration is key for proceeding with a concurrent sensing electrochemical system.
2. What front-end circuits would be useful for a low power sensor front-end system? To develop a wireless device, it is important to have a low powered sensor front-end circuit for both the potentiomtry and amperometry readout. This can be done through a review of front-end circuits and determining the best combination of the potentiometry and amperometry readout circuit for a low power consumption.

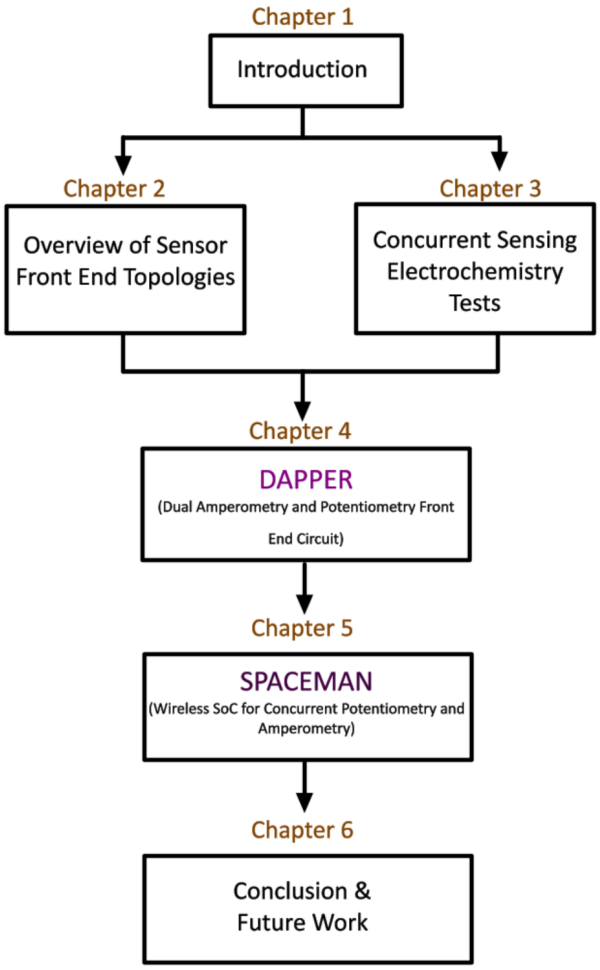


Figure 1.6: Thesis Organisation

3. What are the possible errors associated with mixing both the concurrently read signals into one output? Mixing both the potentiometric and amperometric outputs into a single output frequency allows for the data stream to be sent via NFC. However, there are associated errors that arise from this mixing process. It is important to analyse where these errors come from and characterise them.

4. What challenges are there in developing a wireless electrochemical sensor with switchable states? There are a number of key considerations that must be taken in order to design such a system for low power. Various circuit implementations are utilised to ensure the power consumption remains low. There are also challenges in developing a test system to verify the wireless power and data transmission.

5. What is the future direction for the development of the wireless electrochemical sensor? Through the thesis contribution and ongoing work, a number of possibilities are proposed for the next stage of the research process.

1.4 Report Structure

The report structure can be seen in Fig. 1.6. After the introduction in **Chapter 1**, the following chapters cover:

Chapter 2 covers the background behind the electrochemistry concepts, the sensor front-end topologies and wireless powering components. The electrochemistry concepts would go into the details about the role of the reference electrode and understanding how sharing the electrode for concurrent measurements would affect the readings. The sensor front-end topologies and wireless powering background would go through the CMOS circuits currently available in the literature. This would aid the design of both the integrated circuits (ICs) developed in this project.

Chapter 3 discusses the theory behind concurrent amperometric and potentiometric sensing from a chemical perspective, and evaluate the feasibility of a shared reference electrode topology through designed tests. These tests are specifically developed for the purpose of attaining readings from both the amperometric and potentiometric sensors, and serve to provide a basis for the electrochemical tests for the entire project.

Chapter 4 describes the design of DAPPER, a front-end system for concurrent amperometric and potentiometric sensing. This system is developed for the shared reference electrode configuration, and mixes both the output readings of amperometry and potentiometry into a single output for wireless data transmission. The fabricated IC is tested and validated through electrical and electrochemical tests. A more in-depth analysis is done into the mixing technique of the data transmission through a VHDL simulation. This provides a relationship between the error and the power consumption of the system.

Chapter 5 would discuss the overall system design for the wireless power and data transmission components and the developed system, SPACEMAN. This chapter goes into the details of the simulations for SPACEMAN to provide an understanding of the workings of the IC. The fabricated IC is validated and tested in this chapter to show the wireless power transmission and data transmission.

Chapter 6 summarises the work to date and the future work moving forward. The research contributions are described in this chapter. All ongoing work for this research project is also described to give an overview of the path to a full monolithic electrochemical sensor.

1.5 Publications

Several publications have arisen from this thesis. A list is included below.

1.5.1 Conference

D. Ma, Y. Chen, S. S. Ghoreishizadeh and P. Georgiou, "SPACEMan: Wireless SoC for Concurrent Potentiometry and Amperometry," 2021 IEEE International Symposium on Circuits and Systems (ISCAS),

2021, pp. 1-5, doi: 10.1109/ISCAS51556.2021.9401312.

D. Ma, S. S. Ghoreishizadeh and P. Georgiou, "DAPPER: A Low Power, Dual Amperometric and Potentiometric Single-Channel Front End," 2020 IEEE International Symposium on Circuits and Systems (ISCAS), 2020, pp. 1-5, doi: 10.1109/ISCAS45731.2020.9181213.

Y. Chen, **D. Ma** and P. Georgiou, "A Wireless Power Management Unit with a Novel Self-Tuned LDO for System-On-Chip Sensors," 2021 IEEE International Symposium on Circuits and Systems (ISCAS), 2021, pp. 1-5, doi: 10.1109/ISCAS51556.2021.9401217.

Y. Zhang, **D. Ma**, S. Carrara and P. Georgiou, "Design of Low-Power Highly Accurate CMOS Potentiostat Using the gm/ID Methodology," 2021 IEEE International Symposium on Medical Measurements and Applications (MeMeA), 2021, pp. 1-5, doi: 10.1109/MeMeA52024.2021.9478690.

G. Emmolo, **D. Ma**, D. Demarchi and P. Georgiou, "Multiple Input, Single Output Frequency Mixing Communication Technique for Low Power Data Transmission," 2021 IEEE International Symposium on Medical Measurements and Applications (MeMeA), 2021, pp. 1-6, doi: 10.1109/MeMeA52024.2021.9478708.

1.5.2 Journal

D. Ma, S. S. Ghoreishizadeh and P. Georgiou, "Concurrent Potentiometric and Amperometric Sensing With Shared Reference Electrodes," in IEEE Sensors Journal, vol. 21, no. 5, pp. 5720-5727, 1 March1, 2021, doi: 10.1109/JSEN.2020.3039567.

References

[1] J. Neiser et al. *Building Health Tech Advantage*. 2022.

[2] H. Li et al. "CMOS electrochemical instrumentation for biosensor microsystems: A review". In: *Sensors* 17.1 (2017), p. 74.

[3] P. McKenna et al. "Emergency department and hospital crowding: causes, consequences, and cures". In: *Clinical and Experimental Emergency Medicine* 6.3 (2019), p. 189.

[4] A. Manickam et al. "Interface design for CMOS-integrated electrochemical impedance spectroscopy (EIS) biosensors". In: *Sensors* 12.11 (2012), pp. 14467–14488.

[5] D. R. Seshadri et al. "Wearable sensors for COVID-19: A call to action to harness our digital infrastructure for remote patient monitoring and virtual assessments". In: *Frontiers in Digital Health* 2 (2020), p. 8.

[6] S. Cheng et al. "Recent Progress in Intelligent Wearable Sensors for Health Monitoring and Wound Healing Based on Biofluids". In: *Frontiers in Bioengineering and Biotechnology* 9 (2021), p. 765987.

[7] A. H. Graham et al. "Commercialisation of CMOS integrated circuit technology in multi-electrode arrays for neuroscience and cell-based biosensors". In: *Sensors* 11.5 (2011), pp. 4943–4971.

[8] S. Li. *Molecularly imprinted sensors: overview and applications*. Elsevier, 2012.

[9] A. J. Bandodkar and J. Wang. "Non-invasive wearable electrochemical sensors: a review". In: *Trends in biotechnology* 32.7 (2014), pp. 363–371.

[10] S. Carrara. *Bio/CMOS interfaces and co-design*. Springer Science & Business Media, 2012.

[11] P. Yager, G. J. Domingo, and J. Gerdes. "Point-of-care diagnostics for global health". In: *Annual review of biomedical engineering* 10 (2008).

[12] E. Bakker and E. Pretsch. "Trace level potentiometry". In: *Analytical Chemistry* 74 (2002), 420A–426A.

[13] J. Ding and W. Qin. "Recent advances in potentiometric biosensors". In: *TrAC Trends in Analytical Chemistry* (2020), p. 115803.

[14] N. Moser et al. "Complementary Metal–Oxide–Semiconductor Potentiometric Field-Effect Transistor Array Platform Using Sensor Learning for Multi-ion Imaging". In: *Analytical chemistry* 92.7 (2020), pp. 5276–5285.

[15] M. Ciobanu et al. “Glucose and lactate biosensors for scanning electrochemical microscopy imaging of single live cells”. In: *Analytical chemistry* 80.8 (2008), pp. 2717–2727.

[16] R. Baron and J. Saffell. “Amperometric gas sensors as a low cost emerging technology platform for air quality monitoring applications: A review”. In: *ACS sensors* 2.11 (2017), pp. 1553–1566.

[17] M. Diabetes. *Medtronic Enlite Glucose Sensors*. Oct. 2020.

[18] Y.-T. Liao et al. “A 3-μW CMOS Glucose Sensor for Wireless Contact-Lens Tear Glucose Monitoring”. In: *IEEE Journal of Solid-State Circuits* 47.1 (2012), pp. 335–344.

[19] P. Kassal, M. D. Steinberg, and I. M. Steinberg. “Wireless chemical sensors and biosensors: A review”. In: *Sensors and Actuators B: Chemical* (2018).

Chapter 2

Background

This chapter describes the theory behind three topics: (1) Electrochemical sensing, (2) Sensor front end topologies, and (3) Wireless powering components. Electrochemical sensing refers to an explanation behind the electrochemical techniques. The background behind the electrochemistry described in this chapter is used to inform the experiments performed for validating the shared reference electrode that is done in Chapter 3.

The next topic would cover the sensor front-end circuits necessary for the electrochemical sensor & discuss the possible applications for which the sensor can be used for. The strengths and weaknesses of each circuit is evaluated to determine the best possible choice for the front-end system. The background in this work culminated in the eventual design of the IC DAPPER in Chapter 4.

Lastly, the wireless powering components refer to the blocks utilised for wireless power and data transmission. The overview for the various circuits developed for each of the wireless blocks are key to the development of wireless IC SPACEMAN in Chapter 5.

2.1 Applications for Wireless Electrochemical Sensing

The advent of smaller transistors down to the 3nm process has brought up the possibility of developing nanometre-sized circuits to be placed on the human body[1]. These circuits can be applied to help alleviate healthcare issues in the biomedical sector through wearables or implants. Sandro et al. discusses the possibility of a future whereby $10\mu m^2$ sized CMOS circuits are designed for drinkable diagnostics[2] where they look at the future of cellular level diagnostics in healthcare applications, only possible by miniaturising circuits to the same magnitude of red blood cells.

There have been a number of wireless electrochemical sensors developed. Kim et al. designed a non-invasive alcohol monitoring wearable tattoo is designed for alcoholics [3]. This patch detects alcohol from sweat through the use of the alcohol-oxidase enzyme and the Prussian Blue electrode transducer. This sensor is then linked to a on-board flexible electronics board, from the data is transmitted via bluetooth communication to a smartphone. A carbon nanofibre (CNF) electrode array was used as a

neurotransmitter for the detection of dopamine to showcase the application of these arrays against standard carbon fibre microelectrodes [4]. These electrodes arrays were prepared on a silicon wafer, and linked to a bluetooth PCB for transmitting data. A lactate sensor is designed for use in the continuous measurement of sweat for observing endurance-based physical activities [5]. NFC is applied to transmit the information. In [6], a mouthguard is designed to monitor salivary uric acid levels. This mouth guard system detects the salivary uric acid levels in real time, and transmits this data via bluetooth to a smartphone.

These examples here showcase the versatility of analyte detection, as well as a variety of wireless transmission methods. Their applications also vary, from neural implants to in mouth sensing device, as well as a wearable tattoo patch. However, most of these methods utilise a transmitter that is generally on a PCB board, and is unwieldy as a wearable device.

Hence, a miniaturised wireless electrochemical sensor would be useful for locations not easily accessible, such as in-vitro applications. It would also be useful in cases where the sensor has to be mobile, which is the case for healthcare wearables, where a large device could impede the motion of a user. In this case, a non-obstructive sensor would be ideal. For sensors applied for in-vivo sensing, a minimally invasive biocompatible sensor would be ideal. In addition to these two examples, the miniaturisation of wireless electrochemical sensing platforms has applications for a wide range of fields such as gas monitoring systems, DNA sensing, and even food transport. This gives the opportunity to integrate miniaturised sensors in pre-existing systems with as minimal a disruption as possible.

2.1.1 Concurrent Sensing of Analytes

A key challenge in the measurement of biomolecules from biofluids is the presence of interfering molecules. Additionally, changes in environmental parameters such as temperature and pH of biofluid affects the electrochemical sensors [7]. Salivary pH follows a circadian rhythm that changes dependent on the body's dietary conditions, gastric acid reflux, diabetes or oral health situation [8]. Measuring electrochemical biomedical readings in tandem with pH measurements provides additional metrics helpful for improving the accuracy of the readings. Concurrent measurements of potentiometric and amperometric monitoring of various analytes for co-analysis allows for sensor calibration at real-time [9]. Moreover, the inherent differences of potentiometry and amperometry result in advantages and disadvantages for either technique [10]. In particular, Brunt et al. states that amperometry allows a faster measurement of glucose in flow cells, while potentiometric technique provides a lower limit of detection. The input-output characteristics of the potentiometric and amperometric sensors are also different, with potentiometry having a logarithmic response while amperometry is linear. Having the possibility of utilising both techniques allows the advantages of either technique, and provide for a more versatile analysis.

Few systems have been introduced to obtain both amperometry and potentiometry readings. For example, Sun et al [11] (Fig. 2.1) and Jiang et al [12] describe reconfigurable circuits that can be switched into potentiometric or amperometric modes at different moments in time. However, simultaneous potentiometric and amperometric readings, which is essential to capture instantaneous

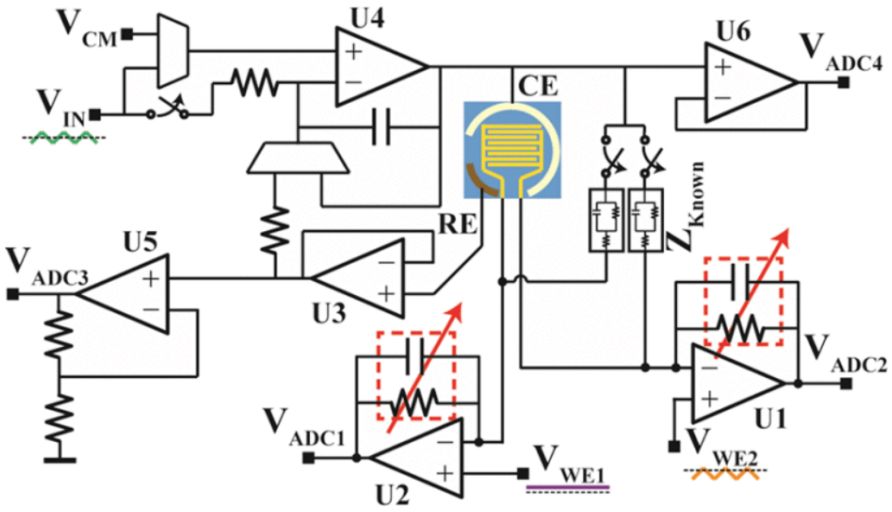


Figure 2.1: Reconfigurable electrochemical circuit designed by Sun et al, capable of switching between potentiometric, amperometric and impedance spectroscopy. Taken from [11].

changes in pH for accurate calibration and reliable analysis[13], have yet to be achieved in literature.

2.2 Electrochemical Sensing of Potentiometry and Amperometry

To describe the operation of potentiometry and amperometry, a background into the operation of electrodes and their equivalent circuits is provided. The sensing operation at the electrode as well as circuit level is then covered for both potentiometry and amperometry.

2.2.1 Electrodes

Two electrodes are employed in potentiometry, consisting of a sensing and reference electrode. The sensing electrode in this work is an ion-sensitive electrode (ISE), and serves to measure the ion concentration relative to a stable reference. The amperometric measurement typically includes three electrodes: Working (WE), Counter (CE) and a Reference electrode (RE). A potential is induced across the WE and RE, while the CE provides a steady current supply. Randles cell [14] is an equivalent circuit model for an electrode in an electrolyte and is illustrated in Fig. 2.2.

C_{dl} describes the double layer capacitance from the electrical alignment of water molecules near the electrode surface to the electrolyte. R_s is the electrolyte resistance, which is affected by electrode material, electrode construction and tissue impedance. R_P represents the charge transfer resistance at the phase boundary, which involves the electrode oxidation and reduction reactions[15].

It is not possible to measure the potential across the electrolyte and electrode, as there is no physical connection point at the electrolyte. Instead, this model describes the theoretical reactions across

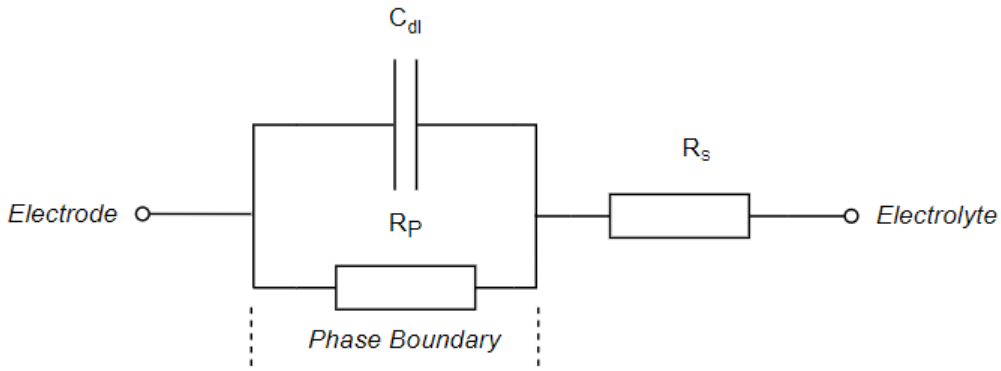


Figure 2.2: Simplified Randles Half-Cell Model that describes the electrode-electrolyte interface of a single electrode

the electrolyte and phase boundary. In order to determine the potential across a half-cell, another electrode is required as a reference with a known potential to compare any measured potential to.

2.2.2 Potentiometry

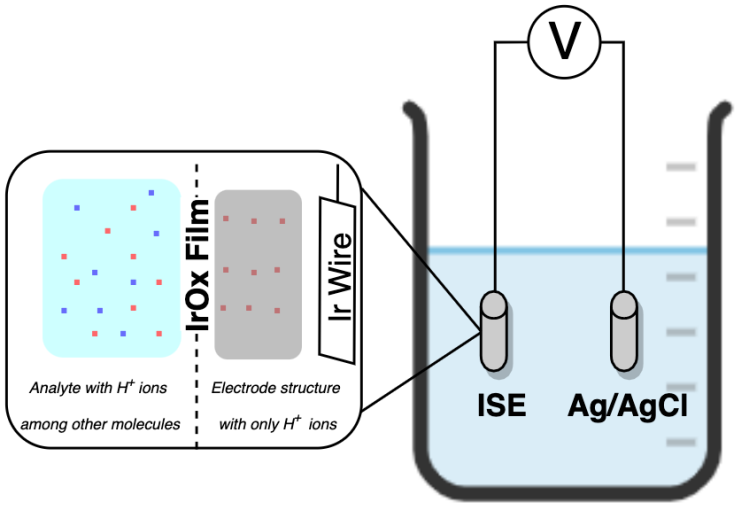


Figure 2.3: Potentiometry set-up with a graphical description of the junction potential of an iridium oxide pH electrode

As can be seen from Fig. 2.3, a junction potential arises due to the charges at the interface between an electrode and an electrolyte. Potentiometry is the measurement of this charge through the use of a high-impedance voltmeter between the sensing electrode and a RE, ensuring that no current passes through - leaving the circuit in equilibrium.

ISEs work specifically by allowing only the desired ions to be adsorbed upon the electrode surface. In particular, for metal oxide/metal oxide pH sensors such as the iridium oxide (IrOx) electrodes described in this work[16], this is dependent on the equilibrium between the oxide layers. This potential at the sensing electrode is related to the Nernst Equation for ISEs:

$$E = E^0 + \frac{2.303RT}{nF} log(A) \tag{2.1}$$

where E is the total potential in mV between the sensing and reference electrodes, E^0 the constant based on the ISE/reference pair, R is the gas constant (8.314 Joule/degree/mol), T is the absolute temperature (298.15K @ 25°C), n the ion charge sign, F the Faraday Constant (96.5K Coulombs) and ion activity [17].

In potentiometry, the circuit is kept at equilibrium and no current is flowing through the electrodes. When this equilibrium is disturbed through a variation in the potential, a current is produced based on Faraday's Law[18].

2.2.3 Amperometry

Amperometry involves the technique of applying the potentiostat to measure the concentration of a certain ion in a solution. Once a potential is induced across the RE and the WE, the detected ions diffuses towards the WE. These ions are then adsorbed onto the WE, where a redox reaction occurs. The products of the reaction then desorb away from the WE. To achieve ion-selectivity, a diffusion membrane can be introduced to limit the reaction for the desired ions[19]. The CE is utilised in this case to provide a steady current supply without affecting the potential difference - hence the term potentiostatic.

The analytical response of the sensor is the magnitude of the current between the WE and the CE. The potential of the WE is chosen such that the faradaic current is determined by diffusion instead of the kinetics of the redox reaction, which allows for a linear relation between the current and the concentration of the detection ion.

2.2.4 Reference Electrode

The RE is an electrode that has a stable and well defined potential, where all other potentials in the circuit are referenced to. Standard Hydrogen Electrode (SHE), Saturated Calomel Electrode (SCE) or the Silver/Silver Chloride Electrode (Ag/AgCl) are the most commonly used REs.

As mentioned, a current is produced when there is a variation in the potential. This current and voltage relationship causes electrode polarisation, which is the phenomena whereby the potential across the electrode-electrolyte interface varies with the current flow. Polarisation differs for various materials as shown in Fig. 2.4 - with the degree of polarisation being key to the type of electrode the material will be suitable for. Polarisation is affected by 3 factors: (1) Activation, whereby the potential difference depends upon the activation energy of the reaction; (2) Concentration, whereby the change in ion concentration varies the equilibrium potential of the reaction; (3) Ohmic, where a resistive drop across the electrolyte occurs due to the volume resistance [21]. Fig. 2.4 also displays the I-V curves for ideal REs or WEs. To measure the degree of polarisation, a potentiostat is utilised to maintain a fixed potential while measuring the current induced.

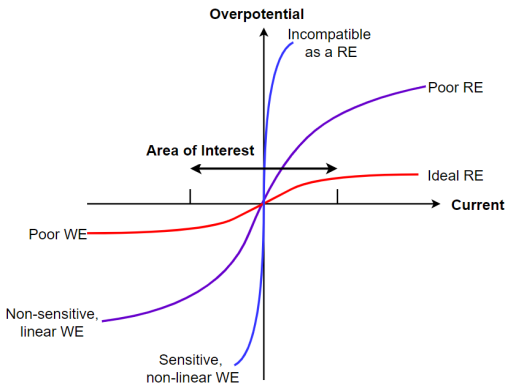


Figure 2.4: I-V curves for various materials - Non-polarisable representing a good RE, with minimal potential change across a large range of current, as well as linear (Polarisable) or sensitive (Highly Polarisable) WEs. [20]

The requirements of a RE are as follows[20]: (1) It must be non-polarisable and reversible with a high exchange current density. These allow the potential to remain constant for a large current range. (2) The reaction area should remain constant throughout the reaction, with the reaction not affecting the electrode area. (3) Lastly, the inner filling solution of the electrode should be saturated. This ensures that the concentration of the inner filling solution remains relatively stable even when the solvent evaporates - and leaves the potential constant. It also follows that a high saturation allows for a higher and stable exchange current density as shown in Fig. 2.4. This also allows the test solution to be separate from the inner filling solution, and hence the potential is as constant as possible.

Most of the characteristics of the RE such as being non-polarisable and having a constant potential is shared across the potentiometric and amperometric techniques. However, a key difference lies in their electrical control requirements (i.e. associated circuit topologies). In potentiometry (see Fig. 3.1B), the RE is connected to a low-impedance output node of an op-amp. This is key for the RE to be driven by the op-amp to a desired reference voltage. In contrast, for amperometry (see Fig. 3.1A) the RE is connected to a high-impedance input node in a positive feedback configuration. This ensures zero-current flows into the RE. As current flows from the CE, this topology ensures that the current goes directly to the WE.

For the combined configuration, the RE is connected similarly to the amperometric RE - a high-impedance connection. Although the change of RE configuration does not affect the ISE enlivenment (because RE simply provides a reference point for the measurements), the voltage between the electrode and the electrolyte at the ISE may become affected due to the current flow induced by the amperometry. Ion flow across the solution might affect the concentration across the junction potential - leading to erratic readings. We expect this to be negligible for steady state measurements. We will explore the scale of this effect in this work through carefully designed experiments. Another potential issue is the possibility of the RE voltage drifting due to the open-loop topology employed.

The effects of a controlled external current applied to potentiometric readings has been explored in [22][23][24]. The utilisation of external current has led to an improvement in the lower limit of detection for potentiometry[22] and [23]. A theoretical model described in [24] further expands upon the potential response of the ISE demonstrating that a controlled-current allowed for improved

lower limits of detections for ISE.

The amperometric measurements should be similar across both the combined and separated topologies because the addition of a passive ISE will not impact the amperometric cell.

2.3 Sensor Front End Topologies

This section would describe the various sensor front end topologies available for potentiometry and amperometry. Fig. 2.5 shows the various types of configurations available. This section would provide a background into each of the configurations along with a design rationale for determining a chosen configuration. The rest of this section further deliberates the design choices.

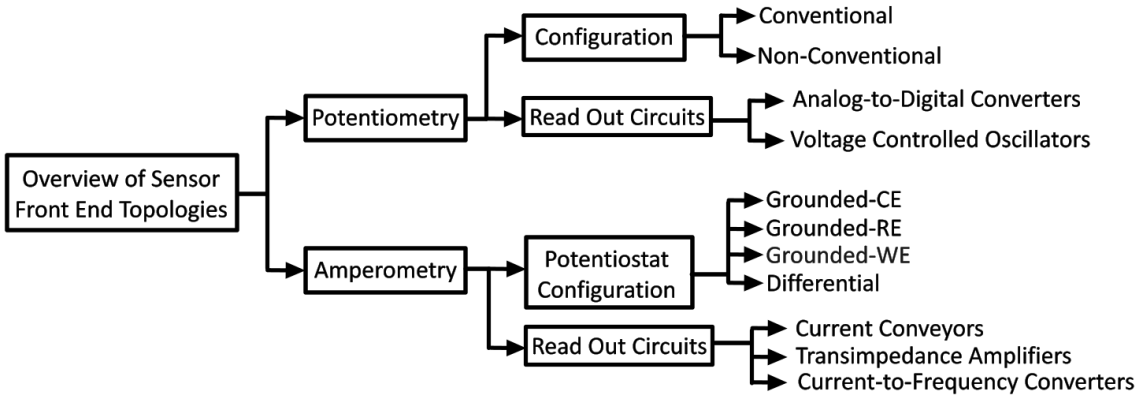


Figure 2.5: Literature Review Mindmap for sensing topologies

2.3.1 Electrode Requirements

The decision was made to focus on potentiometric and amperometric techniques due to their large range of biomarkers. In particular, potentiometric biosensors has use cases for ions such as sodium, chlorine, potassium and pH[25]. This is in the range of mediums such as sweat, saliva and interstitial fluid. On the other hand, amperometric biosensors are more suited for enzyme electrodes which measure a reactant from a reaction such as hydrogen peroxide[26]. More recently, there has been interest in aptasensors - sensors that utilise aptamers on electrode surfaces. These have been used for cardiac, alzheimer's disease, infectious diseases and cancer biomarkers[27].

The key requirements for the electrodes is biocompatibility and size. For implantable or wearable potentiometric electrodes at the desired size, Ion-Sensitive Field Effect Transistors(ISFETs) and Iridium Oxide(IrOx) [28][29][30] are the most commonly reported electrode types in literature. An ISFET array can be designed to sizes of 0.7mm x 0.4mm, which is desirable for monolithic applications[29]. However, due to the CMOS manufacturing process of ISFETs, aluminium is present in the electrodes which is a corrosive metal in the presense of biofluids such as saliva. Hence, the decision was made

to use IrOx electrodes as the potentiometric electrodes. IrOx electrodes on planar surfaces have been reported in the literature[30], and the future plan is to embed these electrodes on-chip.

The amperometric electrodes usually involve a gold or platinum surface, and hence are much more straightforward to implement. For the tests, commercial Dropsense 550 planar electrodes are utilised.

2.3.2 Potentiometric Front End Circuits

The potentiometric front end circuit measures the input voltage obtained from the IrOx electrodes, likely in the range of $V_{ref} \pm 0.4V$ [31] with a high output linearity at low power.

2.3.2.1 Potentiometric Front End Configuration

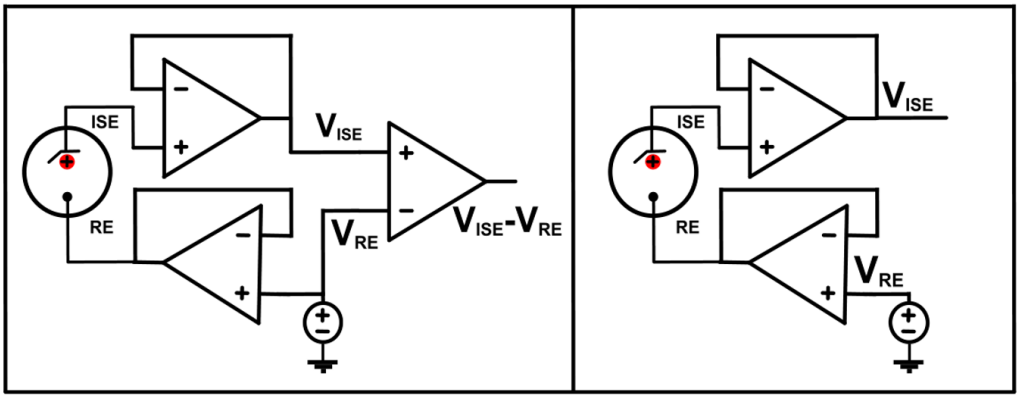


Figure 2.6: Left: Conventional potentiometric front end configuration with two voltage followers and a differential amplifier to subtract the difference. Right: Potentiometric front end with two voltage followers with only the V_{ISE} measured

There are two configurations that could be utilised for potentiometry. Taking the example of the measurement of pH utilising an ISE and a RE, a basic system will consist of a 2 voltage followers, one supplying the RE and one reading the ISE as shown in the left image of Fig. 2.6. The difference between the voltages at each electrode (ISE-RE) could then be amplified with a differential amplifier in a normal case scenario to give an indication of the pH value.

It is also possible to utilise a single output from the ISE as a measurement of the pH as shown in the right image of Fig. 2.6. The output voltage of the ISE provides a linear relation to the pH value. However, it is key that RE is held constant throughout by a reliable supply, and that the range of measurements of the V_{ISE} does not go beyond the supply rails of the voltage follower. In this scenario, one less op-amp is required.

2.3.2.2 Potentiometric Read Out Circuits

There are numerous methods discussed in literature for converting the voltage signal into either a magnitude, phase or frequency variation. These can be grouped into: (1) Analog to Digital Convert-

ers (ADCs)[32][33][34] or (2) Voltage Controlled Oscillators (VCOs)[35][36][37] with some unique methodologies outside these 2 main groupings. Generally speaking, VCOs have the advantage of simplicity and low-power while ADCs have the advantage of a faster conversion time.

As power consumption will be a major priority in this project in comparison to speed of processing, most of the examples here will look at VCOs.

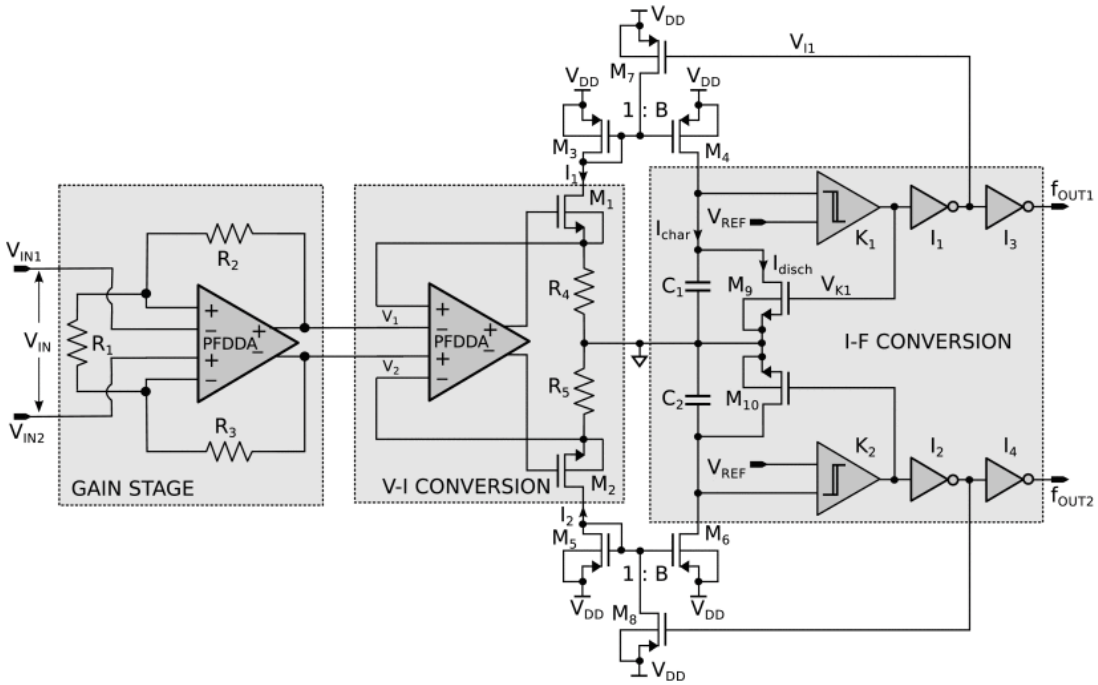


Figure 2.7: Schematic of the voltage-to-frequency converter for a 0-10mV input described in [35]. This is notable in particular for their low input voltage range of 0-10mV.

Arbet et al. describe a differential voltage to frequency converter for ultra low input voltages (0-10mV)[35]. Their system consists of 3 key stages - a gain stage, voltage to current conversion and a current to frequency conversion stage. The gain stage is a pseudo fully differential differential amplifier through which the gain can be varied with feedback network resistors R_1 to R_3. The current to frequency converter simply converts a proportional input voltage to an output current based on the value of R_4 or R_5. The final stage begins with an integrated output before conversion into pulsed signals. A feedback loop from the output of the inverter to transistor M_7 helps set the charge and discharge states. They achieve a circuit with a sensitivity of 348.8Hz/mV at a 78mW power supply.

A combined pH-impedance sensing system for ISFETs with a frequency output is implemented by Aslanzadeh et al.[36]. Their system consists of an input ISFET sensor with a current to frequency converter. They utilise a differential amplifier to convert the output voltage from the circuit into a current. This current charges a capacitor from which two comparators utilise as a comparison window for converting this voltage level to a frequency. An set-reset(SR) latch is used at the output of the comparator to supply the charging and discharging of the previously mentioned capacitor. Their circuit power consumption is at 40.2μW.

Azcona et al. present a voltage to frequency converter for use in wireless sensor networks[37]. It is

capable of operation in both single and differential mode, whereby an offset frequency of 0.1MHz is subtracted from the output frequency.

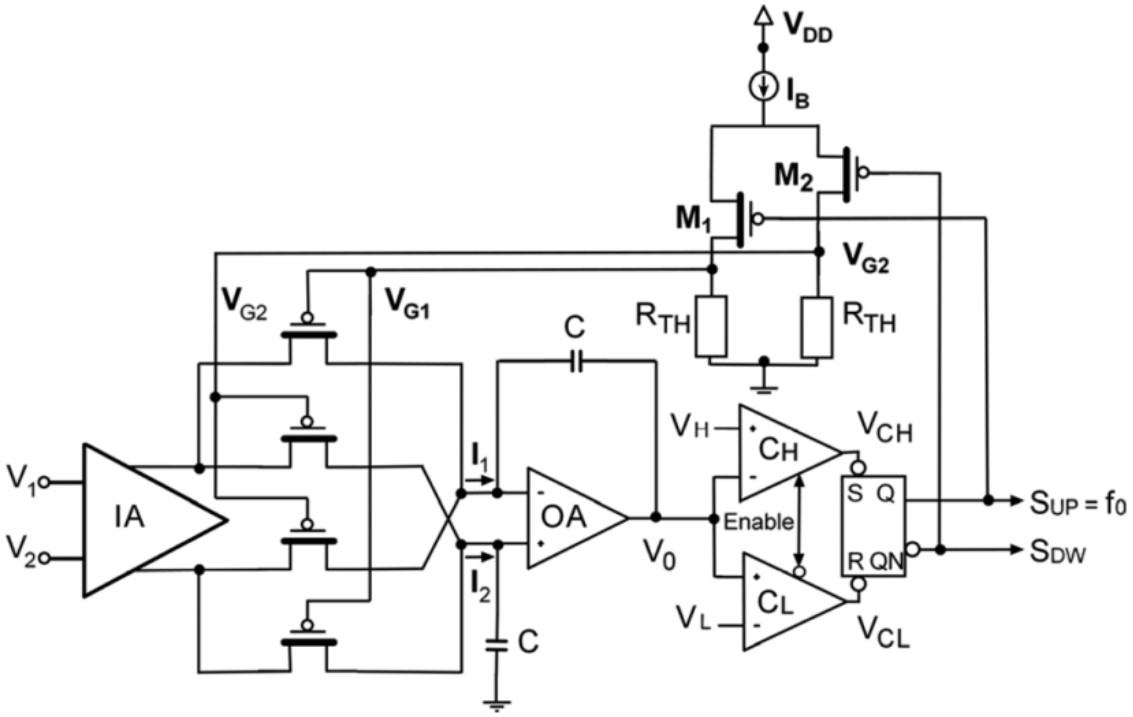


Figure 2.8: Schematic of the potentiometric front end circuit described by Valero et al. [38]. They utilise a differential input with a voltage to current converter that is driven into two comparators to obtain an output frequency.

A voltage-to-frequency converter with temperature drift compensation is presented by Valero et al.[38]. Similarly to [35], they utilise a differential input with a voltage to current converter, as well as a integrator driven current to frequency converter. A key point in their work is to introduce temperature compensation by implementing R_{TH} in order for the output to be temperature independent.

A 60μW voltage-to-frequency converter is described in [39]. The top level schematic is shown in Fig. 2.9. The circuit utilises a voltage to current converter with using a common-source amplifier with rail-to-rail operation. The transistors are operated in the sub-threshold region for low power. The current is mirrored across to a gm-boosted differential pair comparator ideal for low voltages.

Table 2.1: Comparison of potentiometric read-out topologies

Ref	Tech(nm)	Supply Voltage (V)	Output Range(Hz)	Input range(V)	Sensitivity	Power Consumption(μW)
[35]	130	0.4	0.033-3.48M	0-10m	348.8Hz/mV	7800
[36]	180	1	4.9-6.7M	370-630m	6.92MHz/V	40.2
[37]	180	1.2	100-1000k	0-1.2	750kHz/V	80
[38]	180	1.8	0-1400k	0-1.2	861kHz/V	375
[39]	180	1.2	0-0.5M,0.5M-1M	0-1	NA	60

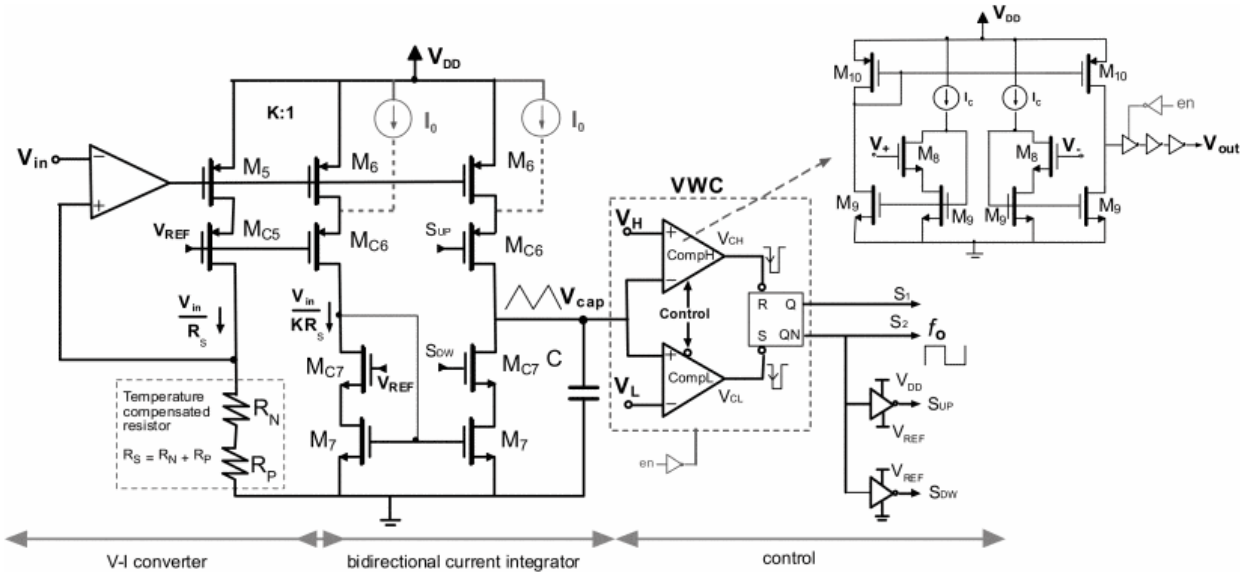


Figure 2.9: Schematic of the potentiometric front end circuit described by Azcona et al. [39].

2.3.2.3 Comparison of Potentiometric Topologies

Table 2.1 shows selected topologies that have an ideal metrics such as power consumption or input range, with their key metrics compared. A common feature amongst these VCOs were a voltage-to-current conversion, which suggest that this stage is key in order to lower the power consumption. However, the output frequency range is still fairly high(>100Hz), which means that the power consumption could be reduced much further for lower frequency ranges.

2.3.3 Amperometric Front End Circuits

There are a number of reviews on current sensing front end available [40][41][42][43] which are helpful to gain an insight into amperometric circuit design. The amperometric front end consists of circuitry to read a generated dc current from the postulated electrodes on chip. The range of current expected from such miniscule sensors will likely be 50nA to 0.3μA for enzymatic reactions[44]. However, this will vary based on the applied reference voltage, as well as the surface area of the WE and counter electrodes. Hence, a large dynamic range of measurement will be ideal, with a high resolution with the bandwidth of interest while keeping power consumption low.

Instrumentation for an amperometric biosensor usually involves 4 blocks: a signal generator, potentiostat, readout circuit and signal processing[42]. The signal generator could potentially output different stimulus signals at the RE(triangle, saw or pulse) - but will simply be a constant signal in the case of a dc current. The potentiostat serves to maintain the potential between the RE and the WE throughout the operation such that any variation in the current measured is due to the analyte. The read out circuit measures the current obtained, while the signal processing block filters any potential noise in

the measurements. Thus, this overview focuses on the two more complex circuitry - the potentiostat as well as the read out circuit.

2.3.3.1 Potentiostat

The potentiostat fixes the cell voltage between the reference and WE to the reduction potential of the analyte. This is imperative to ensure that the reaction occurs at the optimal voltage intrinsic to each reaction [45]. In terms of circuitry, there are four possible configurations: (1) Grounded-WE (2)Grounded-RE, (3)Grounded-CE and (4)Differential.

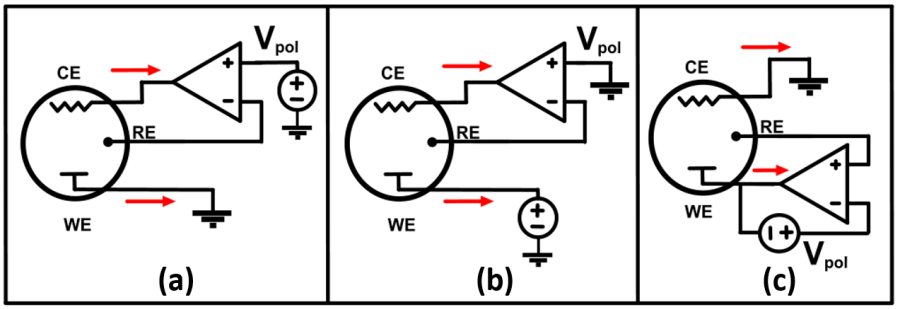


Figure 2.10: Three types of potentiostat configurations with (a) Grounded-WE, (b) Grounded-RE and (c) Grounded-CE. The red arrows indicate the current measurement points. Adapted from [46].

The grounded-WE configuration represents the most widely utilised configuration in literature [47] [48] [49] [50]. This configuration consists of a single op-amp as the potentiostat which provides a polarisation potential to CE, with RE connected to the negative terminal. The RE voltage is forced to the polarisation potential by the feedback in the opamp, which results in a potential difference across RE and WE. This induces a current from CE that flows to the grounded WE electrode, from which it could be measured. The grounded-RE configuration is fairly similar, whereby in this case the rather than RE being held at the polarisation potential, it is held at ground. Thus a current is induced in the opposite direction.

The grounded-CE configuration is relatively uncommon in comparison to the previous 2 configurations and is usually used for specific applications. Busoni et al. describes a scenario where connecting a current measuring device in series with the WE is inconvenient[46]. In their work, the WE is a mercury electrode connected to a mercury reservoir through tubing. This assembly cannot be shielded satisfactorily from external eletromagnetic interference - hence any measurement source there will affect the readings. In addition, the current measuring device will add an impedance in series with the WE, which although low at DC and at low frequencies, will increase rapidly with increased frequency. Thus, their application will be more suited to a measurement from a grounded-CE configuration.

These previous single-ended architecture configurations have the limitations in terms of not being able to dynamically control the voltages on the CE and WE. Martin et al. describe a fully differential potentiostat that overcomes this limitation[51]. As shown in Fig. 2.11, the output potentials at the RE and WE electrode are buffered and summed with with a fully differential amplifier. In addition, the fully differential amplifier is also configured in negative feedback which forces its inputs to a zero

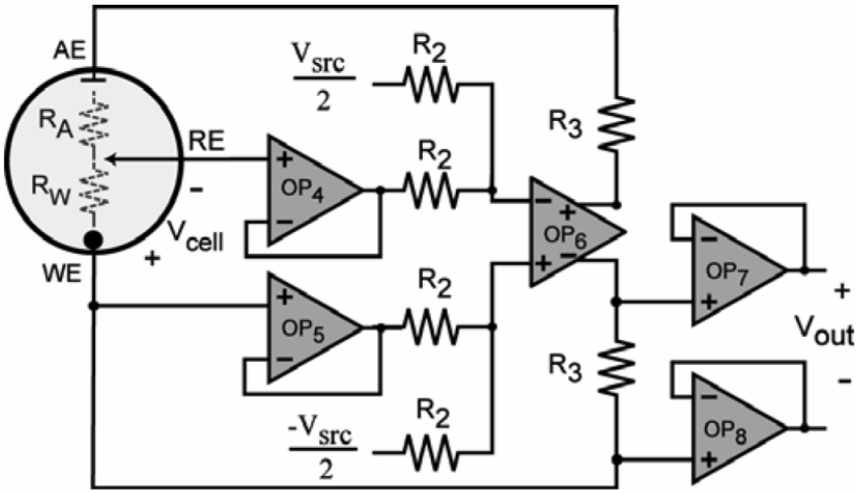


Figure 2.11: Example of a fully differential potentiostat described in [51].

voltage. This topology allows the voltage between WE and RE to go up to twice the reference voltage. A similar topology is also reported in [52] for neurotransmitter detection.

2.3.3.2 Amperometric Read Out Circuits

An amperometric read out circuit should have the ability to read a large dynamic range of current for at a low power consumption. There are three main types of read out circuits:(1) Current conveyors, (2)Transimpedance Amplifiers, and (3)Digitised Outputs.

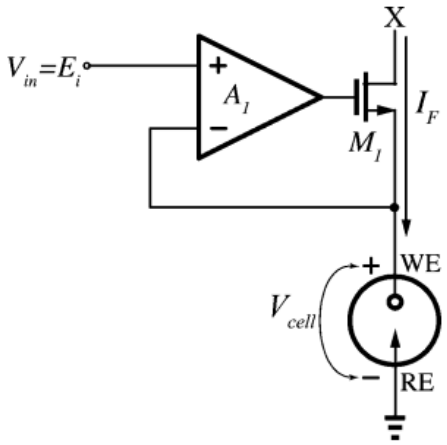


Figure 2.12: Example current conveyor circuit described by Ahmadi et al. [53]

Current conveyors involve read out circuits whereby the measurements are completely handled in the current domain without any translation to voltage. Fig. 2.12 shows an example current conveyor circuit from [53]. The current I_F is directly conveyed from the WE to the high impedance node X,

without any conversion to voltage. This topology allows for a low power consumption due to the reduced number of components, but is very dependent on the current mirror. Thus, these circuits are particularly susceptible to process variations which cause mismatches in the current mirror. This topology is reported in [53] [54][55][56][57].

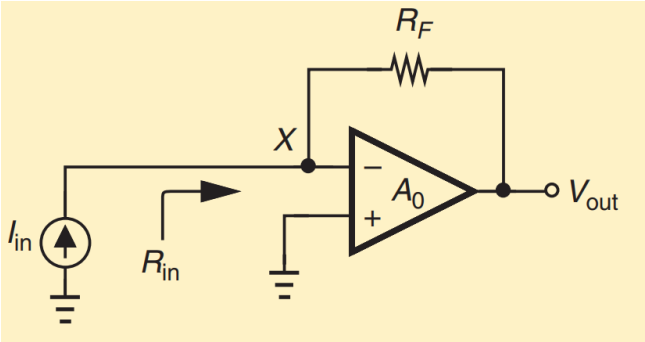


Figure 2.13: Basic transimpedance amplifier circuit from Razavi et al. [58]

The second group of topology involves transimpedance amplifiers. The simplest amperometric read out circuit will consist of a current to voltage converter such as a transimpedance amplifer, whereby the output voltage is converted into a value of the input current based on the resistance value in feedback. The measured current range can be varied through the feedback resistor. For extremely small currents however, this topology has the limitation that the feedback resistor can become very large - which is an issue for CMOS based designs[42]. In addition, the thermal noise of the feedback resistor becomes more of an issue at higher values. The basic circuit can be seen in Fig.2.13 as described in [58].

This resistor could also be swapped with a switched capacitor as well to become a capacitive feedback circuit. This provides an improvement upon the previous topology by reducing the noise and is usually the preferred method for CMOS architectures. In this system, the capacitor is charged to saturation before the charge is reset through a switch. A differentiating amplifier is then used to recover the linear relationship between the input current and output voltage. This results in this system having high sensitivity and low noise across a large bandwidth[43].

Digitising the output allows for a simpler analysis of the measured signal. ADCs specifically developed for current-mode applications have been utilised in [59][60][61]. These circuitry generally have the best sensitivity at a low power consumption. Current to frequency converters are front end circuits that directly convert to input measured current into a proportional frequency. This is usually utilised in applications where resources such as power and area is extremely constrained. Another key advantage in such a topology is that the output can be used with load shift keying techniques. Thus, the decision was made to focus the literature review on current to frequency converters.

2.3.3.3 Current to Frequency Converters

An integrator-differentiator current measurement system with a current to frequency output is demonstrated in [63]. As mentioned previously, the integrator-differentiator setup allows for excellent noise

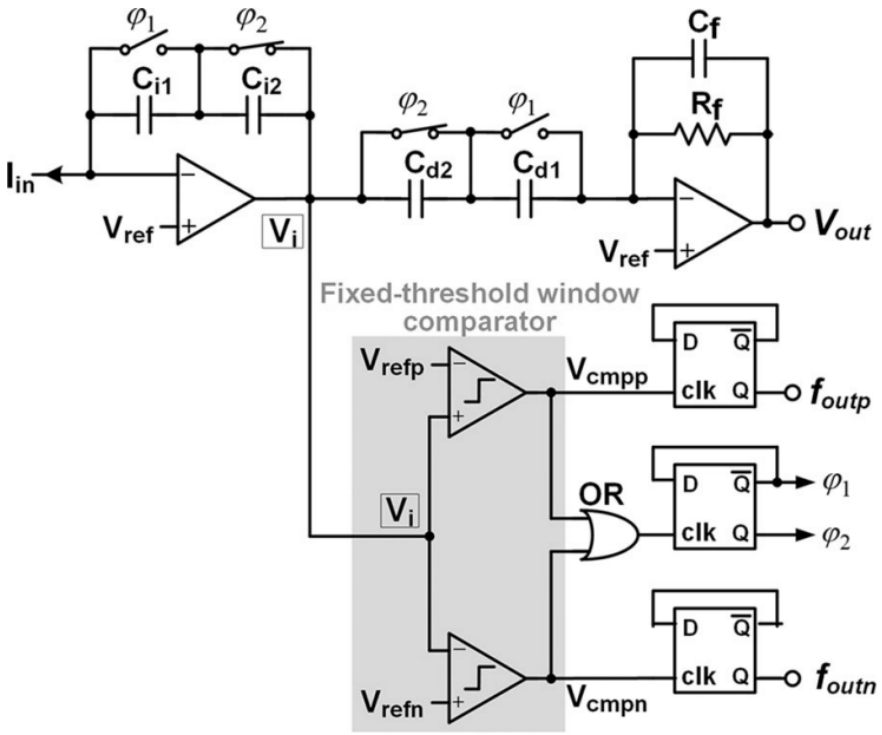


Figure 2.14: Schematic of the current to frequency converter circuit described in [62]. This circuit uses an integrator-differentiator setup with a frequency output to obtain a reading for the current. Note the 3 outputs available in the system.

performance across a wide bandwidth. As shown in Fig. 2.14, a self-timed switched capacitor network is added to reduce the reset transients and prevent saturation at the integrator. The output sets both switches and reduces the need for any external reset or clock signal. This allows for the reset transients and recovery time to be minimised and the maximum measurable current increases.

A CMOS glucose sensor for wireless contact lenses is developed in [54]. In this work, the transimpedance amplifier is avoided due to the inductive input impedance that may result in an unstable control loop in an in-eye electrochemical cell. Hence, they utilise the current mirror topology previously discussed in [53]. The mirrored current is fed into a current-to-frequency ring oscillator seen in Fig. 2.15. The oscillator used is a current-starved ring oscillator that operates at 9.9Hz/nA. The output frequency is then backscattered through near field communications for wireless transmission.

A sigma-delta ADC is used to measure a 160dB dynamic range input current in [61]. The ADC designed in capable of a full scale input currents with reduced linearity. It contains a capacitive-feedback TIA with a switch driven by two continuous-time comparators. The output of the comparators are fed into a pulse counter. Through sampling of the counter, a digital representation of the frequency is obtained.

Yan et al. describe a switched-capacitor potentiostat with feedback in [64]. The output of the a differential switched-capacitor is fed back to the drive the reset switches. However, rather than their output being a frequency, they utilise a frequency to digital converter with the digital signal converter to a low sampling frequency - thus reducing the data rate of the system.

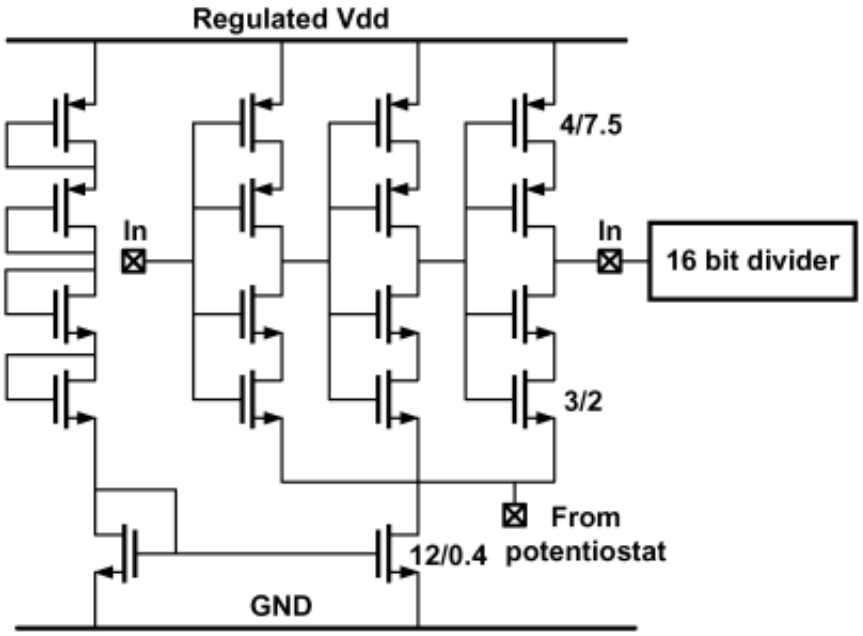


Figure 2.15: Current starved ring oscillator utilised in [54].

2.3.3.4 Comparison of Current to Frequency converters

Table 2.2 shows the comparison of the different current-to-frequency converters. The design in [61] shows an extremely high dynamic range for a relatively low power consumption and shows promise in its implementation in comparison to the other implemention. A common trait for all these systems is a frequency output that is fed back into the input stages for charge resetting. The systems in [64] and [61] have an output frequency to digital converter which allows for a digital representation of the signal. Both these systems use counters to implement this.

Table 2.2: Comparison of Current-to-frequency converters in the literature

Ref	Tech(nm)	Area(mm^2)	Max Current(μA)	Dynamic Range	Signal Bandwidth(Hz)	Power(μW)	Supply Voltage
[63]	180	0.091	11.6	155.1dB	1.4M	5220	1.8
[54]	130	0.36	0.15	NA	1.8G	3	1.2
[61]	180	0.2	10	160dB	1.8	295	1.8
[64]	180	0.02	2.5	52dB	10	4200	1.8

2.4 Wireless Powering on CMOS

Wireless power transfer can be classified into two main classes: (1) Far field, which involves long range power transfer through the application of infrared, ultraviolet or microwaves, and (2) Near field, which is for shorter ranges and usually involves utilising electric or magnetic fields. Near field power transfer is

Inductive coupling is a method of utilising electromagnetic induction for wireless power transfer. A

transmitter coil generates an alternating magnetic field through an alternating current flow. When this alternative magnetic field passes through a receiver coil for the sensor, a voltage is induced as per Lenz's Law.

$$\varepsilon = -\frac{d\phi_B}{dt} \tag{2.2}$$

Where ε is the induced voltage, and ϕ_B is the magnetic flux through the transmitter coil. This method allows for the miniaturisation of wireless electrochemical sensors. Previous work in this field demonstrate a number of examples of wirelessly powered electrochemical sensors and has been shown to transmit power wirelessly in the range of 10 – 90mW [65][66][67][68].

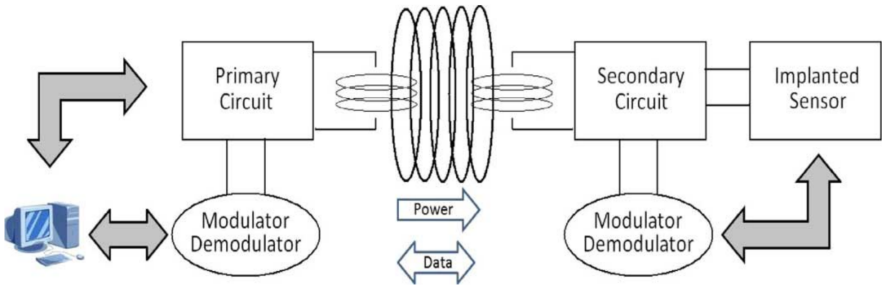


Figure 2.16: Inductive Coupling with Power and Data Transmission. Taken from [69]

There exists an optimum frequency depending on the medium transmitted, as well as the distance of transmission. The wave frequency relation with energy is given by **Equation 2.3**:

$$f = \frac{c}{\lambda} = \frac{E}{h} \tag{2.3}$$

Where c is the speed of light, λ is the wavelength, E is the photon energy and h is Planck's constant. This give rise to the following relation, where the frequency of transmission is inversely proportional to the wavelength. Hence, increasing the frequency allows for smaller antennas. This is due to the fact that for optimum transmission, the antenna length should be at least a quarter of the wavelength transmitted.

The depth of penetration is given by the following formula [70]:

$$Depth\ of\ Penetration = \frac{1}{2\pi f}\left[\frac{\mu\epsilon}{2}(\sqrt{1+(\frac{\sigma}{\epsilon 2\pi f})^2}-1)\right]^{-\frac{1}{2}} \tag{2.4}$$

Where f is the frequency of the radiation, μ is the permeability of the material, ϵ is the permittivity of the material, and σ is the conductivity of the material. Hence, as the penetration depth is inversely proportional to the frequency of transmission ($Depth\ of\ Penetration \propto \frac{1}{f}$), it can be stated that low frequencies increase the penetration depth through a material.

As a result, there is a trade-off between using a high frequency to minimise antenna size, and a low frequency for increasing penetration depth. This together ensure that the frequency chosen would

be an optimisation problem. Additionally, there are a multitude of works that provide solutions to this issue [71][72] to determine the optimum frequency for transmission. Their work mainly involves utilising algorithmic solutions based on the energy efficiency equation to determine the optimum frequency, as well as the optimum coil trace widths and thickness.

2.4.0.1 Wireless Power/Data Management System Overview

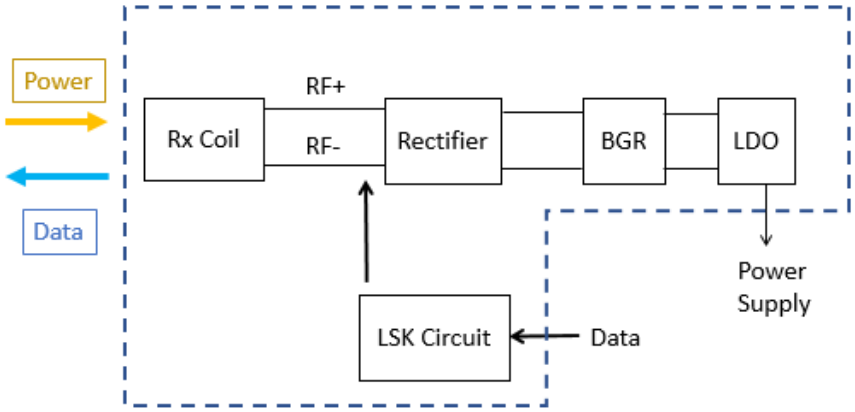


Figure 2.17: Power and Data Management Block Components

The overall circuits required for a power and data management block is shown in Figure 2.17 above. There are 5 blocks of note, and will be discussed in the following order.

1. Inductive Receiver(Rx) Coil
2. Rectifier
3. Bandgap Reference(BGR)
4. Low-Dropout Regulator(LDO)
5. Load-Shift Keying(LSK)

A brief discussion into the various receiver coils will be compared based on their application, technology and capabilities. Next, the various blocks for the rectifier, bandgap reference, low-dropout regulator and load-shift keying circuit will be explained, along with a rationale for the chosen topology. The chart can be seen in Fig. 2.18 below.

2.4.1 Inductive Receiver Coil

The inductive receiver coil is paired with a transmitting coil for power and data transmission. Work done in [73] compares three different implementation of coils - Around-CMOS, where a coil is wire-

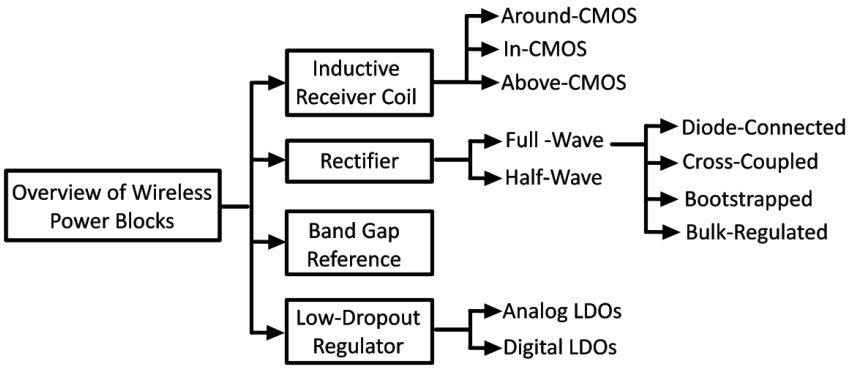


Figure 2.18: Mindmap of various wireless power block toplogies

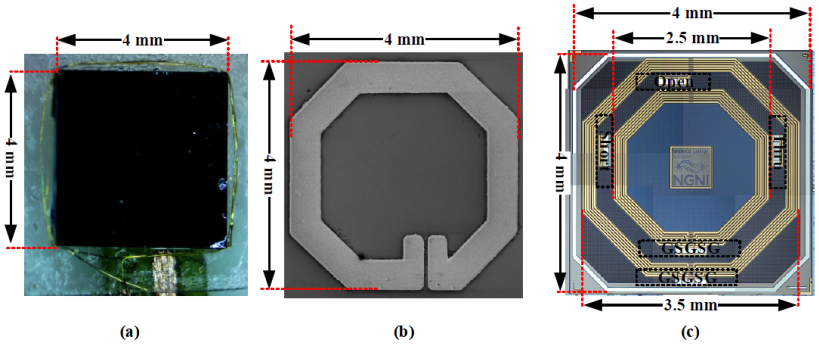


Figure 2.19: Illustration of various coils (a) around CMOS, (b) above CMOS and (c) in CMOS. Taken from [73]

bonded to a chip, Above-CMOS, where a coil is flip-chip bonded to the chip, and in-CMOS, where the coil is fabricated completed in the silicon die.

A number of different implementations of wirelessly powered coil on chip implementations are compared in this section. This is specifically for in-CMOS implementation, where the coil is fabricated on the silicon die itself. The power transfer efficiency of each of the implementations are recorded in Table 2.3.

The results in Table 2.3 shows that in-CMOS chips provides the lowest transfer efficiency among all three methods. As the thickness of the metal layer is defined by the CMOS technology employed, this limits the Q factor of the coil, thus affecting its efficiency[74]. However, in terms of the design considerations, power efficiency is not key. Rather, the lack of post-processing required for an in-CMOS

Table 2.3: Comparison of different types of coil implementations, and their various efficiencies

Type	***Around-CMOS***		***Above-CMOS***		***in-CMOS***	
Medium	*Air*	*Tissue*	*Air*	*Tissue*	*Air*	*Tissue*
Distance(mm)	12	12	12	12	12	12
Frequency(MHz)	600	300	110	60	426	330
PTE(%)	26.3	3.88	19	2.12	8.18	1.68

coil makes it highly desirable for mass production techniques.

2.4.1.1 Prior Work on Wirelessly Powered Coil on Chips

In [75], an energy harvesting chip for continuous power or duty-cycled power delivery is proposed. Figure 2.20 illustrates the system. The entire chip is 1.6 $\times$ 1.6mm, and contains a coil, voltage rectifier, a low-dropout voltage regulator, a storage capacitor and a power management unit that monitors the rectified voltage, and determines the power delivery mode. By observing the voltage on the storage capacitor, the power management unit activates or deactivates the voltage regulator depending on the power input.

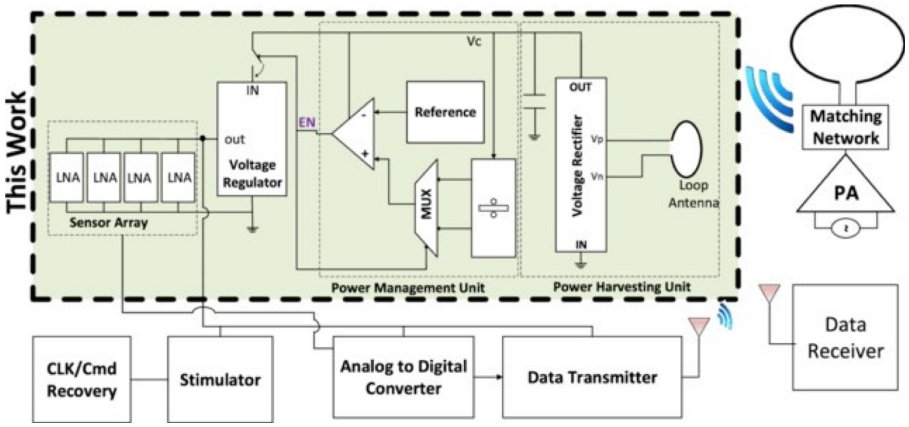


Figure 2.20: Wireless energy harvesting chip developed by Rahmani et al. Taken from [75].

In [76], a wireless chip is optimised for a 10mm distance. Figure 2.21 illustrates the system. Similarly, the chip is designed for energy harvesting, and not for any direct electrochemical sensing.

In this chip, a 2 $times$ 2.18mm receiver coil is implemented, which operates at a frequency of 187MHz. An adaptive matching circuit is also employed to vary the optimum frequency by capacitance adjustment. This adjustment is controlled by a digital adaptation circuit. In addition, a voltage rectifier is also employed, along with a voltage doubler used to supply a second supply voltage higher than the main supply to drive the gate of the regulator employed. Lastly, a bandgap reference circuit is used to supply the reference voltage for the system.

In [77], a 4 $times$ 4mm coil is designed for a 433Mhz frequency. Figure 2.22 illustrates the system. Adaptive matching is also employed for tuning along a range of frequencies from 400-460Mhz. In this case, telemetry is employed through the use of load-shift keying. A cross-coupled rectifier is used to obtain a DC voltage, with a regulator integrated into the rectifier to smoothen the voltage ripple. Specifically, a sigma delta ADC is integrated into the chip to monitor readings, along with a Bandgap reference to provide a 1.2V reference for the circuit.

In [55], a 6μW glucose monitoring system is designed on a CMOS platform.Figure 2.23 illustrates the system. This design uses an inductive coupling link at 900Mhz, and is fabricated in a 1.4 $times$ 1.4 $times$ 0.25mm^3 prototype.

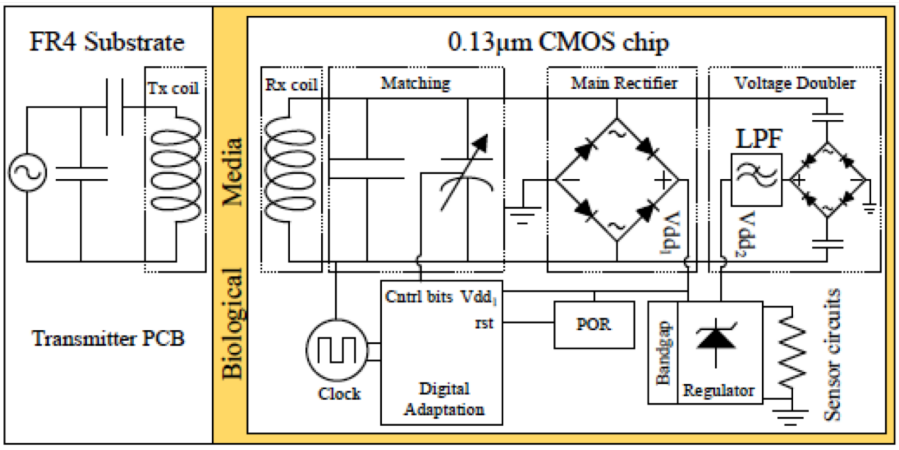


Figure 2.21: Wireless circuit with digital adaptation designed by Zargham et al. Taken from [76].

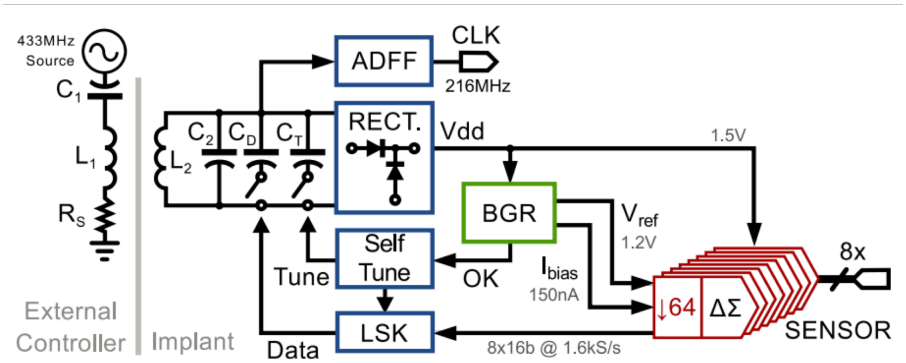


Figure 2.22: 433MHz wireless chip that employs adaptive matching with a frequency range. Taken from [77].

A 4-turn 1.3 $times$ 13mm on-chip coil is implemented on the top metal, with a 400fF on-chip MIM capacitor used for resonance at 900MHz. A 3-stage full-wave rectifer is employed along with a 400pF MOS capacitor to filter the resultant ripple. In addition, a reference voltage and a linear voltage regulator generates a 1.2V supply voltage. After readout is complete, the ADC output is serialised and transmitted to the reader by modulating the MOS switch at a rate of 200kbps.

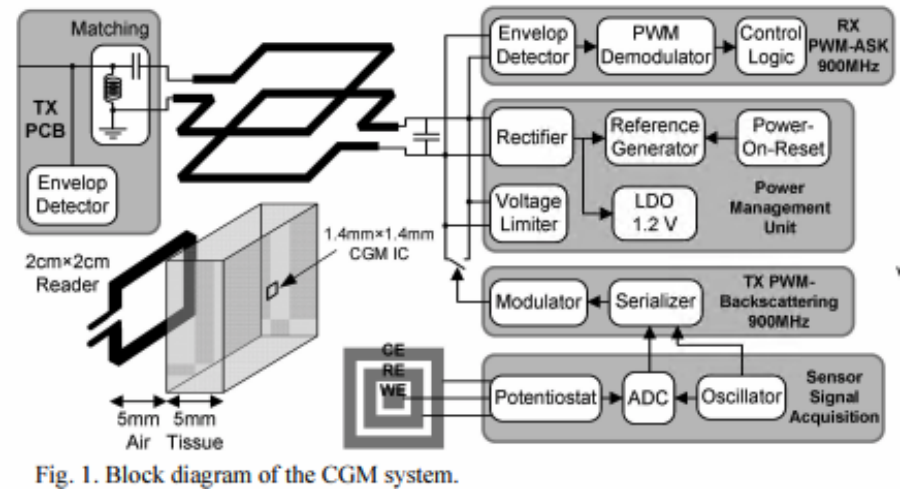


Figure 2.23: Coil-On-Chip System designed by Nazari et al. Taken from [55].

In [54], a read-out circuit is designed for monitoring glucose in contact lens. Figure 2.24 illustrates the system. Although the coil and sensors are external, it is significant as the CMOS chip implementation measures 0.6 $times$ 0.6mm, and contains a regulator, readout circuitry, rectifier and potentiostat.

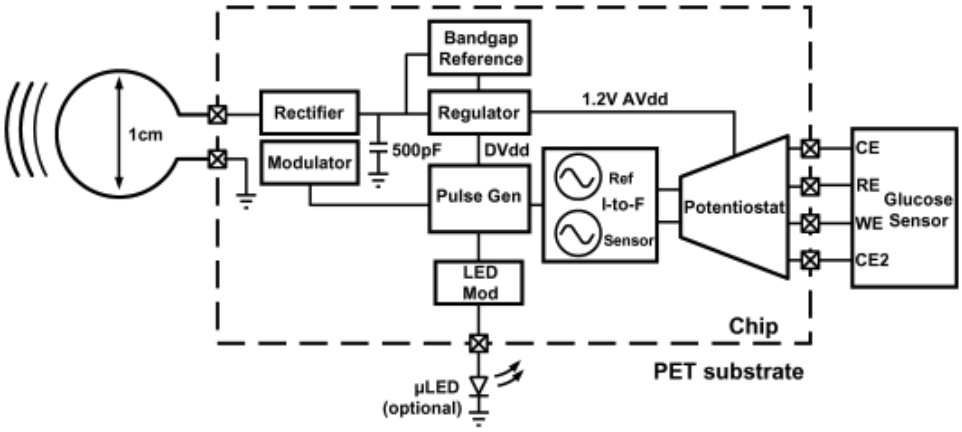


Figure 2.24: Glucose contact lenses system developed by Liao et al. Taken from [54].

In [78], a two-turn on-chip coil is used for 915Mhz carrier frequency. The coil size is 1.2 $times$ 1.2mm, and employs a 3 stage full wave rectifier to a 1.2V supply. The LDO generates a 1V supply.

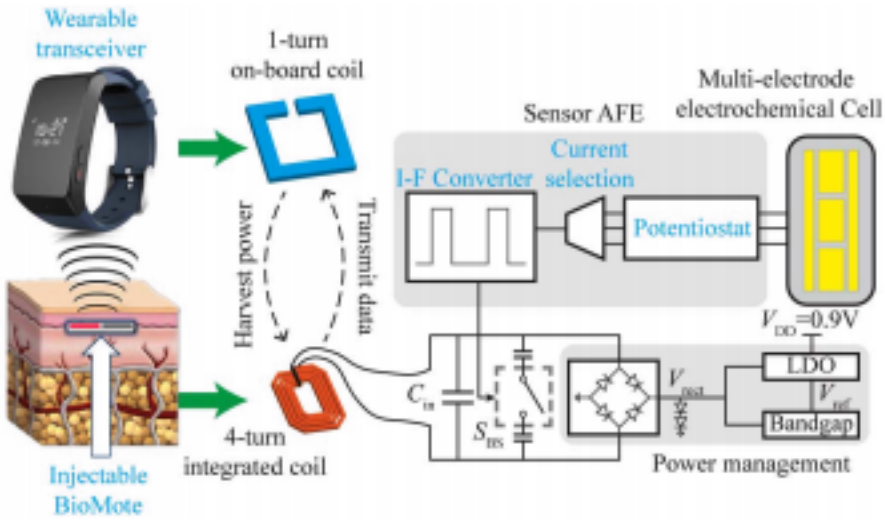


Figure 2.25: Alcohol Biomote developed by Jiang et al. Taken from [12].

In [12], a 4-turn 0.85 $times$ 1.85mm coil is implemented on the top metal layer for a carrier frequency of 985MHz. Figure 2.25 illustrates the system. A 5-stage full-wave rectifier is used here, along with a diode clamp for overvoltage protection. Similarly, a bandgap reference and LDO generates a 900mV supply voltage along with a 5nA reference current. The dyanmic range of the potentiostat employed here only covers the necessary physiological range of alcohol and pH. The potentiostat output is then fed into a I-to-F converter and transmitted via backscatter through modulation of the resonant frequency of the wireless link.

Their work is significant due to the low power potentiostat employed, which only consumes 500nW, a reduced measurements time of only 3 seconds, and through the transmission of data using backscat-

tering. This removes need for ADCs and clock generators, thus being able to achieve a low 0.97μW power budget.

A comparison of the different types of on-chip coil implementations are shown in Table 2.4. [78][55][12] utilise a higher range of frequency based on the work of [79], and also report similar capabilities of transmission through tissue. With higher frequencies employed, they are also able to minimise the size of the coil. This reveals a trend for wireless-powered devices to move towards higher frequencies to enable smaller medical devices to be developed. In addition, optimising and reducing power consumption is particularly critical in order to allow for sensors to function reliably and accurately.

2.4.2 Rectifier Architectures

The rectifier serves to convert the AC voltage obtained from the inductive coil to a DC voltage for use by the remaining circuits. These rectifier circuits can be realised through the use of half-wave or full-wave rectifiers as shown in Fig. 2.26. The advantages of a half-wave rectifier are a simpler implementation with less components, thus resulting in a lower power consumption and area. However, this comes at the cost of lower power efficiency.

$$\eta = \frac{P_{DC}}{P_{AC}} = \frac{(\frac{I_{max}}{\pi})^2 \times R_L}{(\frac{I_{max}}{2})^2 (r_f + R_L)} = \frac{\frac{4}{\pi^2}}{1 + \frac{r_f}{R_L}} \tag{2.5}$$

Where η is the efficiency, P_{DC} and P_{AC} are the DC output power after rectification and AC input power before rectification respectively. I_{max} is the max current, r_f the diode resistance and R_L the load itself. For $r_f \ll R_L$, 9.4% of power is lost from the circuit implementation.

The efficiency for a half wave rectifier is given by Equation 2.6 below.

$$\eta_{half} \approx \frac{4}{\pi^2} \approx 40.6\% \tag{2.6}$$

In contrast, the efficiency for a full wave rectifier is given by Equation 2.7.

$$\eta_{full} \approx \frac{\frac{8}{\pi^2}}{1 + \frac{r_f}{R_L}} \approx 81.2\% \tag{2.7}$$

Fig. 2.26 describes both types of rectification methods.

A brief overview of various rectifier topologies will be reviewed and compared in this section. Rectifier design is a fairly popular topic due to its importance in wireless power harvesting techniques, with reviews and design guides available [80][81][82].

Diode-connected transistors are usually used in CMOS for the implementation of rectifier circuits. This allows for a simpler implementation as compared to standard diodes in terms of area and power consumption. However, this comes at the cost of having the threshold voltage (V_{th}) and a voltage drop across the channel resistance having a huge effect on the power efficiency [83]. This can be

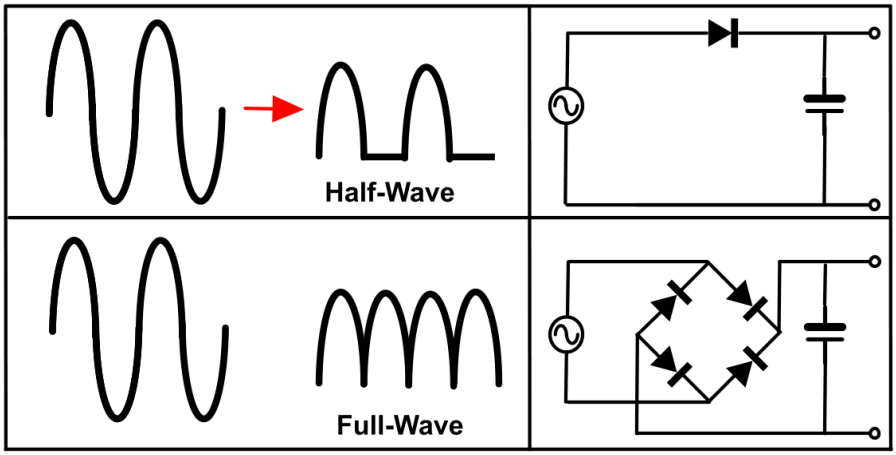


Figure 2.26: Demonstration of half-wave and full-wave rectification

Table 2.4: Comparison of On-Chip Coil Wireless Power Implementations

Reference	Process(μm)	Area of Coil(mm)	Intervening Medium	Transmission Frequency	Rectifier	Matching Circuit	Data Telemetry	Supply(V)	Power Consumption(μW)
[75]	0.18	1.6x1.6	10mm Air	2.75GHz	6 Stage Rectifier	No	No	1.1	1210
[76]	0.13	2x2.18	10mm Air/Muscle	160MHz	Cross Coupled Hybrid	Yes	No	3.1	NA
[77]	0.35	4x4	3mm Tissue	433MHz	Cross Coupled	Yes	LSK	1.5	92
[55]	0.18	1.4x1.4	5mm Tissue/Air	900MHz	3-stage	Yes	LSK	1.2	6
[78]	0.065	1.2x1.2	10mm	915MHz	3-stage	No	PWM-ASK with backscattering	1	4
[54]	0.13	10(dia)	15cm Tissue	1.8GHz	NA	No	FM-LSK	1.2	3
[12]	0.065	0.85x1.5	2.4mm Tissue	985MHz	5-stage	No	Backscattering	0.9	0.97

circumvented with Schottky diodes that lower the voltage drop, but are usually not implemented in standard CMOS processes due to the extra fabrication required [84]. In particular at sub-micron CMOS technologies where the ratio of power supply to V_{th} decreases, simple diode-connected structures become less and less efficient.

There have been two overarching techniques proposed in the literature to improve the efficiency of rectifiers. First, the use of novel circuits that improve upon the present configuration, and second, by cancelling V_{th} to improve efficiency. The first method involves reconfiguring the circuitry either using cross-coupling or adding active circuits, while the second method involves additional biasing circuitry that reduces the V_{th}.

Fig. 2.27 describes the basic bridge wave rectifier topology and shows how the topologies evolve. The basic full wave bridge rectifier has a high power efficiency compared to the half wave rectifier as spoken about previously. To improve the efficiency of this circuit further, the gate of the diode-connected transistor is connected to the voltage drop across a mosfet transistor[85][86]. This allows for the voltage at the gate to be driven at a higher voltage at each cycle compared to the basic configuration. This has the advantage of a lower leakage and higher conductivity, resulting in improved efficiency. It is possible for the circuit to either be half cross-coupled, or fully cross-coupled. The half cross-coupled topology still has a voltage drop across the load transistors, while the fully cross-coupled topology should ideally circumvent that. In practice, it was found that the fully cross-coupled topology did not have a good power efficiency[87]. This was the result of current leakage through to the antenna from the cross-coupling connections in addition to parasitics.

Active rectifiers rely on transistors that switch the transistors required for rectification. An example implementation can be seen in Fig. 2.27. This topology is seen in [88] and utilises two active diodes D1 and D2 to be switched on and off quickly to avoid reverse leakage current. In this design, comparators are used to improve the switching time of the transistors to 10ns. This topology has been used in [89][90][91] with higher efficiencies reported. However, it is important to note that the additional active circuitry constitutes a higher power consumption especially at higher frequencies, where more power is required to switch the large transistors.

V_{th} is dependent on the oxide thickness of the chosen process. Some processes offer a low V_{th} option, usually at the cost of higher leakage currents resulting from higher doping along the channel. Thus, such options are generally not used in the implementation of rectifiers where the power efficiency is key. There exist 2 main types of techniques reported in the literature: (1)bootstrapping and (2) bulk regulated biasing.

Bootstrapping involves the reduction of the threshold voltage through the use of capacitors to store the charge as shown in Fig. 2.28. As described in [92], when the input voltage is higher than the output voltage by at least V_{th}, current flows through D1 and charges the output capacitor to $V_{IN} - V_{th(nmos)}$. As the output voltage increases, the voltage at V_{cap} increases to $V_{IN} - 2V_{th(nmos)}$. The PMOS begins conducting to charge the output node until the gate source voltage reaches $V_{th(pmos)}$. The overall circuit results in the effective V_{th} reducing to $V_{th(pmos)} - V_{th(nmos)}$. This technique is also reported in [93][94][95].

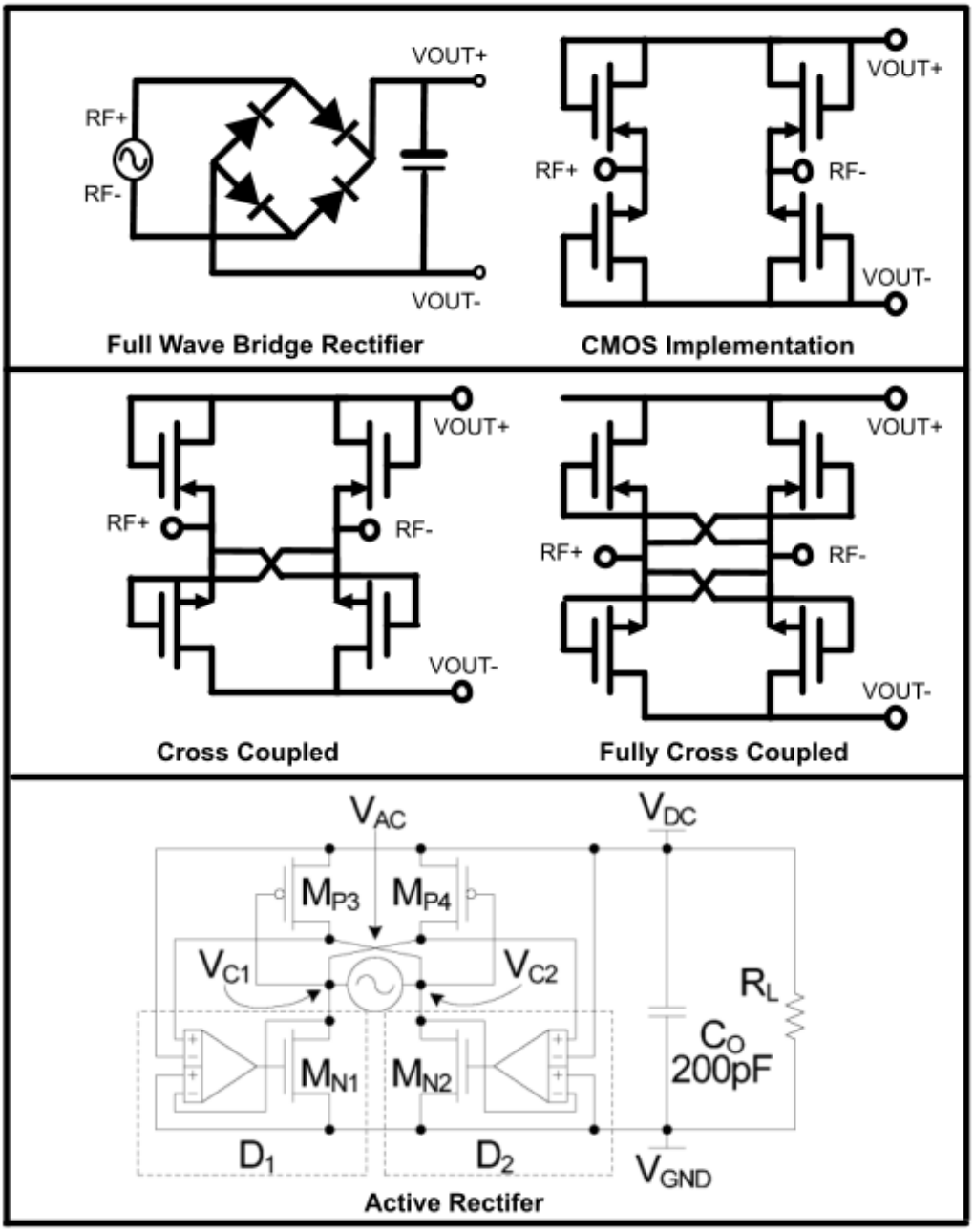


Figure 2.27: Different rectifier topologies starting with the basic full wave bridge rectifier along with its CMOS implementation above, cross coupled and full cross coupled implementation in the middle, and at the bottom the active rectifier toplogy as seen in [88].

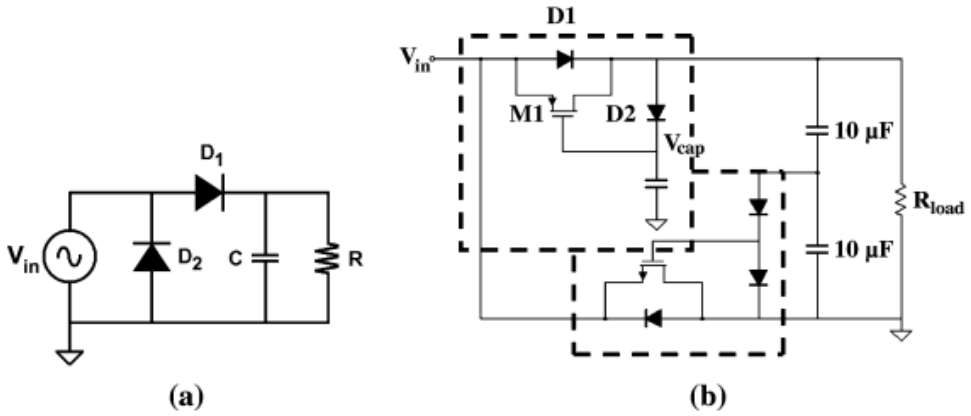


Figure 2.28: Demonstration of a bootstrapped capacitor rectifier circuit that reduces V_{th}. (a) Shows the original passive full-wave rectifer and (b) shows the modified bootstrapped circuit. Taken from [92].

Bulk regulated biasing is the technique whereby the bulk of the diode connected transistors are connected to the highest source voltage. This elimates the body effect on the diode transistors, reducing the rectifier dropout voltage and power consumption. [96][83] utilise this technique.

2.4.3 Bandgap Reference Architectures

The bandgap reference serves as a constant voltage reference irregardless of varying power supply or temperature. The output is usually based on the bandgap of silicon at 0V, which is 1.25V. Bandgap references have important applications with common examples like charge pumps, DC-DC converters and ADCs requiring one. A number of reviews have been published on the different architectures available [97][98][99][100]. The Widlar bandgap reference mentioned in the example earlier is a simple bandgap reference that improved upon previous references that utilised zener diodes, but still suffers from a poor power supply rejection ratio (PSRR).

For wirelessly powered circuits, in particular for switched outputs that require large instantaneous currents, a high PSRR is important for a smooth operation of the circuit. Hence, the literature would focus mainly on high PSRR architectures.

Giustolisi et al. demonstrate a fully CMOS implementation of a BGR that utilises the properties of subthreshold mosfets. The gate source voltage of a mosfet decreases linearly with temperature in the subthreshold range after biasing with a constant drain current. They achieve a output reference of 293mV at a supply voltage of 1.2V [101].

Boni et al. propose a current mode BGR architecture in particular for low supply voltage operation[102]. They mention multiple op amp architectures to reduce the minimum supply voltage to below 1V.

Lee et al. describe a BGR consisting of a start up circuit, PMOS two-stage opamp and a current control loop low dropout linear regulator [103]. The regular provides the operating supply voltage of the

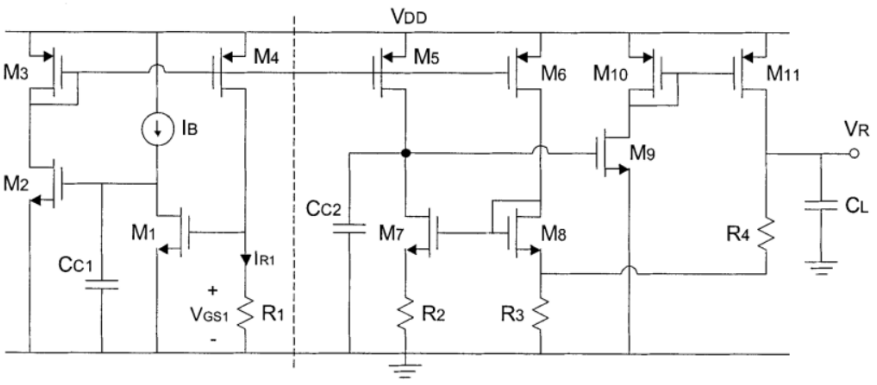


Figure 2.29: Fully CMOS bandgap reference described by Giustolisi et al. Taken from [101].

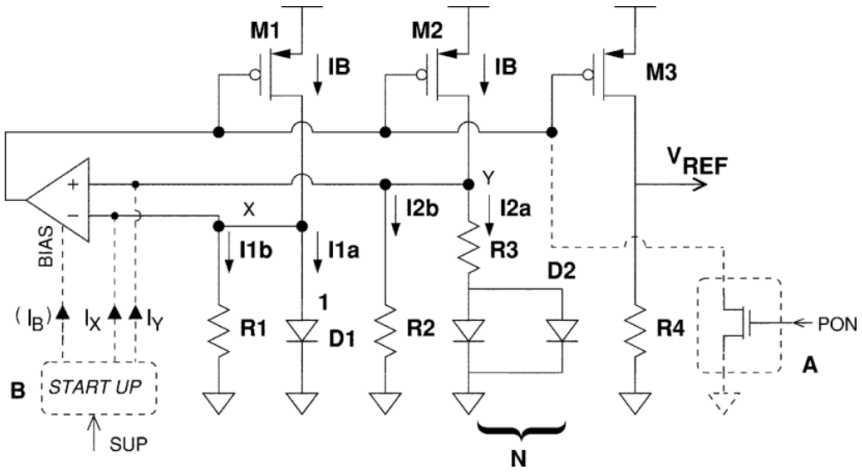


Figure 2.30: Current mode bandgap reference described by Boni et al. Taken from [102].

BGR in order to allow for a high PSRR BGR at a low power supply. They manage to achieve a PSRR of -64dB at a power dissipation of 1244mW.

Li et al. work shows a highly promising BGR, with especially high PSRR measured at -82.8dB [104]. Their circuits comprises of an additional power supply rejection enhancement stage in addition to the bandgap, opamp and start up circuits usually required. This enhancement stage works by increasing the loop gain and feedbacks the supply ripple into the PTAT loop at the bandgap core. This particularly improves the PSRR especially at high frequencies. Their derivation of the PSRR finds that a higher open loop gain of the opamp improves the PSRR at a low frequency but decreases at high frequency.

2.4.4 Low Dropout Regulator Architectures

Regulators play a key role in providing power supplies for electronic circuits. There are mainly two types of supply types: switched-mode power supplies and linear regulators. Switched-mode power supplies have the advantage of a high efficiency, at the cost of a larger amount of switching noise. They could also be stepped up or stepped down. On the other hand, linear regulators are lower in

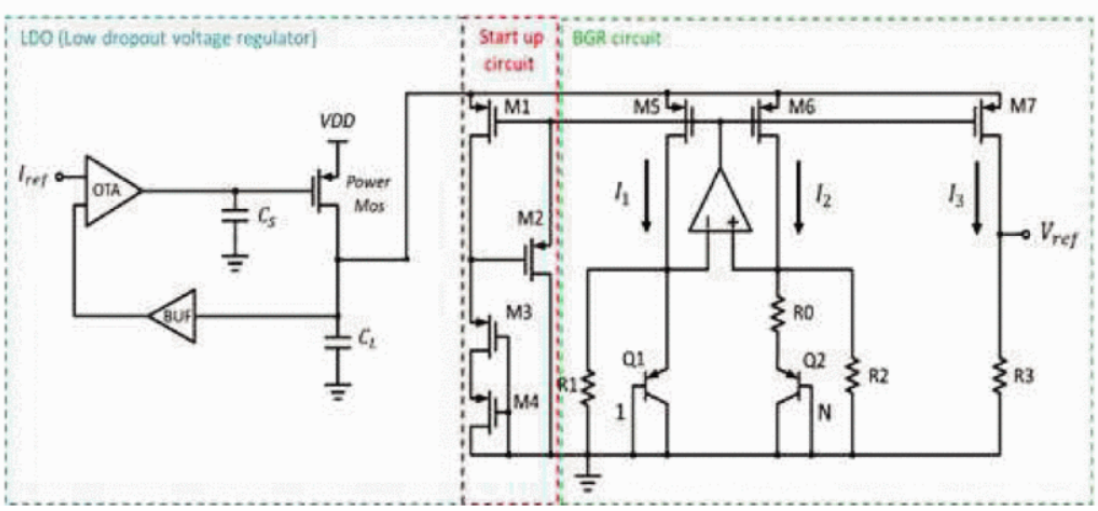


Figure 2.31: Bandgap reference described by Lee et al. Taken from [103].

Table 2.5: Comparison of Bandgap Reference Circuit Implementations

Ref	Tech(nm)	Vss(V)	Output(mV)	PSRR(dB)	Power Consumption (μW)
[101]	1200	1.2	293	NA	17.6
[102]	180	0.85	500	NA	9
[103]	350	2.9-3.3	800	-101@100Hz -47@1MHz	1244
[104]	600	2-5	389.8	-82.8@50kHz -70@100kHz	18
[105]	180	1.8	600	-79	NA

efficiency by comparison, and are always a step down converter. They offer a lower noise and lower output ripple.

The low dropout regulator(LDO) is a type of linear regulator that has a very low voltage potential between the power supply and the regulated output. This has been utilised particularly in batteries and allows for a much extended lifetime. The design of the LDO has been investigated extensively and multiple reviews exist [106] [107][108][109].

The literature on LDOs can be split into analog LDOs (ALDOs) and digital LDOs(DLDOs). ALDOs have disadvantages such as a larger power transistor, is more load dependent and are less reliable than their digital counterparts, but usually have less ripple in their output voltage and have a better PSRR performance[107]. As PSRR is an important feature for our design, the decision was taken to focus on ALDOs.

A generic analog LDO can be seen in Fig. 2.33. It will consist of a error amplifier, a PMOS pass transistor and a pair of resistors to serve as a feedback network. The transistor allows a large amount of current through, and hence has a large area for this purpose. The resistor feedback network serves to tweak the regulated voltage to the desired voltage level. The reference voltage in this scenario is

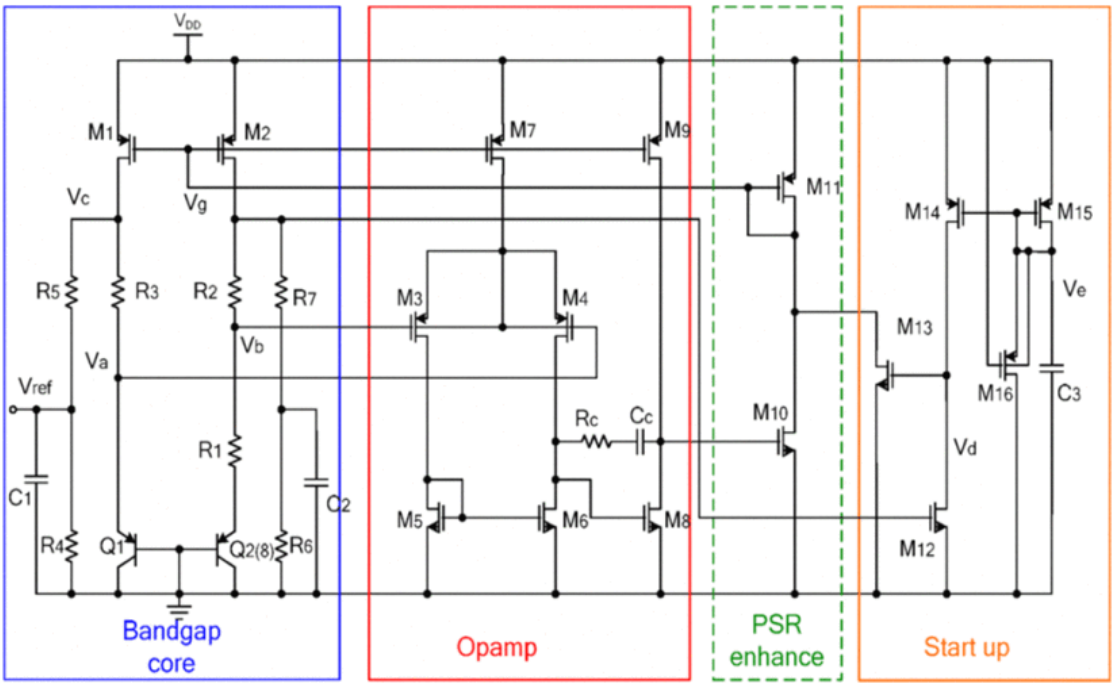


Figure 2.32: High PSRR bandgap reference described by Li et al. Taken from [104].

usually a BGR, but could also be a zener reference as well. The large size of the pass transistor results in a large gate capacitance that introduces a high slew rate that affects high frequency performance. This can be alleviated with a higher current throughput, but at the cost of a higher power consumption.

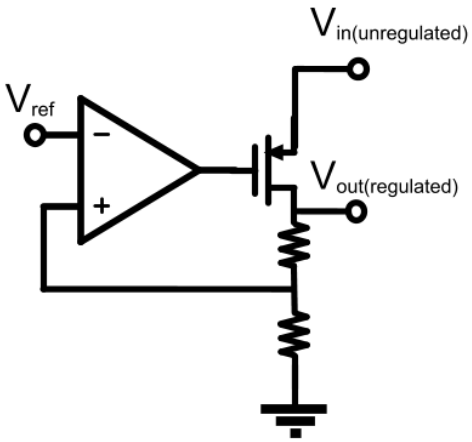


Figure 2.33: Low Dropout Regulator Example

As can be seen in this circuit, the LDO has a mutually exclusive relationship between a low power consumption and slow response time between the input voltage and the output voltage, slow slew rates and particularly low bandwidths. A key part of the design of the LDO involves an efficient feedback system for the closed-loop architecture, as well as a high PSRR with a quick response.

A simple and effective way to improve the PSRR of an LDO would be to add a large capacitor at the output. This would improve the performance by filtering out high frequency signals as well as transient performance. However, this comes at a cost of a large area required for the filtering, and

hence there has been a drive for capacitor-less LDOs.

A number of techniques have been explored to allow for a high PSRR. A multi-feedback structure is utilised in [110] to transform the regulator between 2-stage and 3-stage cascaded topologies depending on the load current. The LDO is decoupled from fluctutations in the power supply through the use of cascodes in [111]. This allows for the noise that is generated by the supply rails to be reduced at the output node. Ripple current injection to cancel output ripples has been performed in [112]. This has been also been explored for dynamic currents, whereby more current is injected when larger ripples are detected [113].

However, it is important to note that all these techniques have all been applied for specific ripple, input or output voltages. As such, it is imperative to develop an LDO for a specific input voltage of 50mV from our application.

2.4.5 Power-On-Reset

The power-on-reset(POR) circuit is required for the amperometry switching circuitry in order to ensure the circuit is in the correct state on boot up. The circuit works by providing a pulsed output when a threshold voltage is reached by the input power supply. The requirements for a POR circuit should be low power consumption, minimised area, ideally precise detection at the threshold voltage as well as insensitivity to temperature variations.

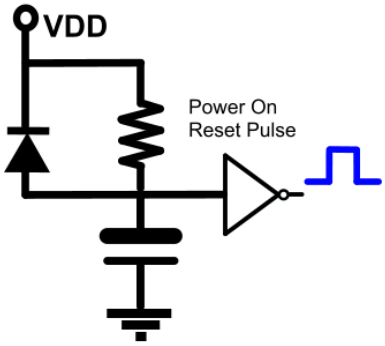


Figure 2.34: Basic RC Power-On-Reset Circuit adapted from [114]

A basic POR circuit is seen in Fig. 2.34 and consists of a resistor, capacitor, diode and inverter. As the supply voltage is switched on, the capacitor is slowly charged and its voltage increases. Once it reaches the threshold voltage set by the inverter, the output goes to 1 and a pulse is generated. This pulse width can be set by the values of R and C in the circuit.

The literature covers a number of power-on-reset that serve to improve on this basic example through designs that utilise a low quiescent current for low power consumption [115][116].

The POR circuit utilised is shown in Fig. 2.35. As the power supply increases, C_{POR} begins charging up until the threshold voltage of inverter 1 is reached. The low output of inverter 1 is then fed into inverter 2. After a slight delay, inverter 2 will switch M2 off, thus resulting in the current to C_{POR} being cut off. This results in the POR output signal remaining low.

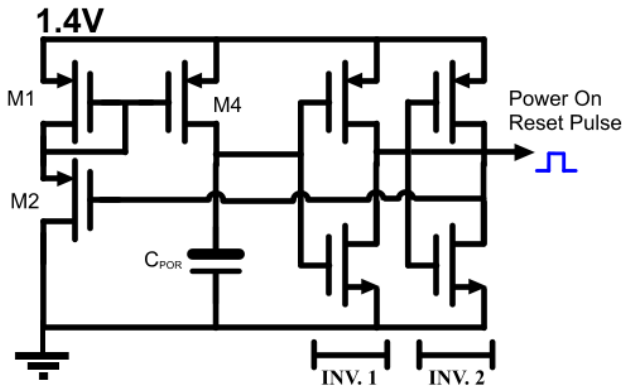


Figure 2.35: Power on reset(POR) circuit utilised in this work.

The circuit parameters are chosen as C_{POR} = 1pF for a output pulse of 1 μs, while the threshold voltages are set at 900mV.

2.4.6 Load Shift Keying

Digital modulation involves the process of embedding data into a carrier wave for transmitting signals. Various modulation techniques exist, of which the basic forms are the modulation of the phase, amplitude and the frequency of the signal. Fig.2.36 shows the 3 different examples and how they modulate the signal.

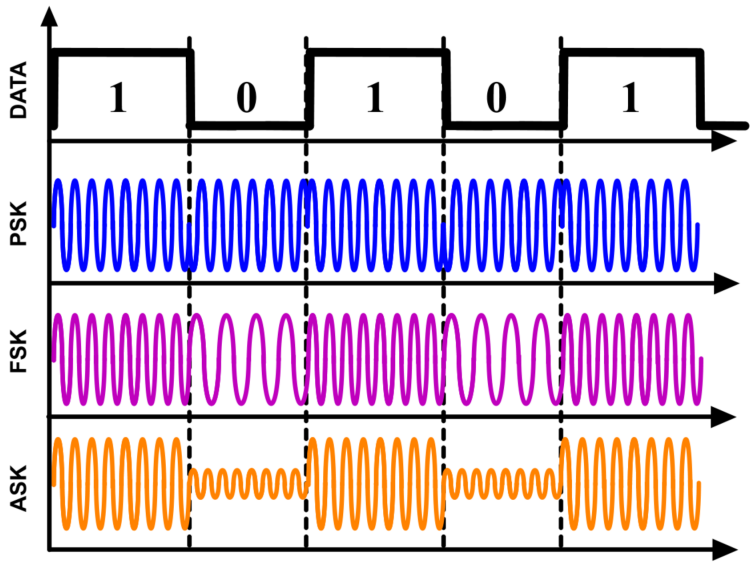


Figure 2.36: Digital modulation examples showing Frequency Shift Keying (FSK), Phase Shift Keying (PSK) and Amplitude Shift Keying(ASK). Load Shift Keying (LSK) is a modulation method similar to ASK.

Load shift keying is a modulation method similar to ASK relies upon the modulation of the resonant frequency between two inductors for communication. It is a fairly simple implementation which

works by the addition of impedance to a LC tank. This can take the form of switching in either series or parallel capacitors to the main capacitors, thus resulting in an impedance variation.

The value of the capacitors chosen are important as they affect the power transfer efficiency. In the case where a large impedance is added, the voltage ripple might be too high which affects the power transfer efficiency of the system. If it is too low, it might not be observed clearly on the transmitter side. Hence, a trade-off between either is chosen.

2.5 Chapter Summary

This chapter provides the background information on the electrochemical configuration for the electrodes in this work. It also provides a direction for the readout integrated circuits, as well as the wireless power and data transmission blocks.

The review for the electrochemical system describes the process of potentometry and amperometry, and focuses on the key factor when they are combined. This key factor is the presence of current flow for potentiometry when the theoretical assumption is there being no current flow. Hence, this will be examined further in Chapter 3 to analyse in deeper depth the effect of potentiometry in the presence of a current flow.

The review for the sensor front-end topologies provides an overview into all the different types of read out circuits available for potentiometry and amperometry. The overview shows there are clear advantages in terms of power consumption or simplicity of implementation for voltage controlled oscillators over analog-to-digital converters, and serves to aid the design for the potentiometric front-end. In addition to this, the current-to-frequency converter is chosen as the topology of choice for the amperometric front-end due to a lower power consumption as well. As power is limited for wireless systems, this is a particularly important specification that has to be met. This review will be key for the development of DAPPER in Chapter 4.

Lastly, the review on the wireless blocks shows a number of different implementations of wireless power systems in the literature. It also describes each of the key wireless blocks (rectifier, BGR, LDO, POR and LSK) in detail to explain their working mechanism as well as the various architectures available. This review is particularly important for evolving the front-end system into a wireless electrochemical system and will greatly aid the design of SPACEMAN in Chapter 5.

References

[1] S. Engineering. *5/3nm Wars Begin*. Oct. 2020.

[2] S. Carrara. “Body dust: Well beyond wearable and implantable sensors”. In: *IEEE Sensors Journal* 21.11 (2020), pp. 12398–12406.

[3] J. Kim et al. “Noninvasive alcohol monitoring using a wearable tattoo-based iontophoretic-biosensing system”. In: *Acs Sensors* 1.8 (2016), pp. 1011–1019.

[4] J. E. Koehne et al. “Carbon nanofiber electrode array for electrochemical detection of dopamine using fast scan cyclic voltammetry”. In: *Analyst* 136.9 (2011), pp. 1802–1805.

[5] M. A. Abrar et al. “Bendable electro-chemical lactate sensor printed with silver nano-particles”. In: *Scientific reports* 6 (2016), p. 30565.

[6] J. Kim et al. “Wearable salivary uric acid mouthguard biosensor with integrated wireless electronics”. In: *Biosensors and Bioelectronics* 74 (2015), pp. 1061–1068.

[7] A. J. Bard et al. *Electrochemical methods: fundamentals and applications*. Vol. 2. wiley New York, 1980.

[8] J. E. Choi et al. “Intraoral pH and temperature during sleep with and without mouth breathing.” In: *Journal of oral rehabilitation* 43 5 (2016), pp. 356–63.

[9] M. J. Schöning et al. “A dual amperometric/potentiometric FIA-based biosensor for the distinctive detection of organophosphorus pesticides”. In: *Sensors and Actuators B: Chemical* 95.1-3 (2003), pp. 291–296.

[10] K. Brunt. “Comparison between the performance of an electrochemical detector flow cell in a potentiometric and an amperometric measuring system using glucose as a test compound”. In: *Analyst* 107.1279 (1982), pp. 1261–1271.

[11] A. Sun, A. Venkatesh, and D. A. Hall. “A multi-technique reconfigurable electrochemical biosensor: Enabling personal health monitoring in mobile devices”. In: *IEEE transactions on biomedical circuits and systems* 10.5 (2016), pp. 945–954.

[12] H. Jiang et al. “A Sub-1 μW multiparameter injectable BioMote for continuous alcohol monitoring”. In: *2018 IEEE Custom Integrated Circuits Conference (CICC)*. IEEE. 2018, pp. 1–4.

[13] A. Cavallini et al. “Design, fabrication, and test of a sensor array for perspective biosensing in chronic pathologies”. In: *2012 IEEE Biomedical Circuits and Systems Conference (BioCAS)*. IEEE. 2012, pp. 124–127.

[14] Y. Xu et al. “Equivalent circuit models for a biomembrane impedance sensor and analysis of electrochemical impedance spectra based on support vector regression”. In: *Medical & biological engineering & computing* 57.7 (2019), pp. 1515–1524.

[15] M. Sharma et al. “Acquisition of Neural Action Potentials Using Rapid Multiplexing Directly at the Electrodes”. In: *Micromachines* 9 (Sept. 2018), p. 477.

[16] P. Steegstra and E. Ahlberg. “Influence of oxidation state on the pH dependence of hydrous iridium oxide films”. In: *Electrochimica acta* 76 (2012), pp. 26–33.

[17] Libretexts. *1.7: Ion Selective Electrode Analysis*. Jan. 2020. URL: `https://chem.libretexts.org/Bookshelves/AnalyticalChemistry`.

[18] E. Britannica. *Faraday’s Law of Electrochemistry*. Apr. 2020.

[19] I. Helm, L. Jalukse, and I. Leito. “Measurement uncertainty estimation in amperometric sensors: a tutorial review”. In: *Sensors* 10.5 (2010), pp. 4430–4455.

[20] M. W. Shinwari et al. “Microfabricated reference electrodes and their biosensing applications”. In: *Sensors* 10.3 (2010), pp. 1679–1715.

[21] S. Yang et al. “Electrochemical analysis of an anode-supported SOFC”. In: *Int. J. Electrochem. Sci* 8.2 (2013), pp. 2330–2344.

[22] É. Pergel et al. “Picomolar detection limits with current-polarized Pb2+ ion-selective membranes”. In: *Analytical chemistry* 73.17 (2001), pp. 4249–4253.

[23] E. Lindner, R. E. Gyurcsányi, and R. P. Buck. “Tailored transport through ion-selective membranes for improved detection limits and selectivity coefficients”. In: *Electroanalysis: An International Journal Devoted to Fundamental and Practical Aspects of Electroanalysis* 11.10-11 (1999), pp. 695–702.

[24] W. E. Morf et al. “Effects of controlled current on the response behavior of polymeric membrane ion-selective electrodes”. In: *Journal of Electroanalytical Chemistry* 526.1-2 (2002), pp. 19–28.

[25] H. Karimi-Maleh et al. “A critical review on the use of potentiometric based biosensors for biomarkers detection”. In: *Biosensors and Bioelectronics* 184 (2021), p. 113252.

[26] J. Wang. “Amperometric biosensors for clinical and therapeutic drug monitoring: a review”. In: *Journal of pharmaceutical and biomedical analysis* 19.1-2 (1999), pp. 47–53.

[27] A.-E. Radi and M. R. Abd-Ellatief. “Electrochemical aptasensors: current status and future perspectives”. In: *Diagnostics* 11.1 (2021), p. 104.

[28] T. Kang et al. “A 1.74. 12 mm 3 Fully Integrated pH Sensor for Implantable Applications using Differential Sensing and Drift-Compensation”. In: *2019 Symposium on VLSI Circuits*. IEEE. 2019, pp. C310–C311.

[29] M. Douthwaite et al. “A thermally powered ISFET array for on-body pH measurement”. In: *IEEE transactions on biomedical circuits and systems* 11.6 (2017), pp. 1324–1334.

[30] H. Cao et al. “An implantable, batteryless, and wireless capsule with integrated impedance and pH sensors for gastroesophageal reflux monitoring”. In: *IEEE Transactions on Biomedical Engineering* 59.11 (2012), pp. 3131–3139.

[31] D. Ma, C. Mason, and S. S. Ghoreishizadeh. “A wireless system for continuous in-mouth pH monitoring”. In: *Biomedical Circuits and Systems Conference (BioCAS), 2017 IEEE*. IEEE. 2017, pp. 1–4.

[32] N. Gay and W.-J. Fischer. “Ultra-low-power RFID-based sensor mote”. In: *SENSORS, 2010 IEEE*. IEEE. 2010, pp. 1293–1298.

[33] W. C. Lai, J. F. Huang, and C. G. Hsieh. “An 8-bit 20 MS/s successive approximation register analog-to-digital converter for wireless intelligent control and information processing”. In: *Fifth International Conference on Intelligent Control and Information Processing*. 2014, pp. 115–117.

[34] X. Zhou, Y. Zhang, and Y. Su. “An 8-bit 35-MS/s successive approximation register ADC”. In: *2015 IEEE International Conference on Progress in Informatics and Computing (PIC)*. IEEE. 2015, pp. 531–533.

[35] D. Arbet et al. “Voltage-to-Frequency Converter for Ultra-Low-Voltage Applications”. In: *2019 42nd International Convention on Information and Communication Technology, Electronics and Microelectronics (MIPRO)*. 2019, pp. 53–58.

[36] S. Aslanzadeh et al. “A Low-Power Voltage-Clamped CMOS pH to Frequency Sensor”. In: *2019 IEEE International Symposium on Circuits and Systems (ISCAS)*. 2019, pp. 1–5.

[37] C. Azcona et al. “Ratiometric voltage-to-frequency converter for long-life autonomous portable equipment”. In: *IEEE Sensors Journal* 13.6 (2013), pp. 2382–2390.

[38] M. R. Valero et al. “CMOS Voltage-to-Frequency Converter With Temperature Drift Compensation”. In: *IEEE Transactions on Instrumentation and Measurement* 60.9 (2011), pp. 3232–3234.

[39] C. Azcona et al. “A CMOS micropower voltage-to-frequency converter for portable applications”. In: *2011 7th Conference on Ph.D. Research in Microelectronics and Electronics*. 2011, pp. 141–144.

[40] M. Crescentini et al. “Noise Limits of CMOS Current Interfaces for Biosensors: A Review”. In: *IEEE Transactions on Biomedical Circuits and Systems* 8.2 (2014), pp. 278–292.

[41] D. Kim et al. “Noise Analysis and Performance Comparison of Low Current Measurement Systems for Biomedical Applications”. In: *IEEE Transactions on Biomedical Circuits and Systems* 7.1 (2013), pp. 52–62.

[42] H. Li et al. “CMOS electrochemical instrumentation for biosensor microsystems: A review”. In: *Sensors* 17.1 (2017), p. 74.

[43] D. Ying and D. A. Hall. “Current Sensing Front-Ends: A Review and Design Guidance”. In: *IEEE Sensors Journal* (2021).

[44] Y.-J. Yoon et al. “Microfluidics biosensor chip with integrated screen-printed electrodes for amperometric detection of nerve agent”. In: *Sensors and Actuators B: Chemical* 198 (2014), pp. 233–238.

[45] S. G. Bratsch. “Standard electrode potentials and temperature coefficients in water at 298.15 K”. In: *Journal of Physical and Chemical Reference Data* 18.1 (1989), pp. 1–21.

[46] L. Busoni, M. Carla, and L. Lanzi. “A comparison between potentiostatic circuits with grounded work or auxiliary electrode”. In: *Review of scientific instruments* 73.4 (2002), pp. 1921–1923.

[47] S. M. Martin et al. “A CMOS-integrated microinstrument for trace detection of heavy metals”. In: *IEEE journal of solid-state circuits* 40.12 (2005), pp. 2777–2786.

[48] E. Lauwers et al. “A CMOS multiparameter biochemical microsensor with temperature control and signal interfacing”. In: *IEEE Journal of solid-state circuits* 36.12 (2001), pp. 2030–2038.

[49] P. M. Levine et al. “Active CMOS sensor array for electrochemical biomolecular detection”. In: *IEEE Journal of Solid-State Circuits* 43.8 (2008), pp. 1859–1871.

[50] M. Carminati et al. “Low-noise single-chip potentiostat for nano-bio-electrochemistry over a 1MHz bandwidth”. In: *2009 16th IEEE International Conference on Electronics, Circuits and Systems-(ICECS 2009)*. IEEE. 2009, pp. 952–955.

[51] S. M. Martin et al. “A fully differential potentiostat”. In: *IEEE Sensors Journal* 9.2 (2009), pp. 135–142.

[52] E. Ghodsevali et al. “High accuracy and sensitivity differential potentiostat with amplifier-based error cancellation feedback loop”. In: *2015 IEEE Biomedical Circuits and Systems Conference (BioCAS)*. 2015, pp. 1–4.

[53] M. M. Ahmadi and G. A. Jullien. “Current-mirror-based potentiostats for three-electrode amperometric electrochemical sensors”. In: *IEEE Transactions on Circuits and Systems I: Regular Papers* 56.7 (2008), pp. 1339–1348.

[54] Y.-T. Liao et al. “A 3-μW CMOS Glucose Sensor for Wireless Contact-Lens Tear Glucose Monitoring”. In: *IEEE Journal of Solid-State Circuits* 47.1 (2012), pp. 335–344.

[55] M. H. Nazari, M. Mujeeb-U-Rahman, and A. Scherer. “An implantable continuous glucose monitoring microsystem in 0.18 μm CMOS”. In: *VLSI Circuits Digest of Technical Papers, 2014 Symposium on*. IEEE. 2014, pp. 1–2.

[56] R. Genov et al. “16-channel integrated potentiostat for distributed neurochemical sensing”. In: *IEEE Transactions on Circuits and Systems I: Regular Papers* 53.11 (2006), pp. 2371–2376.

[57] H. M. Jafari and R. Genov. “Chopper-Stabilized Bidirectional Current Acquisition Circuits for Electrochemical Amperometric Biosensors”. In: *IEEE Transactions on Circuits and Systems I: Regular Papers* 60.5 (2013), pp. 1149–1157.

[58] B. Razavi. “The Transimpedance Amplifier [A Circuit for All Seasons]”. In: *IEEE Solid-State Circuits Magazine* 11.1 (2019), pp. 10–97.

[59] A. Gore et al. “A multichannel femtoampere-sensitivity potentiostat array for biosensing applications”. In: *IEEE Transactions on Circuits and Systems I: Regular Papers* 53.11 (2006), pp. 2357–2363.

[60] M. Stanacevic et al. “VLSI potentiostat array with oversampling gain modulation for wide-range neurotransmitter sensing”. In: *IEEE Transactions on Biomedical Circuits and Systems* 1.1 (2007), pp. 63–72.

[61] C.-L. Hsu and D. A. Hall. “A current-measurement front-end with 160dB dynamic range and 7ppm INL”. In: *2018 IEEE International Solid-State Circuits Conference-(ISSCC)*. IEEE. 2018, pp. 326–328.

[62] H. Dai et al. “A review and design of the on-chip rectifiers for RF energy harvesting”. In: *2015 IEEE International Wireless Symposium (IWS 2015)*. IEEE. 2015, pp. 1–4.

[63] S. Dai et al. “A 155-dB dynamic range current measurement front end for electrochemical biosensing”. In: *IEEE transactions on biomedical circuits and systems* 10.5 (2016), pp. 935–944.

[64] Y. Liu, L. Leene, and T. Constandinou. “An Oscillator Based Potentiostat with Switch-Cap Feedback for Current Sensing Applications”. In: *2019 IEEE International Symposium on Circuits and Systems (ISCAS)*. IEEE. 2019, pp. 1–4.

[65] C. Sauer et al. “Power harvesting and telemetry in CMOS for implanted devices”. In: *IEEE Transactions on Circuits and Systems I: Regular Papers* 52.12 (2005), pp. 2605–2613.

[66] T. Akin, K. Najafi, and R. M. Bradley. “A wireless implantable multichannel digital neural recording system for a micromachined sieve electrode”. In: *IEEE Journal of solid-state circuits* 33.1 (1998), pp. 109–118.

[67] K. M. Silay, C. Dehollain, and M. Declercq. “A closed-loop remote powering link for wireless cortical implants”. In: *IEEE Sensors Journal* 13.9 (2013), pp. 3226–3235.

[68] M. Catrysse, B. Hermans, and R. Puers. “An inductive power system with integrated bi-directional data-transmission”. In: *Sensors and Actuators A: Physical* 115.2 (2004), pp. 221–229.

[69] J. Olivo, S. Carrara, and G. De Micheli. “Energy harvesting and remote powering for implantable biosensors”. In: *IEEE Sensors Journal* 11.7 (2011), pp. 1573–1586.

[70] G. Melia. “Electromagnetic Absorption by the Human Body from 1-15 GHz”. PhD thesis. University of York, 2013.

[71] M. Zargham and P. G. Gulak. “Maximum achievable efficiency in near-field coupled power-transfer systems”. In: *IEEE Transactions on Biomedical Circuits and Systems* 6.3 (2012), pp. 228–245.

[72] U.-M. Jow and M. Ghovanloo. “Design and optimization of printed spiral coils for efficient transcutaneous inductive power transmission”. In: *IEEE Transactions on biomedical circuits and systems* 1.3 (2007), pp. 193–202.

[73] P. Feng et al. “Chip-Scale Coils for Millimeter-Sized Bio-Implants”. In: *IEEE transactions on biomedical circuits and systems* 99 (2018), pp. 1–12.

[74] M. Meng and M. Kiani. “Design and optimization of ultrasonic wireless power transmission links for millimeter-sized biomedical implants”. In: *IEEE transactions on biomedical circuits and systems* 11.1 (2017), pp. 98–107.

[75] H. Rahmani and A. Babakhani. “A wireless power receiver with an on-chip antenna for millimeter-size biomedical implants in 180 nm SOI CMOS”. In: *Microwave Symposium (IMS), 2017 IEEE MTT-S International*. IEEE. 2017, pp. 300–303.

[76] M. Zargham and P. G. Gulak. “Fully integrated on-chip coil in 0.13 CMOS for wireless power transfer through biological media”. In: *IEEE transactions on biomedical circuits and systems* 9.2 (2015), pp. 259–271.

[77] L. B. Leene et al. “Autonomous SoC for Neural Local Field Potential Recording in mm-Scale Wireless Implants”. In: *Circuits and Systems (ISCAS), 2018 IEEE International Symposium on*. IEEE. 2018, pp. 1–5.

[78] A. Agarwal et al. “A 4μW, ADPLL-based implantable amperometric biosensor in 65nm CMOS”. In: *VLSI Circuits, 2017 Symposium on*. IEEE. 2017, pp. C108–C109.

[79] A. S. Poon, S. O’Driscoll, and T. H. Meng. “Optimal frequency for wireless power transmission into dispersive tissue”. In: *IEEE Transactions on Antennas and Propagation* 58.5 (2010), pp. 1739–1750.

[80] H. Dai et al. “A review and design of the on-chip rectifiers for RF energy harvesting”. In: *2015 IEEE International Wireless Symposium (IWS 2015)*. 2015, pp. 1–4.

[81] T. Ngo, A.-D. Huang, and Y.-X. Guo. “Analysis and Design of a Reconfigurable Rectifier Circuit for Wireless Power Transfer”. In: *IEEE Transactions on Industrial Electronics* 66.9 (2019), pp. 7089–7098.

[82] S. Roy et al. “A Comprehensive Review on Rectifiers, Linear Regulators, and Switched-Mode Power Processing Techniques for Biomedical Sensors and Implants Utilizing in-Body Energy Harvesting and External Power Delivery”. In: *IEEE Transactions on Power Electronics* 36.11 (2021), pp. 12721–12745.

[83] S. S. Hashemi, M. Sawan, and Y. Savaria. “A High-Efficiency Low-Voltage CMOS Rectifier for Harvesting Energy in Implantable Devices”. In: *IEEE Transactions on Biomedical Circuits and Systems* 6.4 (2012), pp. 326–335.

[84] U. Karthaus and M. Fischer. “Fully integrated passive UHF RFID transponder IC with 16.7-W minimum RF input power”. In: *IEEE Journal of Solid-State Circuits* 38.10 (2003), pp. 1602–1608.

[85] P. Rakers et al. “Secure contactless smartcard ASIC with DPA protection”. In: *Proceedings of the IEEE 2000 Custom Integrated Circuits Conference (Cat. No.00CH37044)*. 2000, pp. 239–242.

[86] A. Facen and A. Boni. “Power Supply Generation in CMOS Passive UHF RFID Tags”. In: *2006 Ph.D. Research in Microelectronics and Electronics*. 2006, pp. 33–36.

[87] J. Hu and H. Min. “A low power and high performance analog front end for passive RFID transponder”. In: *Fourth IEEE Workshop on Automatic Identification Advanced Technologies (AutoID’05)*. 2005, pp. 199–204.

[88] Y.-H. Lam, W.-H. Ki, and C.-Y. Tsui. “Integrated Low-Loss CMOS Active Rectifier for Wirelessly Powered Devices”. In: *IEEE Transactions on Circuits and Systems II: Express Briefs* 53.12 (2006), pp. 1378–1382.

[89] S. Atluri and M. Ghovanloo. “Incorporating Back Telemetry in a Full-Wave CMOS Rectifier for RFID and Biomedical Applications”. In: *2007 IEEE International Symposium on Circuits and Systems*. 2007, pp. 801–804.

[90] C. Peters et al. “CMOS Integrated Highly Efficient Full Wave Rectifier”. In: *2007 IEEE International Symposium on Circuits and Systems*. 2007, pp. 2415–2418.

[91] T. Lehmann and Y. Moghe. “On-chip active power rectifiers for biomedical applications”. In: *2005 IEEE International Symposium on Circuits and Systems*. 2005, 732–735 Vol. 1.

[92] T. Le et al. “Piezoelectric micro-power generation interface circuits”. In: *IEEE Journal of Solid-State Circuits* 41.6 (2006), pp. 1411–1420.

[93] Q. U. Ain et al. “A High-Efficiency Rectifier with bootstrapping technique for Wireless Power Transfer System”. In: *2021 IEEE International Conference on Consumer Electronics-Asia (ICCE-Asia)*. 2021, pp. 1–3.

[94] M. Ebrahimian, K. El-Sankary, and E. El-Masry. “Enhanced RF to DC CMOS rectifier with capacitor-bootstrapped transistor”. In: *Proceedings of 2010 IEEE International Symposium on Circuits and Systems*. 2010, pp. 1655–1658.

[95] C.-S. A. Gong, S.-W. Li, and M.-T. Shiue. “A bootstrapped comparator-switched active rectifying circuit for wirelessly powered integrated miniaturized energy sensing systems”. In: *Sensors* 19.21 (2019), p. 4714.

[96] P. Favrat, P. Deval, and M. Declercq. “A high-efficiency CMOS voltage doubler”. In: *IEEE Journal of Solid-State Circuits* 33.3 (1998), pp. 410–416.

[97] V. Hande and M. Shojaei Baghini. “Survey of Bandgap and Non-bandgap based Voltage Reference Techniques”. In: *Scientia Iranica* 23.6 (2016), pp. 2845–2861.

[98] K. Pandey, A. Karwal, and S. M. Ranjan. “Review of Bandgap Voltage Reference for Analog and Mixed Signal Circuit”. In: (2016).

[99] J. Catalina et al. “Review of Bandgap Voltage Reference Architectures for Long-Range Passive RFID Applications”. In: *2019 XXXIV Conference on Design of Circuits and Integrated Systems (DCIS)*. IEEE. 2019, pp. 1–5.

[100] P. Kinget et al. “Voltage references for ultra-low supply voltages”. In: *2008 IEEE Custom Integrated Circuits Conference*. 2008, pp. 715–720.

[101] G. Giustolisi et al. “A low-voltage low-power voltage reference based on subthreshold MOSFETs”. In: *IEEE Journal of Solid-State Circuits* 38.1 (2003), pp. 151–154.

[102] A. Boni. “Op-amps and startup circuits for CMOS bandgap references with near 1-V supply”. In: *IEEE Journal of Solid-State Circuits* 37.10 (2002), pp. 1339–1343.

[103] M.-C. Lee and S.-Z. Chang. “Implementation of a High PSRR Low Power CMOS Bandgap Voltage Reference Circuit”. In: *2018 Progress in Electromagnetics Research Symposium (PIERS-Toyama)*. 2018, pp. 2121–2128.

[104] W. Li, R. Yao, and L. Guo. “A low power CMOS bandgap voltage reference with enhanced power supply rejection”. In: *2009 IEEE 8th International Conference on ASIC*. 2009, pp. 300–304.

[105] A. Dey and T. K. Bhattacharyya. “A CMOS bandgap reference with high PSRR and improved temperature stability for system-on-chip applications”. In: *2011 IEEE International Conference of Electron Devices and Solid-State Circuits*. 2011, pp. 1–2.

[106] S. K. Lau, K. N. Leung, and P. Mok. “Analysis of low-dropout regulator topologies for low-voltage regulation”. In: *2003 IEEE Conference on Electron Devices and Solid-State Circuits (IEEE Cat. No.03TH8668)*. 2003, pp. 379–382.

[107] M. A. Sobhan Bhuiyan et al. “CMOS Low-Dropout Voltage Regulator Design Trends: An Overview”. In: *Electronics* 11.2 (2022), p. 193.

[108] M. Huang, Y. Lu, and R. P. Martins. “Review of Analog-Assisted-Digital and Digital-Assisted-Analog Low Dropout Regulators”. In: *IEEE Transactions on Circuits and Systems II: Express Briefs* 68.1 (2021), pp. 24–29.

[109] S. Roy et al. “A comprehensive review on rectifiers, linear regulators and switched-mode power processing techniques for biomedical sensors and implants utilizing in-body energy harvesting and external power delivery”. In: *IEEE Transactions on Power Electronics* (2021).

[110] S. Chong and P. K. Chan. “A 0.9-/spl mu/A Quiescent Current Output-Capacitorless LDO Regulator With Adaptive Power Transistors in 65-nm CMOS”. In: *IEEE Transactions on Circuits and Systems I: Regular Papers* 60.4 (2013), pp. 1072–1081.

[111] V. Gupta and G. Rincon-Mora. “A low dropout, CMOS regulator with high PSR over wideband frequencies”. In: *2005 IEEE International Symposium on Circuits and Systems*. 2005, 4245–4248 Vol. 5.

[112] M. El-Nozahi et al. “High PSR Low Drop-Out Regulator With Feed-Forward Ripple Cancellation Technique”. In: *IEEE Journal of Solid-State Circuits* 45.3 (2010), pp. 565–577.

[113] M. Ho and K. N. Leung. “Dynamic Bias-Current Boosting Technique for Ultralow-Power Low-Dropout Regulator in Biomedical Applications”. In: *IEEE Transactions on Circuits and Systems II: Express Briefs* 58.3 (2011), pp. 174–178.

[114] L. Xinquan et al. “A low quiescent current and reset time adjustable power-on reset circuit”. In: *2005 6th International Conference on ASIC*. Vol. 2. 2005, pp. 559–562.

[115] T. Yasuda, M. Yamamoto, and T. Nishi. “A power-on reset pulse generator for low voltage applications”. In: *ISCAS 2001. The 2001 IEEE International Symposium on Circuits and Systems (Cat. No.01CH37196)*. Vol. 4. 2001, 599–601 vol. 4.

[116] S. Wadhwa, G. Siddhartha, and A. Gaurav. “Zero steady state current power-on-reset circuit with brown-out detector”. In: *19th International Conference on VLSI Design held jointly with 5th International Conference on Embedded Systems Design (VLSID’06)*. 2006, 6 pp.-.

Chapter 3

Concurrent Sensing of Amperometry and Potentiometry

Concurrent sensing of amperometry and potentiometry is a relatively novel concept that will be explored in this chapter. This chapter will describe the rationale for concurrent sensing, before describing a brief theoretical background into electrochemistry concepts. A discussion onto an experiment done to validate the concurrent sensing setup will be shown, before the design of a CMOS-based concurrent sensing front end circuit is given. This results and methods provided in this work have been published in IEEE Sensors 2021[1].

3.1 Experiment Design and Materials

As mentioned in Chapter 2, a key part of the newly proposed combined configuration would be to use a shared reference electrode for the concurrently sensing potentiometry and amperometry. To compare the efficacy of using a shared reference electrode, the results for the classical measurement techniques will be compared to the results obtained for the combined reference electrode configuration.

The combined circuit consists of the amperometric circuit along with the ISE sensing op-amp of the potentiometric circuit. This combined configuration contains the ISE utilising the reference of the open loop circuit.

3.1.1 Materials

Buffer salts of pH 3, 5, 7 and 9 were obtained from Sigma-Aldrich to provide the calibration and tests for potentiometric measurements. 30% H_2O_2 (1.11g/cm3) from Fisher Bioreagents is used for amperometry.

[1] **D. Ma**, S. S. Ghoreishizadeh and P. Georgiou, "Concurrent Potentiometric and Amperometric Sensing With Shared Reference Electrodes," in IEEE Sensors Journal, vol. 21, no. 5, pp. 5720-5727, 1 March1, 2021, doi: 10.1109/JSEN.2020.3039567.

An Ag/AgCl glass reference electrode with a porous teflon tip purchased from CH Instruments (CHI111)[1] is used as the reference electrode for the separate and the combined topologies. The 550 from Dropsens with a platinum CE and WE were used for amperometry [2].

Iridium Oxide electrodes have been chosen as the potentiometric sensing electrode for pH. It has been shown to have a life span of up to 2.5 years[3] - which makes it particularly useful for ensuring sensitivity across the span of the experiment. These electrodes are fabricated for the experiments. Iridium wire (178 μm diameter, 99.9% purity) is obtained from ADVENT RM, along with sulphuric acid (5%V/V) from Sigma Aldrich.

3.1.2 Equipment

A Sentron SI400 pH meter[4] with an accuracy of 0.01 pH was used as a gold standard for pH measurement. A CH700E Potentistat from CH Instruments [5] is used for the fabrication of the IrOx pH sensor. A Saleae logic analyzer with 8 inputs is used in tandem with multimeters to monitor the voltages from the various outputs of the circuit.

3.1.3 IrOx Electrode Fabrication

The IrOx based pH sensor is used due to their high sensitivity, stability and life time. We fabricated the IrOx electrode in house with the following recipe: Iridium wire (178 μm diameter, 99.9% purity) is oxidised through immersion in a sulfuric acid solution (5%V/V). During the oxidation phase, the Ag/AgCl glass reference electrode along with a platinum counter electrode are immersed inside the sulfuric acid solution. Repetitive cyclic voltammetries between -0.2 V and 1.2 V at a 1.4 V/s scan rate is performed on the three electrodes for 3 hours, with the iridium wire serving as the WE.

The oxidised wire is next calibrated in order to obtain the pH sensitivity. This is done through the use of pH buffers. The final fabricated wire is then soldered to a 28 AWG wire as a connection to the sensing circuitry. This connection is covered in Araldite epoxy and the entire surface sealed with a heat shrink to reduce the effect of any contamination of the electrode surface.

3.1.4 Sensing Circuitry

The configuration of electrodes and connection with the readout electronics for the separate and combined experiments is shown in Fig. 3.1. The op-amp utilised for all circuits is the LMC6042 [6] from Texas Instruments. This op-amp is chosen for its ultra-low input leakage current, which helps prevent any possible drift from the reference electrodes.

For the potentiometric circuit, a $\frac{VDD}{2}$ voltage is applied to the reference electrode to allow for a maximum input swing for the ISE detection range.

In the separate amperometric circuit (see Fig. 3.1A), a transimpedance amplifier is used to detect the current flowing into the WE. The WE is biased at 0.65V higher than $\frac{VDD}{2}$ to activate the redox reaction

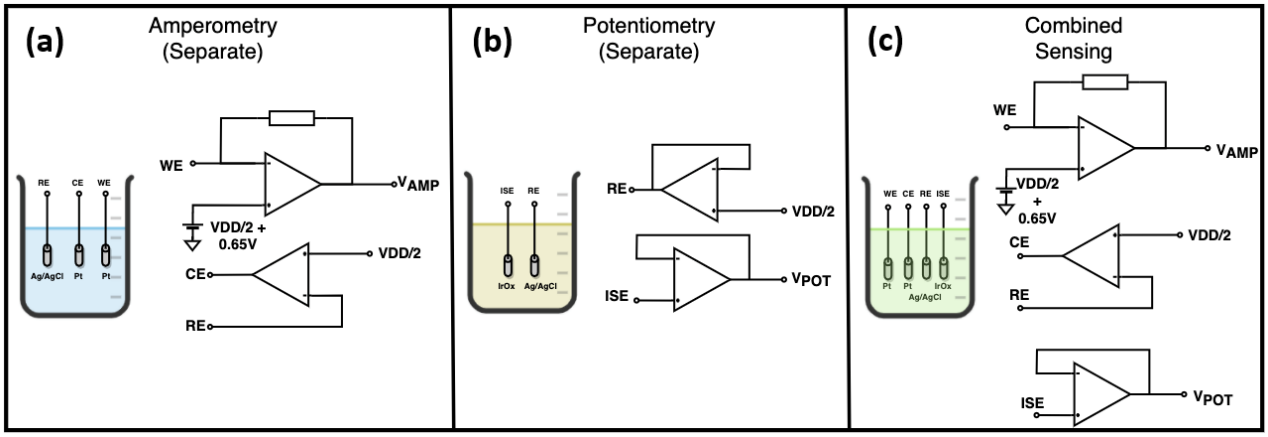


Figure 3.1: Experiment Circuitry employed for this experiment with the separate potentiometric and amperometric modes along with the combined setup. The chosen electrodes along with their materials are also displayed.

of H_2O_2[7], with the CE connected to the output of the op-amp to provide the current necessary for the RE to be held at the $\frac{VDD}{2}$ value.

3.2 Experimental Results

3.2.1 Combined vs separate measurement: sensor sensitivity and correlation

3.2.1.1 Potentiometric

The aim of this experiment is to determine if there is any difference in the sensitivity of the pH sensor between zero and non-zero cell current scenarios. The experiment is held in a well-ventilated lab where the room temperature is maintained relatively constant. The protocol is as follows:

1. 20ml of pH buffer solutions prepared for pH 3, 5, 7 and 9. All solutions are 0 mM concentration of H_2O_2.
2. V_{pot} and RE were measured at all four pH buffer solutions with the setup of Fig. 3.1B.
3. The voltages at V_{pot} and RE were measured again this time using the setup shown in Fig. 3.1C.
4. Experiment repeated thrice to determine error ratio.

The measured potentiometric voltages together with the measured amperometric current in the combined setup are presented in Fig. 3.2. The error bars represent the max and min of the measured data points. The results for the combined potentiometry display a larger error ratio. A cross correlation of 0.9981 between both sets of results indicate a clear similarity between the separate and combined configurations. The amperometric current generated is purely from the pH buffer (i.e not due to H_2O_2), and shows an increment for higher pH buffers.

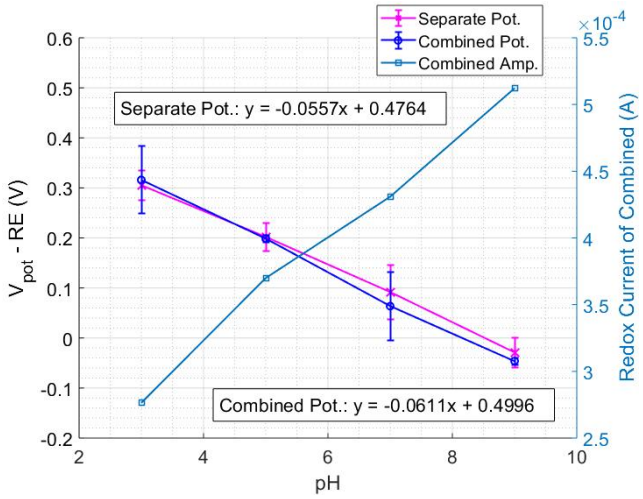


Figure 3.2: Separate vs Combined potentiometric readings (error bars represent max and min values from three trials). Combined amperometric reading is shown on the plot, with the axis on the right. Cross correlation of 0.9981 observed. The entirety of this experiment is with no added H_2O_2, which means the cell current is entirely due to background current.

3.2.1.2 Amperometric

The purpose of this set of experiments is to determine the sensitivity of the amperometric sensor, as well as to determine the correlation between the separate and combined settings of the amperometric outputs. The protocols are:

1. 20ml of pH 3 solution prepared on a magnetic stirrer (rpm 200)
2. Increasing concentrations of 0.01M of H_2O_2 is added to the solution.
3. Measurements of the cell current is taken for the separate configuration as shown in Fig. 3.1A for V_{amp}, CE and RE up to the full range of concentration of 0.1M.
4. Measurements of the cell current is taken for the combined configuration (Fig. 3.1C) for V_{amp}, CE and RE up to 0.1M.
5. Experiment repeated thrice to determine error ratio.

The amperometric measurements for both the separate and combined are presented in Fig. 3.3. A logarithmic fit is applied, with the max and min of the three experiments shown. The results show a high correlation of 0.9959, which demonstrate that the amperometric measurement is unaffected by the addition of the ISE.

3.2.2 Combined Configuration: Concurrent measurements for varying pH and H_2O_2 concentrations

To determine whether potentiometric measurement shows a difference in the presence of a variable cell current, we configure the analyte in the setup shown in Fig. 3.1C such that the amperometric

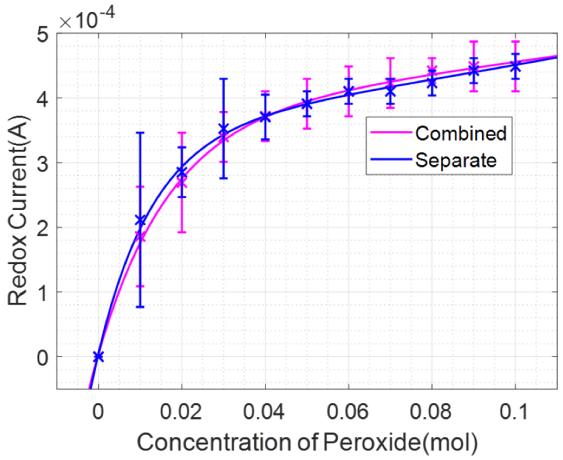


Figure 3.3: Separate vs Combined amperometric readings averaged across three trials with a cross correlation of 0.9959 observed and background current removed. The maximum and minimum of the three measured samples are shown in the plot with a logarithmic fit. The tests are performed at a fixed pH 3 buffer.

current varies (by changing H_2O_2 concentration) for fixed pH buffers. To this aim we designed and conducted two experiments described in this section.

3.2.2.1 Amperometric Measurements

This experiment serves to showcase the varying cell current for varying H_2O_2 concentrations in different pH buffers. The protocol is as follows:

1. 20ml of pH 3, 5, 7 and 9 solution prepared on a magnetic stirrer (rpm 200)
2. Increasing concentrations of 0.01M of H_2O_2 is added to the solution.
3. Sentron pH meter is used as the gold standard pH meter.
4. Measurements of amperometry taken for the combined configuration (see Fig. 3.1C) for V_{amp}, CE and RE for the full range of concentration as shown in Fig. 3.4A.

The measured results for amperometry are shown in Fig. 3.4A. All measurements were performed on the same day. The results show that the cell current variation differs for different pH buffers. This affirms that the cell current varies for increasing peroxide levels, although for lower pH levels (3,5) the variation in the cell current is much higher as compared to the high pH levels (7,9). With it being clear that there is a cell current generated from increasing peroxide levels, the next experiment will aim to determine if there is a variation in the potentiometric results after this cell current is added.

3.2.2.2 Potentiometric Measurements

This experiment seeks to observe the difference of the potentiometric readings in the event the the cell current is varied. This is done by varying the concentration of H_2O_2 in various pH buffers, and

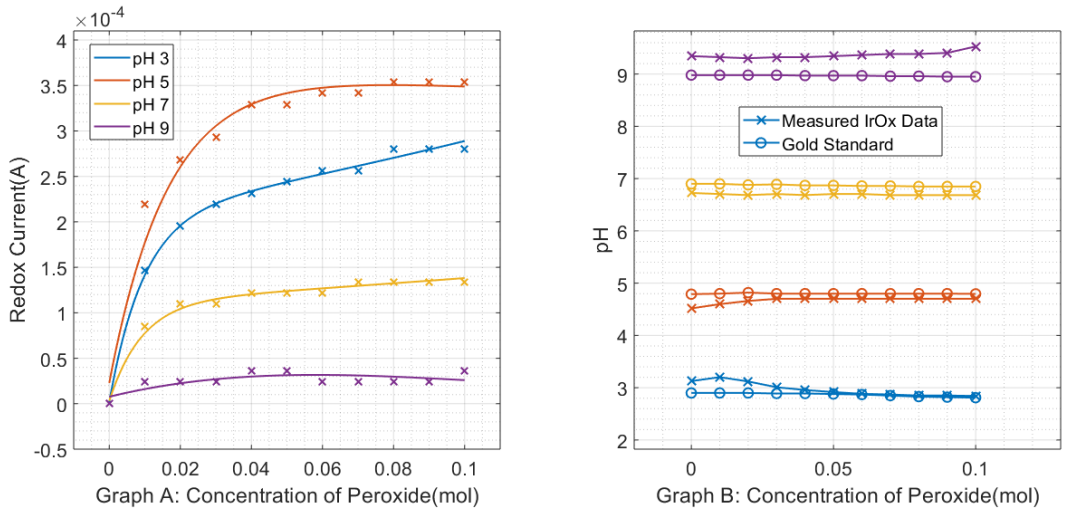


Figure 3.4: Graph A: Combined amperometric readings for cell current measurements across a range of concentrations for various pH buffers with background current removed. Graph B: Combined potentiometric measurements of pH values of buffers for varying concentration of hydrogen peroxide compared against a measured control.

comparing them with pH measurements utilising a gold standard. The protocol is as follows:

1. 20ml of pH 3, 5, 7 and 9 solution prepared on a magnetic stirrer (rpm 200)
2. Increasing concentrations of 0.01M of H_2O_2 is added to the solution.
3. Sentron pH meter is used to serve as the gold standard pH value with readings taken for each concentration value.
4. Measurements of potentiometry taken for the combined configuration (Fig. 3.1C) for V_{pot} and RE for the full range of concentration as shown in Fig. 3.4B.

The results are shown in Fig. 3.4B. The measurements with the gold standard shows that the pH remains constant, and only changes slightly (up to 10%) for higher concentrations of H_2O_2.

The difference between the gold standard and the IrOx electrode observed is shown in Table 3.1 and can be characterised as varying between a negative value for both pH 5 and 7 and a positive value for pH 3 and 9. This value for pH 5, 7 and 9 remain relative constant with variation around $\pm$0.4 pH.

Table 3.1: The mean and standard deviation of the pH difference between measured ISE results and control for various pH values (ISE-Control)

pH	Mean of pH difference	Standard Dev.
3	0.099	0.103
5	-0.129	0.0587
7	-0.175	0.0134
9	0.398	0.0724

3.3 Analysis and Discussion

3.3.1 Comparison of Separate vs Combined

The sensitivity of the separate and combined potentiometric readings are -0.0557V/ pH and -0.0661V/ pH respectively as seen in Fig. 3.2. This indicates that the ISE sensor behaves similarly, and also demonstrates the feasibility of the use of potentiometric readings with a shared reference electrode. More importantly, the varying cell current (as measured by the amperometric sensor) showcases that even for increasing cell current for higher pH values, the combined potentiometric sensor is still capable of behaving ideally, albeit with an error ratio up to 26% higher. This can be seen at the pH 7 readings, with the combined configuration having a slightly higher error ratio compared to the separate configuration. A cross correlation of 0.9981 particularly indicates the high statistical similarity in their trends.

As the separate and combined amperometric readings differ only through the addition of the ISE electrode, the results in Fig. 3.3 are as expected with both configurations following a similar trend with a slight offset in the current readings. The high cross correlation of 0.9959 between both the combined and separate amperometric readings leads to the conclusion that the amperometric sensors in both configurations have very similar trends.

3.3.2 Potentiometry with Cell Current

A particular challenge faced is to demonstrate the accuracy of the potentiometric readings in the presence of various levels of cell current. This is highly unconventional, and prior work in [8] and [9] has shown the possible effects of this cell current on enhancing potentiometry. In comparison, we are looking at how much this cell current will cause the actual readings to differentiate or deviate from the gold standard.

Fig. 3.4A demonstrates that additional H_2O_2 concentrations increase the cell current. The large increment in cell current at lower pH values (3, 5) compared to the higher pH values (7,9) is likely due to all H^+ ions introduced by the H_2O_2 reacting with the OH^- ions in the pH 9 solution to form water - which is neutral.

Another important observation that can be made is that the largest variations in cell current occurs for the lower H_2O_2 concentrations at pH 5 and 7. This is reflected in Fig. 3.4B, where the offset for the pH 3 and pH 5 potentiometric readings are largest for the first 2 samples. However, as additional H_2O_2 concentrations are added, the combined potentiometric readings follow the gold standard.

Table 3.1 shows that the difference in pH between the control and experiment for pH 9 is the highest, although it remains relatively stable throughout. In comparison, the difference for pH 3 is the lowest, although its variation is the highest among the compared buffers (as seen from its standard deviation of 0.103). The variation in this difference could be attributed to the varying cell current, and serves to relate the theory that the cell current would affect potentiometric readings. However, for values of

cell current in the magnitude of 10^{-4}A, it is clear from the results that the variation is minuscule. This leads to the conclusion that potentiometric readings are capable of accurately reading values in the presence of cell currents, and is demonstrated for cell currents up to 10^{-4}A.

3.4 Chapter Summary

This chapter shows that concurrent measurements of potentiometry and amperometry is possible with a shared reference electrode. It demonstrates clear similarities in their trends, for amperometry and in particular for potentiometry even with a cell current applied. The high correlation values, as well as similar sensitivities of the sensors, showcase that the combined configuration is equivalent to their conventional counterparts.

The efficacy of concurrent sensing is exhibited through the novel design of a test that varies pH and H_2O_2 concentrations concurrently. The presence of cell current is acknowledged, and shown that at levels such as 10^{-4}A, the potentiometric readings are relatively unaffected.

A CMOS IC with the above topology will be tested with 4 on-chip electrodes[10] in Chapter 4. This IC will be used to further analyse the concepts of concurrent sensing and prove its viability in extremely small packages.

References

[1] C. Instruments. *CHI111 Ag/AgCl Reference Electrode w/ porous Teflon Tip*. Apr. 2020. URL: https://www.chinstruments.com/accessories.shtml.

[2] Dropsens. *Dropsens 550 Screen Printed Electrode*. Apr. 2020. URL: http://www.dropsens.com.

[3] M. Wang, S. Yao, and M. Madou. "A long-term stable iridium oxide pH electrode". In: *Sensors and Actuators B: Chemical* 81.2-3 (2002), pp. 313–315.

[4] Sentron. *Sentron Si 400 pH Meter*. Apr. 2020. URL: http://www.sentron.nl.

[5] C. Instruments. *CH Instruments Model 700E Bipotentiostat*. Apr. 2020. URL: https://www.chinstruments.com/chi700.shtml.

[6] T. Instruments. *TI LMC 6042 Potentiostat*. Apr. 2020. URL: https://www.ti.com/product/LMC6042.

[7] D. Harvey et al. "Analytical Chemistry 2.0". In: (2018).

[8] É. Pergel et al. "Picomolar detection limits with current-polarized Pb2+ ion-selective membranes". In: *Analytical chemistry* 73.17 (2001), pp. 4249–4253.

[9] E. Lindner, R. E. Gyurcsányi, and R. P. Buck. "Tailored transport through ion-selective membranes for improved detection limits and selectivity coefficients". In: *Electroanalysis: An International Journal Devoted to Fundamental and Practical Aspects of Electroanalysis* 11.10-11 (1999), pp. 695–702.

[10] D. Ma, S. S. Ghoreishizadeh, and P. Georgiou. "DAPPER: A Low Power, Dual Amperometric and Potentiometric Single-Channel Front End". In: *IEEE International Symposium on Circuits and Systems 2020* ().

Chapter 4

DAPPER: A Low Power, Dual Amperometric and Potentiometric Single-Channel Front End

The previous chapter demonstrated the possibility of utilising a four-electrode structure to effectively apply both amperometry and potentiometry concurrently. To implement this, a front end circuit is developed for measurement as well as for the transmission of these measurements through a integrated wireless system. This chapter presents a **D**ual **A**mperometric and **P**otentiometric **P**ower **E**fficient instrumentation (**DAPPE**R). This system is an analog front end circuit that performs concurrent potentiometry and amperometry sensing, producing a single output by combining the two readings. The results in this work was published in IEEE ISCAS 2020[1].

In addition, further simulations are performed to obtain a analytical understanding of the errors arising from mixing two frequencies through a single channel. The simulations for the error analysis of the data transmission was done by Giuliana Emmolo for her Master's project in 2021. The results were published in IEEE MeMeA 2021[2]. The following chapter will describe the wireless power implementation of the system.

4.1 System Design

DAPPER is illustrated in Fig. 4.1. The envisaged electrochemical cell consists of four electrodes: working electrode (WE) for amperometric sensing, an ion-selective electrode (ISE) for potentiometric measurement, a shared reference electrode (RE) and a counter electrode (CE). This electrode configu-

[1] **D. Ma**, S. S. Ghoreishizadeh and P. Georgiou, "DAPPER: A Low Power, Dual Amperometric and Potentiometric Single-Channel Front End," 2020 IEEE International Symposium on Circuits and Systems (ISCAS), 2020, pp. 1-5, doi: 10.1109/ISCAS45731.2020.9181213.

[2] G. Emmolo, **D. Ma**, D. Demarchi and P. Georgiou, "Multiple Input, Single Output Frequency Mixing Communication Technique for Low Power Data Transmission," 2021 IEEE International Symposium on Medical Measurements and Applications (MeMeA), 2021, pp. 1-6, doi: 10.1109/MeMeA52024.2021.9478708.

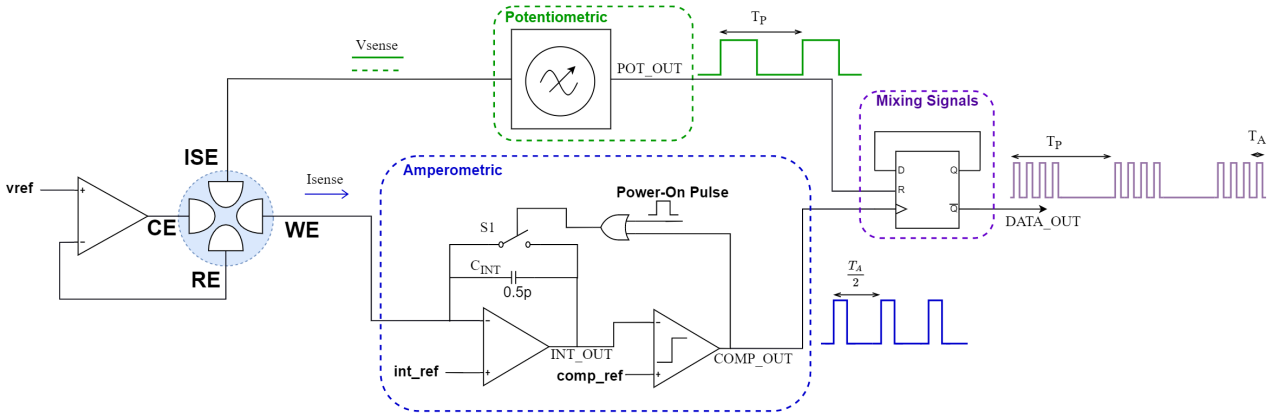


Figure 4.1: The block diagram showcasing the circuit in DAPPER, the proposed dual amperometric and potentiometric front end

ration has been demonstrated to work well in concurrent sensing mode as shown in the previous chapter.

An amplifier in negative feedback drives the counter electrode (CE) and shared reference electrode (RE). Both the amperometric and potentiometric circuits transduce their inputs into output frequencies. The outputs of the two circuits are then mixed through the use of a D flip-flop to be transmitted outside on a single channel. The reference voltages **v_ref**, **int_ref** and **comp_ref** are provided externally, along with a power-on pulse to start the circuit. The circuit has four main blocks which will be detailed in this section.

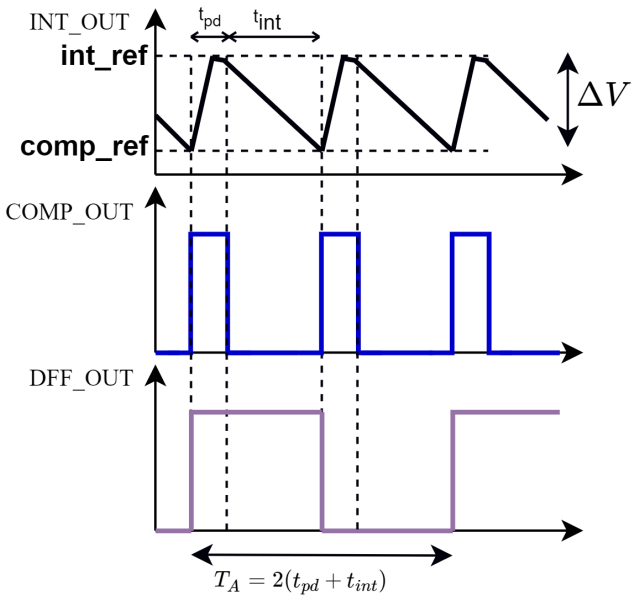


Figure 4.2: Timing Diagram of Amperometric Circuit

4.1.1 Amperometric Circuit

The amperometric circuit consists of a switch-capacitor integrator and a comparator in a feedback loop. The circuit generates a square waveform with a frequency proportional to the input current. The integrator accumulates the input current on a capacitor when S1 is open. The reset clock of the capacitor is provided by the comparator to ensure the output voltage of the integrator is within a specific voltage range.

The amperometric circuit has two phases: *integration* and *reset*. The power-on-reset pulse sets the circuit in *integration* mode at system start-up. During the *reset* phase, $\mathrm{COMP\_OUT}$ is high and S1 is closed. The integrator is configured as a voltage buffer, and $\mathrm{INT\_OUT}$ rises to the input reference **int_ref**. During the *integration* phase where $\mathrm{COMP\_OUT}$ is low, S1 is open, the capacitor discharges and $\mathrm{INT\_OUT}$ falls to the comparator reference **comp_ref**. Once it reaches **comp_ref**, $\mathrm{COMP\_OUT}$ goes high, and closes S1 after a propagation delay from the output of the comparator to S1. This then starts the *reset* phase all over. The waveforms that occur throughout the circuit are presented in Fig. 5.10.

The comparator output is fed into the clock input of the D flip-flop. This is utilised as a divide-by-2 counter to obtain a 50% duty cycle, making it easier to demodulate at the backend.

Each period of the output pulse width consists of t_{pd}, the propagation delay from the time the comparator input crosses the threshold voltage to when S1 is closed, and t_{int}, the integration time. The output period of the DFF can be calculated as:

$$T_{DFF\_OUT} = 2(t_{pd} + t_{int}) \tag{4.1}$$

From the equation for the charge in a switched-capacitor integrator, we obtain the integration time in Eq. 4.2, where C_{INT} is the feedback capacitor value, ΔV is the difference in voltage between **int_ref** and **comp_ref**, and I_{in} is the input current:

$$t_{int} = \frac{C_{INT}\Delta V}{I_{in}} \tag{4.2}$$

Putting the equations together, we obtain an expression for the output frequency at the D flip-flop, $f_{out,amp}$, as a function of input current in Eq. 4.3.

$$f_{out,amp} = \frac{I_{in}}{2(t_{pd}I_{in} + C_{INT}\Delta V)} \tag{4.3}$$

This shows the output frequency varies in a non-linear fashion due to the non-zero propagation delay t_{pd} of the circuit. However, this could be estimated to a linear equation when t_{pd} is small compared with t_{int}.

4.1.2 Potentiometric Circuit

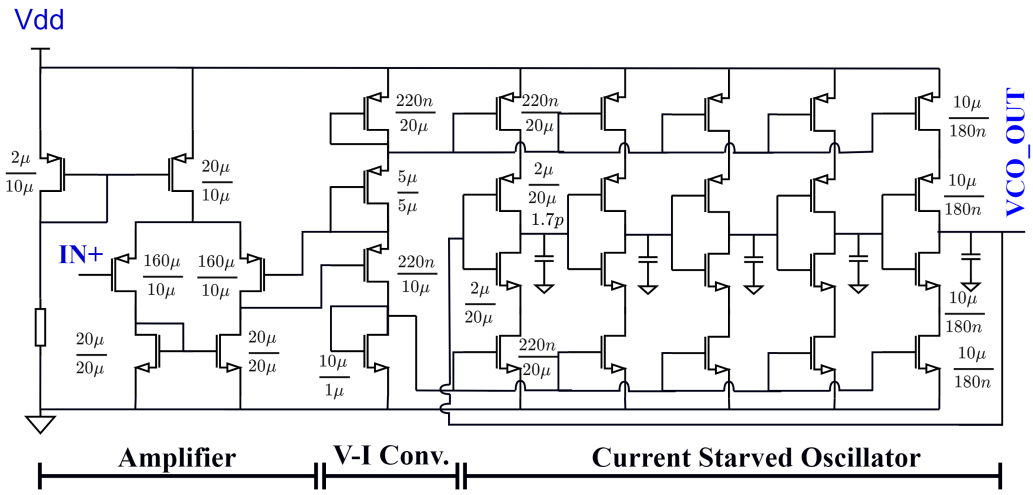


Figure 4.3: Potentiometric Frontend Consisting of Current Starved Oscillator and Differential Pair

The potentiometric circuit serves to convert the input voltage read between RE and ISE into a frequency. Fig. 4.3 shows the potentiometric circuit where IN+ connects to ISE. This voltage input is passed through a differential input amplifier, before a central buffer is used to convert this voltage into a current. PMOS and NMOS current mirrors are used to bias the current sink and source transistors for the current starved ring oscillator. Extra capacitors are added after each stage to further reduce the frequency of the oscillators.

4.1.3 Mixing the signals

The output signals of the potentiometry and amperometry circuits are mixed using a D flip-flop with an asynchronous active-low reset. Fig. 4.4 demonstrates the mixing of the different waveforms. The figure describes a possible situation that arises when the potentiometric output is high during a low edge for the amperometric output. t_a is the time when the potentiometric signal goes high, while t_e is the time when the mixed signal goes high. t_b captures the point where the potentiometric output goes low.

By detecting the edges in the mixed signal and calculating the edge-to-edge time difference, it is possible to reconstruct the amperometric data for T_A. To ensure at least two rising edges of T_A are detected on the mixed signal, T_P has to be chosen to be at least 4 times higher than T_A. For the potentiometric signal which occurs at a lower frequency, there exists an error arising from the phase difference. The received period of T_P is:

$$\frac{T_{P,received}}{2} = t_b - t_e = \frac{T_P}{2} - e \tag{4.4}$$

where $t_e - t_a < T_A$. This becomes $\frac{t_e - t_a}{T_P} < \frac{T_A}{T_P}$, which allows us to deduce the percentage error. Thus, we have the requirement that the amperometric frequency is at least an order of magnitude ($\times 10$)

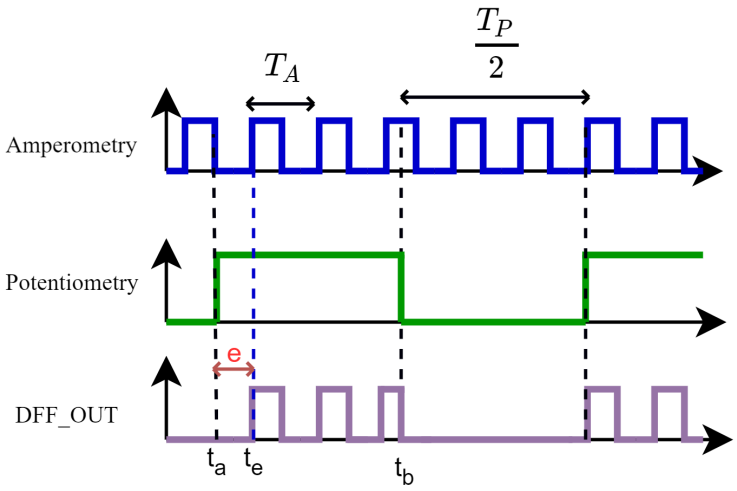


Figure 4.4: Mixing Timing Diagram with the amperometric output, potentiometric output, and the mixed signals obtained, along with the error $t_e - t_a$

larger than the potentiometric frequency, which gives a maximum error for $T_{P,received}$ to be 10%.

In addition, the input clock voltage threshold of the D flip-flop and the comparator are designed to only trigger for currents above the 250 pA level. This is done by carefully designing the dimensions of the input transistors of the D flip-flop. Hence, lower current values will not be detected.

4.1.4 Amplifier

The topology of the amplifier in Fig. 4.3 is used for both amperometric circuits and potentiometric circuits, and is a single stage differential input amplifier. PMOS transistors with long lengths are used as input transistors minimise the noise. The open-loop gain of the amplifier is 54 dB with a phase margin of 77° (with no load connected). The maximum power consumption, power supply rejection ratio, common-mode rejection ratio and the -3 dB bandwidth from simulations for the amplifier are 6μW, 52 dB, 63 dB and 10 kHz respectively. The integrated input-referred voltage noise over the -3dB bandwidth of the amplifier 1.7μV.

4.2 Simulation Results

The circuit is designed in a standard 180nm CMOS technology and simulated with cadence. The layout is presented in Fig. 4.6 with the circuits occupies a total area of 0.098mm^2. Fig. 4.5 displays the output frequency ranges for both the potentiometric and the amperometric circuits. For the amperometric circuit, the frequency output is shown for DC current inputs from 250pA to 5.6μA. This circuit draws 29μW at the maximum frequency. The output frequency of the D flip-flop when potentiometry is deactivated begins at 214Hz@250pA before increasing to 551kHz@5.6μA.

The frequency output shows a linear trend from 250pA to 0.1uA with a slope of 1260Hz/nA. From 0.1uA to 5.6μA, this gradient reduces to 68Hz/nA. This corresponds with the reduced gain of the am-

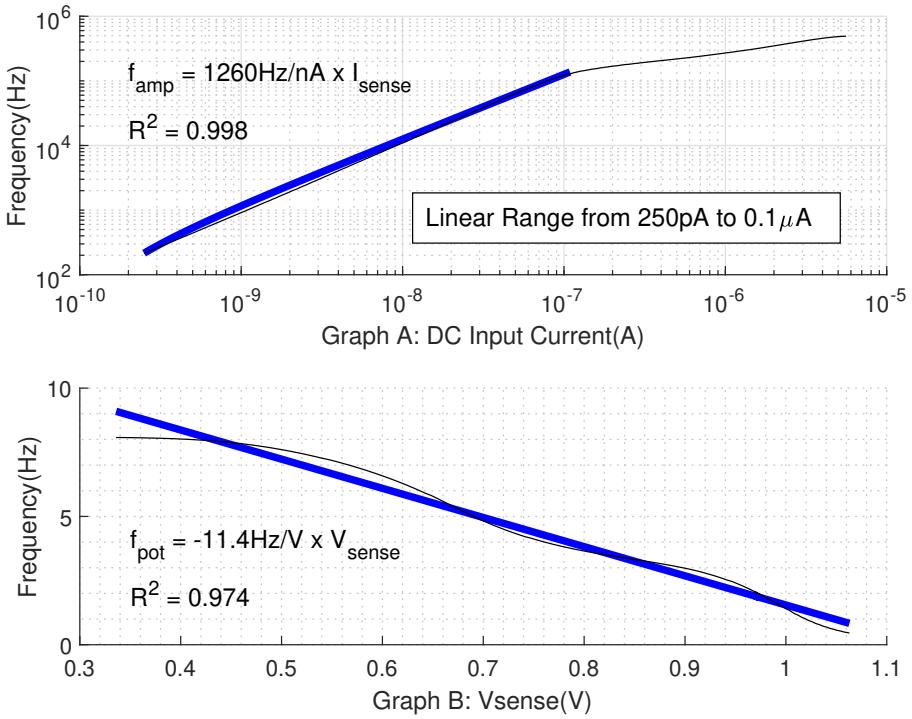


Figure 4.5: A: Output frequency of amperometric circuit at D flip-flop when potentiometry is deactivated for DC input current. B: Output frequency of potentiometric circuit for DC input voltage.

plifier after the bandwidth of 10kHz of the amplifier. The propagation delay t_{pd} from the comparator output to S1 increases from 100 ns at I_{in}= 250pA to 500 ns at I_{in}=0.1μA, which explains the difference in the gradient as per Eq. 4.3. This delay increases as for higher currents, C_{INT} takes a longer time to discharge.

The simulated input-output characteristics of the potentiometric circuit is shown in Fig. 4.5, showing sufficiently linear behavior between 0.4V to 1V, which is adequate for values measured using a metal oxide based pH electrode[1]. The curve displays a linear relation, with a slope of -11.4Hz/V input. The power consumption at the maximum frequency of the circuit is 3μW.

Fig. 4.7 displays the output simulation for the D flip-flop for Isense = 300pA and Vsense = 0.7V. The reset switch is effective in modulating the output of the D flip-flop to correspond to the potentiometric output frequency, while the amperometric output frequency can still be obtained from the individual pulses.

4.3 Electrical Measurements

The fabricated Dapper is shown in Fig. 4.8. The circuit area is shown as a 150μm by 60μm area along with surface located bondpads for potential electrode plating.

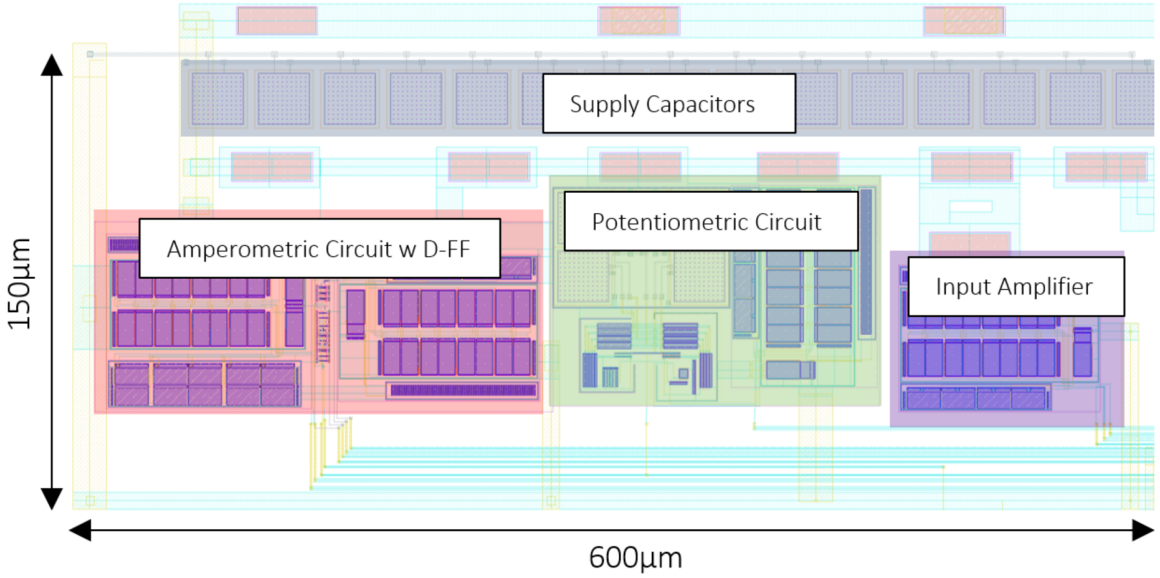


Figure 4.6: Layout of DAPPER

4.3.1 Experimental Setup

Two printed circuit boards (PCBs) are developed in Altium Designer for the testing platform: the daughterboard where the chip is bonded to and a Motherboard that hosts the testbench as seen in Fig. 4.9. This setup allowed for a quick swap for the daughterboard, facilitating quick comparisons amongst working ICs. The daughterboard consists of a grounding plane for the IC along with pads for wirebonding, while the motherboard consisted of peripherals for the IC such as a coil for wireless powering, electrode connection points, the card connector to the daughterboard, generated reference voltages through the use of potentiometers and power supplies from a raspberry pi or from an external supply. A pulse generator is also prepared in the event that the on-chip power-on-reset circuit was not functioning.

First, the ICs were electrically bonded to the ground plane on the Daughterboard through the use of EPO-TEK H20E electrically conductive epoxy. The Daughterboard is then cured in an oven at 125°C for an hour. The Daughterboard is then wirebonded(using the F&S Bondtec manual bonder) to the IC with a 25μm aluminium wire. After bonding, a quick electrical test is run to ensure all wires are functioning correctly. Once verified, EPO-TEK T7139 glob top epoxy is applied to the top of the wirebonds to protect the connections. The Keithley 2602B is utilised to provide current and voltage sources for the IC, in addition to external power supplies for powering the IC and occasionally supplying the reference voltages.

4.3.2 Focused-Ion Beam (FIB) Milling of Tahu

After initial tests, it was found that the bondpad connection for the COMP_OUT pin on DAPPER as shown in Fig. 4.1 was directly connected to a ground pad by mistake. This effectively meant that the output of the D flip-flop, along with the amperometry output were unable to output any

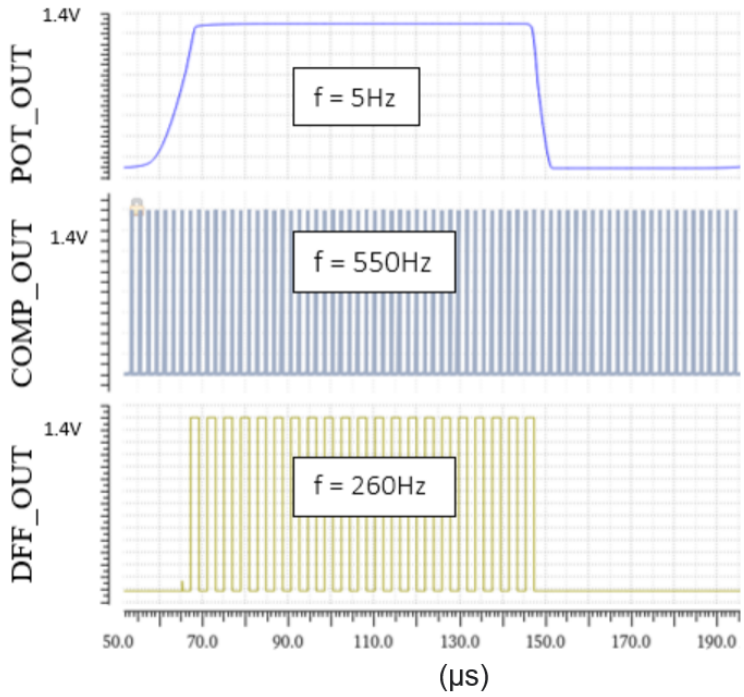


Figure 4.7: Simulation of the output voltages for an Isense = 300pA and Vsense = 0.7V. This corresponds to 5Hz and 260Hz on the D flip-flop output.

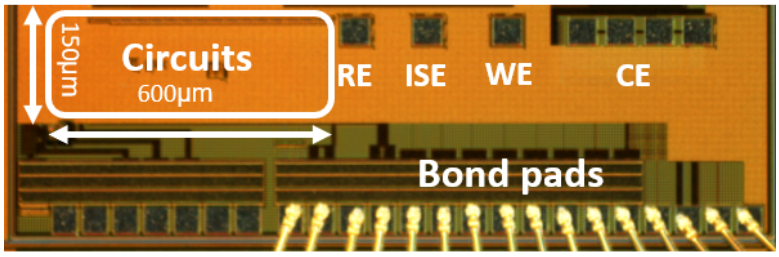


Figure 4.8: Fabricated DAPPER circuit highlighting the circuit area and surface bondpads. This was fabricated on TSMC180 technology.

coherent signal. This was resolved through the focused-ion beam milling of the track connected to the aforementioned ground pad. This was achieved with a Tescan Lyra3 workstation. Fig. 4.10 shows the layout of the circuit as well as the milling point (shown in red) for the track. The bond pads marked in blue were used as reference points for accurate milling.

Fig. 4.11 shows the results after the milling is completed. The chip functions as expected after the fibbing, although signals could not be extracted from $\mathrm{COMP\_OUT}$ due to the lost testpad.

4.3.3 Measurements

The power consumption results of the whole system is measured to be 28μW at the maximum linear output frequency of both the amperometric (122.5kHz) and potentiometric circuit (6.8Hz). This is done through measuring the maximum current drawn at the supply voltage. The setup is shown in Fig. 4.12.

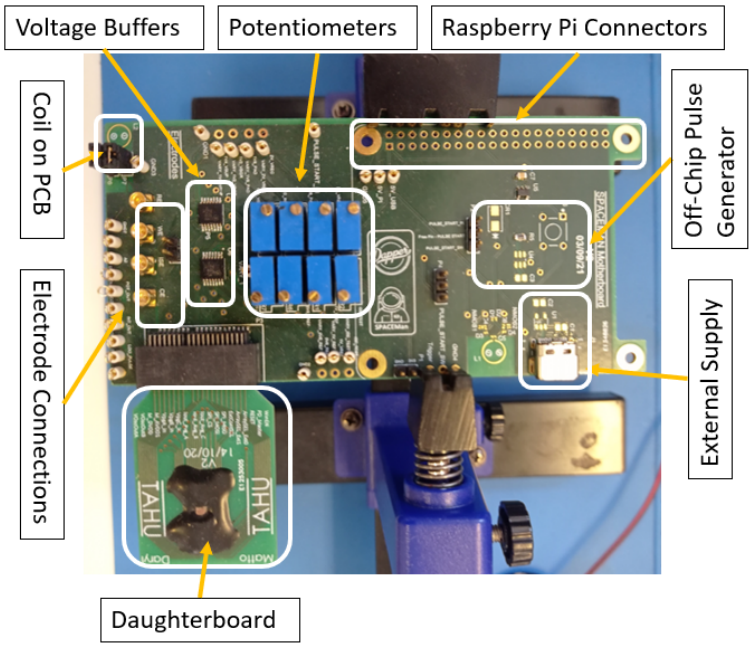


Figure 4.9: Experimental Setup of the Daughterboard and Motherboard, with the wirebonded IC along with the glob topping.

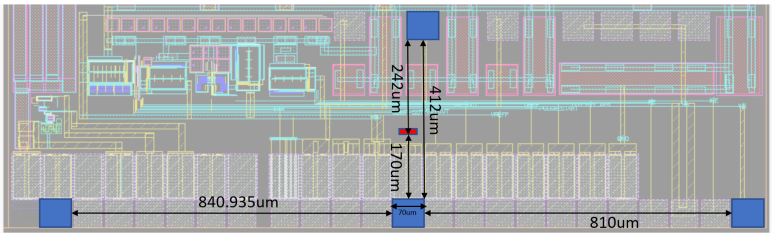


Figure 4.10: Layout of potential milling point - the track between the comparator output and the ground buffer

A voltage source of 0.3V-1V in 50mV steps is applied using the Keithley into the ISE input and the output frequency oscillation was measured using a Tektronix DPO4034 oscilloscope to observe the frequency. Likewise, a current source of 200pA - 0.8μA was applied into the WE input and the output frequency observed. The left image in Fig. 4.13 shows the potentiometric signal and the system output observed for an input of 1V and 0.1μA, while the right image in Fig. 4.13 zooms into the system output along with the integrator output.

A plot of the output frequency vs the input voltage is obtained and shown in Fig. 4.14. The amperometric readings display a linear range from 200pA to 0.1μA. Below this input, no output is observed. The measured readings correlate closely with the simulated readings described in Fig. 4.5.

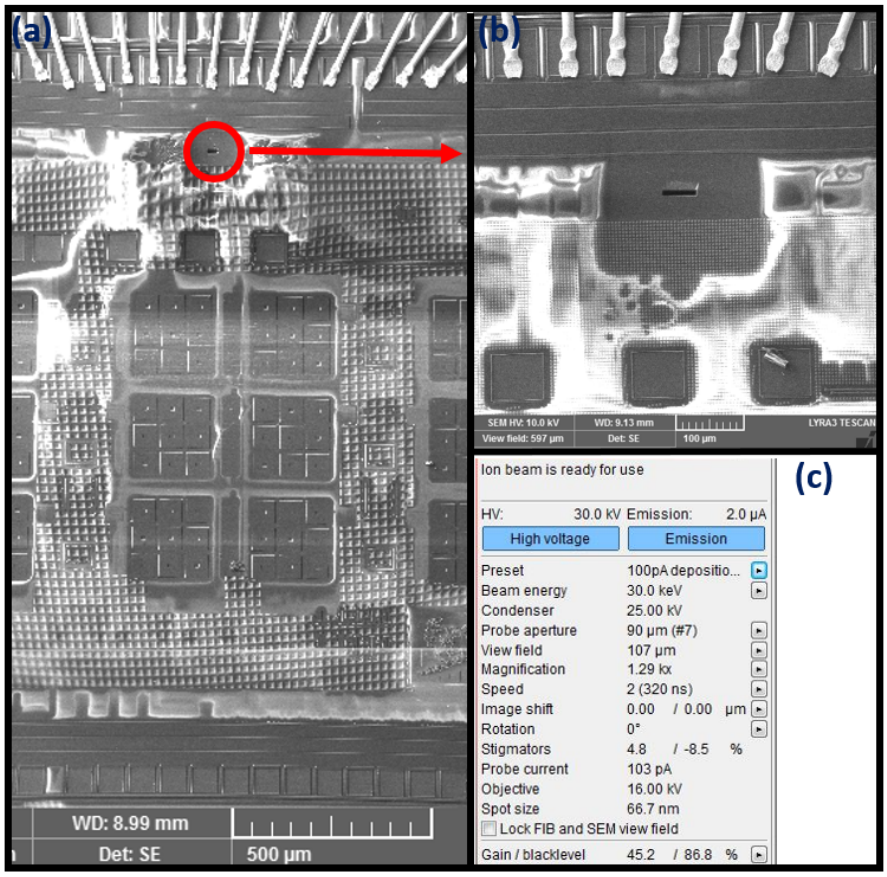


Figure 4.11: Images taken from the Scanning Electron Microscope (SEM) displaying the milling point on Tahu. (A) shows the entire chip, while (B) shows a zoomed in image up to the 20μm cut in the silicon. (C) shows the settings for the milling involved.

4.4 Electrochemical Measurements

4.4.1 Test Method

The circuit was validated utilising the setup in Fig. 4.15 in Chapter 3 with a key difference. To reduce the amount of current drawn from the electrodes from the previously measured 0.1-0.6mA range down to the nano-ampere range suitable for this circuit, the Dropsense 550 planar electrodes previously used for the CE and WE electrodes are swapped out for simple platinum wires (Sigma-Aldrich, 2mm Diameter). As the electrode surface affects the amount of current drawn, utilising a wire of minute diameters allowed for the current to reduce to values that were measurable and within the range of the system. In addition, the peroxide concentration is reduced by a magnitude of 10 from 10mMol - 100mMol to 1mMol - 10mMol for a better observable range.

4.4.2 Individual Readings

For the pH input, 3 readings were taken and the potentiometric frequency output observed on an oscilloscope. The results are shown in the left image of Fig. 4.16. The plot of the output frequency

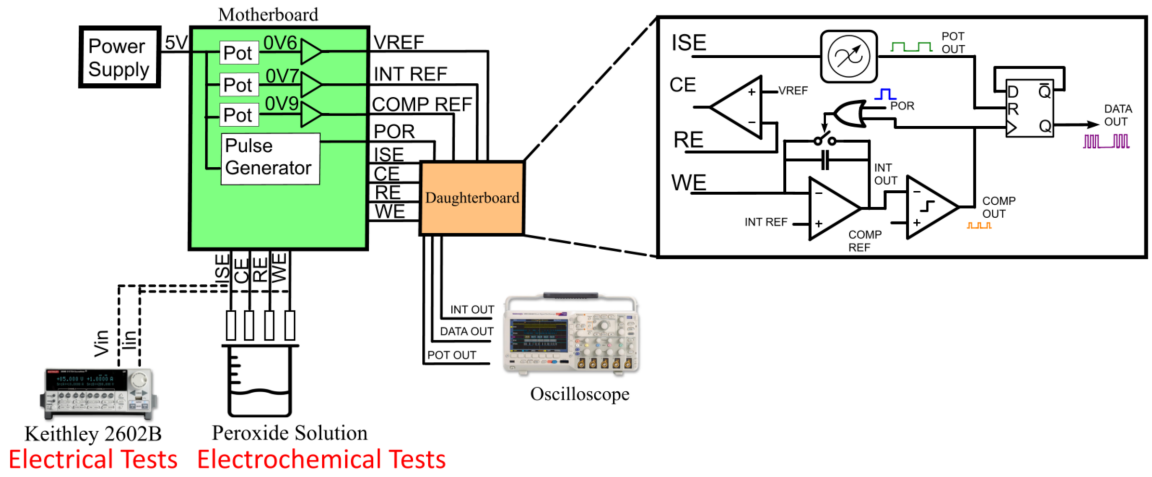


Figure 4.12: Experiment setup for the measurements taken.

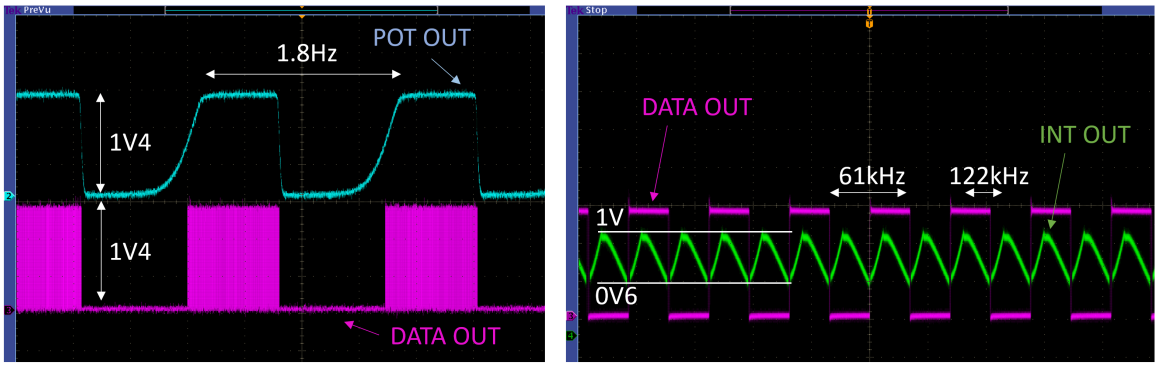


Figure 4.13: Left: Scope trace of the potentiometric output (POT OUT) and the overall mixed signal output (DATA OUT) from a voltage input of 1V and a current input of 0.1μA. Right: Zoomed in trace of the overall system output (DATA OUT) with the integrated output (INT OUT). This shows that the frequency is halved after passing through the D flip-flop, which is expected.

shows an increasing linear trend for an increase in the pH value. To provide an indication of how the frequency is used to monitor the measured voltage and currents at the electrode, the trendline equation from Fig. 4.14 is used.

The characteristic equation of the potentiometric frequency is given by the following equation:

$$f_{pot} = -6.6Hz/V * V_{input} + 9.06 \tag{4.5}$$

where f_{pot} is in the output frequency for the potentiometry, and V_{input} is the input voltage into the ISE. Rearranging the equation allows us to obtain the derived input voltage from the output frequency as shown:

$$V_{input} = \frac{(f_{pot} - 9.06)}{6.6Hz/V} \tag{4.6}$$

Similarly, the characteristic equation of the amperometric frequency is given by the following equation:

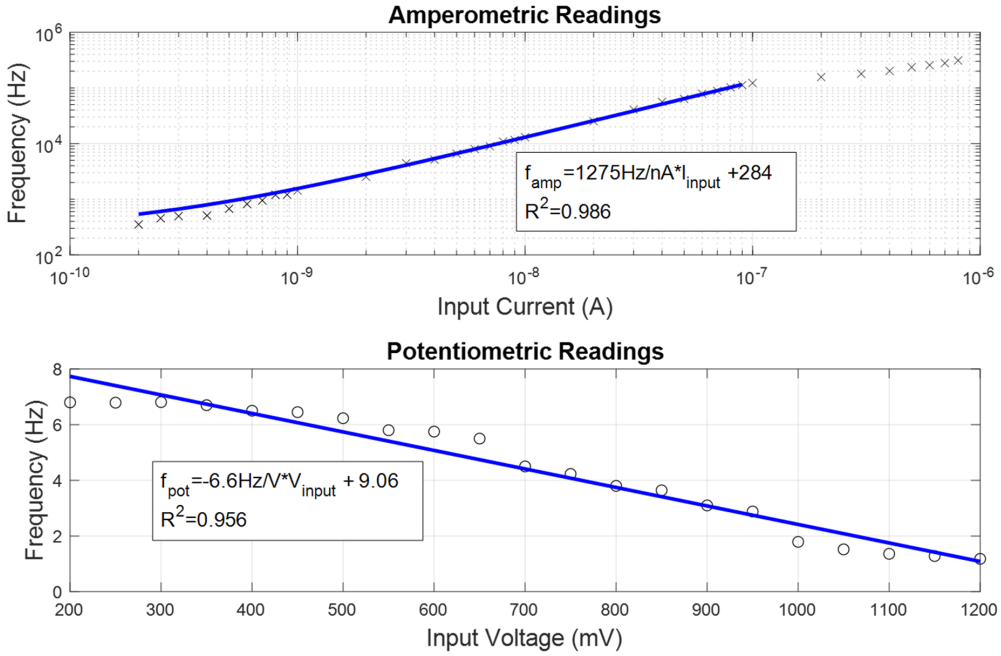


Figure 4.14: Plot of the measured amperometric readings above and potentiometric readings below. The linear region for the amperometric readings are from 200pA to 0.1μA.

$$f_{amp} = 1275Hz/nA * I_{input} + 284 \tag{4.7}$$

where f_{amp} is in the output frequency for amperometry, and I_{input} is the input current into the WE.

$$I_{input} = \frac{(f_{amp} - 284)}{1275Hz/nA} \tag{4.8}$$

Rearranging the equation allows us to obtain the derived input current from the output amperometric frequency.

The derived input voltage obtained from the trendline equation in shows the input voltage slowly decreases as the pH increases - which tallies with our expectations. For the peroxide measurements shown in the right image of Fig. 4.16, a similar trend is noted for increasing concentrations of peroxide. The derived input current also follows on with a clear trend of increasing current for increasing concentrations of peroxide.

4.4.3 Concurrent Readings

To show the possibility of measuring both the sensors concurrently, increasing concentrations of peroxide is added to a fixed pH 3 buffer. An average of 3 readings is taken per concentration of peroxide with the minimum and maximum values shown in the error bars. The measured frequencies is shown in the left image of Fig. 4.17. The frequency for the potentiometric output remains constant throughout between 1.8-1.9Hz, while a clear increment in the amperometric frequency is shown for increasing peroxide concentrations.

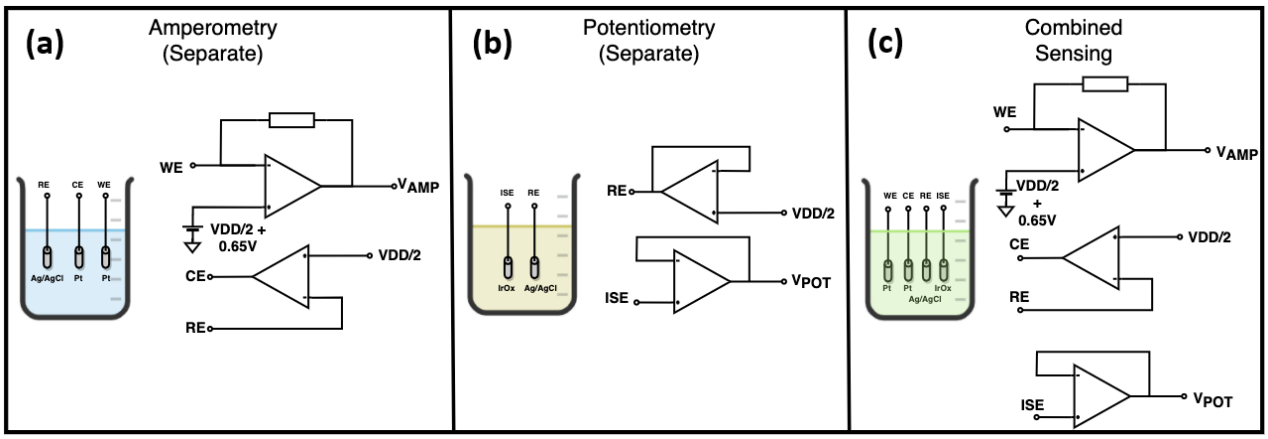


Figure 4.15: Experiment Circuitry employed for this experiment with the separate potentiometric and amperometric modes along with the combined setup. The chosen electrodes along with their materials are also displayed.

The values of the current and voltage is obtained from the values of the frequency in the left image of Fig. 4.17 for a quantitative view of the change in current and voltages. The right image of Fig. 4.17 shows the derived current and voltage values. There is an increase in the current values for increasing concentration levels of the peroxide while the pH levels remain constant. This tallies with the experiments done previously in Chapter 3.

4.5 Analysis

The results showcases the possibility of using concurrent sensing with a single front-end output albeit with some limitations. In this experiment, the sensors utilised are still large as compared to the on-chip sensors. It is expected that the actual magnitude of the current and voltage should decrease.

The right image of Fig. 4.17 showcases this limitation. Although the derived current changes for an increment in peroxide concentration, this increment is not large enough to trigger a large change in the input voltage - and hence the potentiometric frequency stays the same throughout at 1.5Hz. This is likely due to the small magnitude of the current not affecting the ion-sensitive surface as much as a higher current would do. At smaller electrode surface areas which will be the case for on-chip electrodes, surface area of the electrode may have a larger effect. It is important to quantify this in the future to understand the effect of on-chip electrodes.

The potentiometric readings differ from the simulated readings. The measured gradient of the frequency output vs input voltage is -6.6Hz/V, which was simulated to be -11.4Hz/V. This large difference could be due to process variations involving the structure of the current starved oscillator shown in Fig.4.3. In this structure, the size of the capacitors along with the differential input pairs play a huge role in varying the frequency.

In addition, jitter was also noted for the output frequency of the amperometric circuit after a change in the concentration of peroxide. This could be due to the current fluctuating around the expected

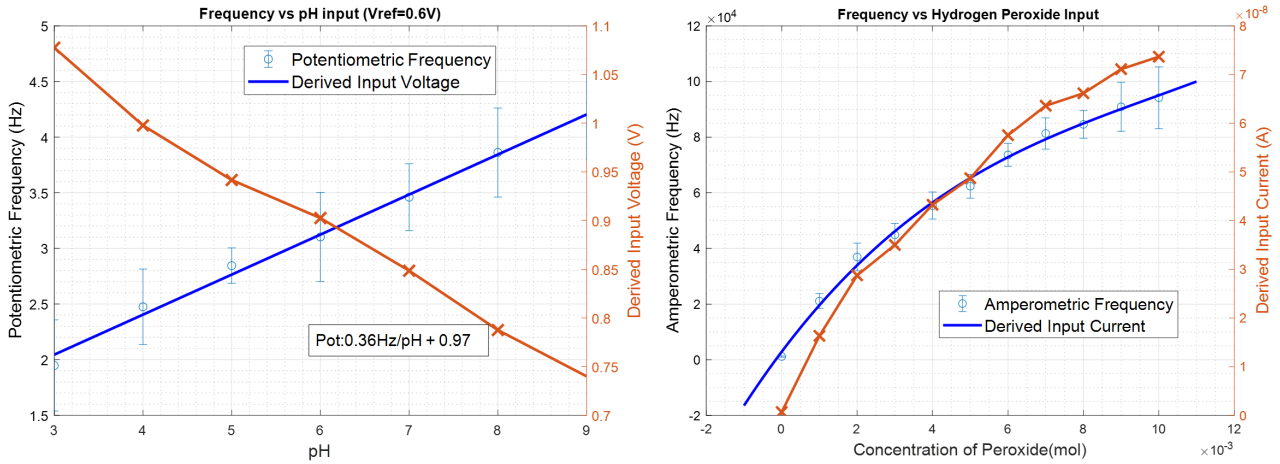


Figure 4.16: Left: Measured potentiometric output for a pH input of 3 to 9 with IrOx electrodes on the left axis. A line of best fit is used to monitor the trend. The derived input voltage on the right axis is obtained from each sampled point itself to show the direct relationship. Right: Measured amperometric readings for increasing concentrations of peroxide from 1mMol to 10mMol on the left axis. A line of best fit is used to show the trend. Similarly, the derived input current on the right axis is obtained from each sample point directly.

range, and is also dependent on the stirrer consistency. As the amperometric circuit is designed for smaller current values, it is important to design the sensitivity of future circuits with a target range in mind to reduce this jitter. The final value of the frequency was each taken after a stable value was reached.

4.6 Data Transmission Error Analysis

As mentioned earlier, mixing both the frequencies results in an error due to phase shift. This section investigates the errors arising from this mixed signal and looks to obtain the optimum frequency ratio for a desired minimum error and power consumption.

4.6.1 D Flip-flop mixer

The idea behind the use of D flip-flop for the purpose of digital mixing has been proposed several times in the literature. Dong et al. proposed the topology for the accurate measurement of the difference between two input frequencies. It also highlighted the use case of such systems for field instruments to measure minute frequency increments of high frequency signals [2]. To our knowledge, the use of a D flip-flop for the mixing of two varying frequencies as a means of transmission across a single channel for wireless transmission has not been described in literature. This method has a number of advantages in particular for the application described in Chapter 2. Firstly, a continuous output stream of frequency from the system ensures that variations in the sensed bio-signals can be readily monitored. This is opposed to a time-division multiplexed solution seen in other single-channel designs where each sensor transmits its data for a fixed amount of time and is switched periodically

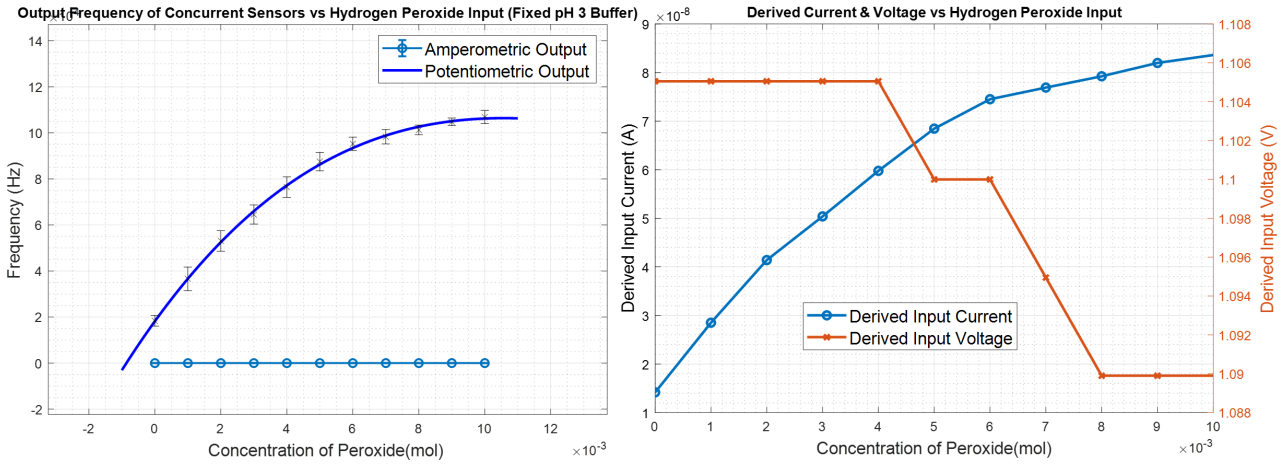


Figure 4.17: Left: Measured output frequencies of both the amperometric and potentiometric outputs for a fixed pH 3. Right: Derived input current and the derived input voltage for increasing concentrations of peroxide from 1mMol to 10mMol. This figure shows that the current increases slightly for increments of peroxide, although the derived input voltage only decreases slightly.

amongst the sensors. Secondly, such a system utilises minimal circuit implementation as compared to a time-division method, which requires system clocks as well as phase-locked loops to achieve timing accuracy. In this scenario, the frequency would be transmitted constantly throughout, and the requirements are simply frequency variant front-ends along with the mixer.

However, there are also drawbacks related to utilising this method which is alluded to in Chapter 4. First, there is an error e associated with the phase difference as described in Equation 4.4. This error arises from two sources: the frequency ratio of the input signals as well as the relative phase shift. Second, there is an associated trade-off in having a higher input frequency ratio - with higher frequencies the power consumption of the system would inadvertently increase.

Hence, this section would aim to do the following: characterising this error value resulting from Dapper with respect to varying input frequency ratios, and obtaining a value of the power consumption resulting from varying input frequency ratios. These two outputs would be overlaid to determine an optimum trade-off value between the error and power consumption.

4.6.1.1 Error resulting from varying input frequency ratios

A base case scenario with a frequency ratio of 7 and 8 is used to demonstrate the sources arising from these errors. Fig. 4.19 describes the various possible scenarios that may occur during the mixing of two frequencies. Fig. A and B showcase the situations when no phase shift occurs, while Fig. C and D showcase the situation when there is a phase shift of 50%. The relative error signal is calculated through the following:

$$T1_{error} = \frac{T1 - T1_{mixed}}{T1} \times 100 \tag{4.9}$$

These examples showcase the two key sources of error: First, the error arising due to the frequency

ratio of the input signals, and second, the error arising due to the phase shift. The error only occurs for the lower frequency signal as the frequency is derived from the start and end edges of the mixed cycle - which is could be lost due to the aforementioned reasons. On the other hand, the higher frequency signal could be easily replicated as multiple periods (at least 2 in this scenario) is available, and hence no error is seen.

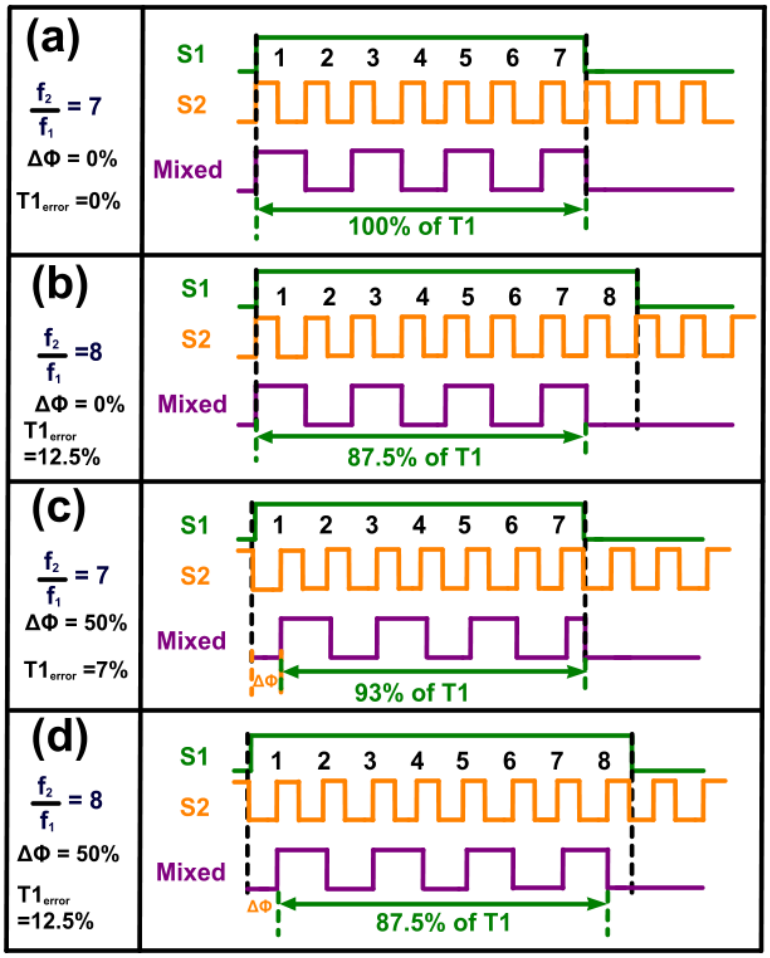


Figure 4.18: Digital mixing errors arising from either the frequency ratio or the phase.

4.6.2 Experimental Set-Up

A functional test simulation in verilog high description language (VHDL) is used to obtain the various error values arising from different frequency ratios. The simulation assumes that both inputs are ideal digital signals, and ensures ignores any errors resulting from analog implementation such as slew rate.

The test system works by calculating the edge-to-edge time difference of the rising edge and falling edge. To do so, a synchroniser is used to ensure the input signal in timed together with the system clock. The system clock has the requirement to be faster than the incoming input frequency. In addition to this, the edge detector generates a rising edge and falling edge signal pulse whenever either is detected. To detect the fast frequency, a high-pulse counter is used which is enabled by the rising edge counter, which is then disabled by a falling edge signal and synchronously reset. The slow

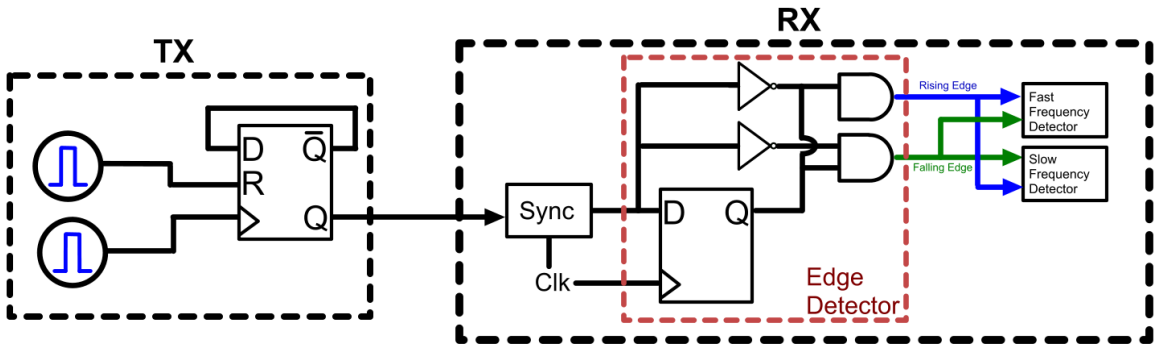


Figure 4.19: VHDL test setup with the transmitter consisting of both signals and the mixer, and the receiver consisting of a synchroniser, edge detector, fast frequency and slow frequency detector

frequency detector operates similarly for a low-pulse counter.

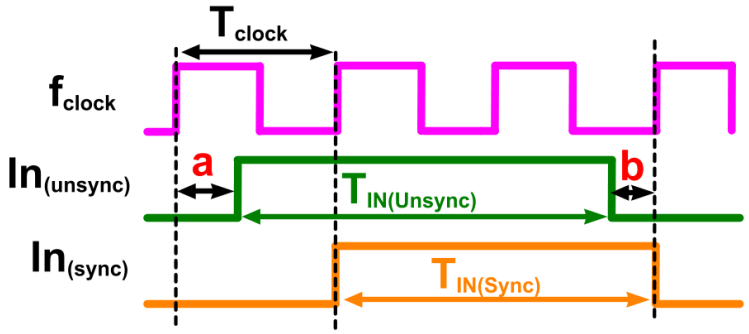


Figure 4.20: Possible error arising from the synchronisation of the input signal with the clock. This error can be alleviated with a higher system clock frequency.

A possibility of an error arising from synchronisation issues is shown in Fig. 4.20. An input signal of $2T_{CK} < T_{in(Unsync)} < 3T_{IN}$ is shown in the figure, where T_{CK} is the system clock, $T_{IN(Unsync)}$ is the unsynchronised input and $T_{IN(Sync)}$ is the synchronised to system clock input. An error arises from the low-to-high edge capture delay (a) as well as the high-to-low edge capture delay (b).

The absolute error can thus be given by the following equation:

$$error \leq |3T_{CK} - a - b - 2T_{CK}| \tag{4.10}$$

from which a percentage value can be obtained:

$$error_{\%} = \frac{T_{CK}}{T_{IN(Unsync)}} \times 100 \tag{4.11}$$

From this equation we ensure that $T_{CK} \ll T_{IN(Unsync)}$ in order to achieve a low error signal. This is done by setting the system clock frequency to a couple of magnitudes higher than the fast input signal.

Fig. 4.21 shows the timing diagram of the entire receiver architecture, and shows how the input signal is synchronised, with the rising and falling edge signals obtained from this signal. A pulse counter is

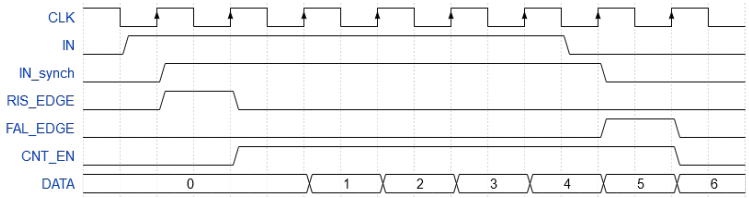


Figure 4.21: Timing Diagram showing the pulse counting process that determines the frequency values of the fast and slow frequency signals.

used to count the number of signals, after which the number of pulses is converted to a frequency value.

4.6.2.1 Results and Analysis

The test system is driven with a 10 samples for at each fixed $\frac{f_2}{f_1}$ ratio for various phase shifts. The error plots for the average, maximum and minimum errors are shown in Fig. 4.22. The average error in Fig. 4.22a describes the general trend of error, which decreases as the frequency ratio of $\frac{f_2}{f_1}$ increases. The plot shows the error evaluated for each specific ratio which is then averaged over all possible phase shifts. This plot also shows that the possible errors arising from phase shift has a larger effect at lower ratios.

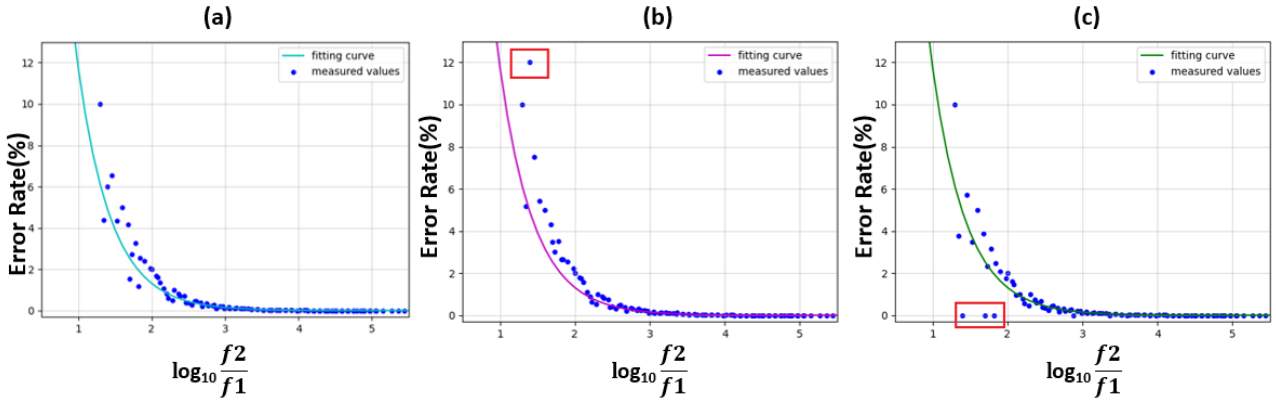


Figure 4.22: Error curves obtained from the experimental setup. (A) shows the average error calculated, (B) the maximum error, and (c) the minimum error. Taken from [3].

The plots have a similarity in that the errors all decrease to near zero after the fourth decade, which correlates to a frequency ratio of at least 10000. On the other hand, the differences between the error samples are due to the varying phase shift errors. Fig. 4.22b shows the maximum error calculated and shows that a possible edge case scenario of an error at 12% is seen despite an input frequency ratio of around 15. This tallies with our previous error estimations as shown in Fig. 4.19 which describes the highest possible error being 12.5%. This shows that our previous calculations prior in Equation 4.4 where we assume a minimum ratio of 10 for a max error of 10% might not be valid. Fig. 4.22c shows that it may be possible for certain combinations of the ratio and the phase shift whereby the error percentage is zero. These plots show that the error arising from the phase shift affects the lower frequency ratios and confirms what we expected, and starts to decrease slowly towards the second and third decade.

The trend line of the average curve is fitted and obtained, from which we achieve the following decaying exponential expression:

$$error_{average} = 154.122 \cdot e^{(-2.281 \cdot log_{10}(\frac{f_1}{f_2}))} + 0 \tag{4.12}$$

4.6.2.2 Power Consumption and Error Trade-Off

From the perspective of a designer, there exists an inherent trade-off between having a higher frequency ratio to decrease the error and a high power consumption of the system. To simulate the energy consumption of the system, we utilise the dynamic power dissipation of a CMOS chip which is frequency dependent. The dynamic power dissipation is given by Equation 4.13:

$$P_{dynamic} = C_{eff} V^2 f \tag{4.13}$$

Where C_{eff} is the effective capacitance of the switch, V is the supply voltage and f is the operation frequency.

In our scenario, the frequency that we will take into account would be the higher frequency values that increase with higher ratios. A linear relation is expected between the total power and the input frequency ratio with a slight offset occurring due to possible leakage current.

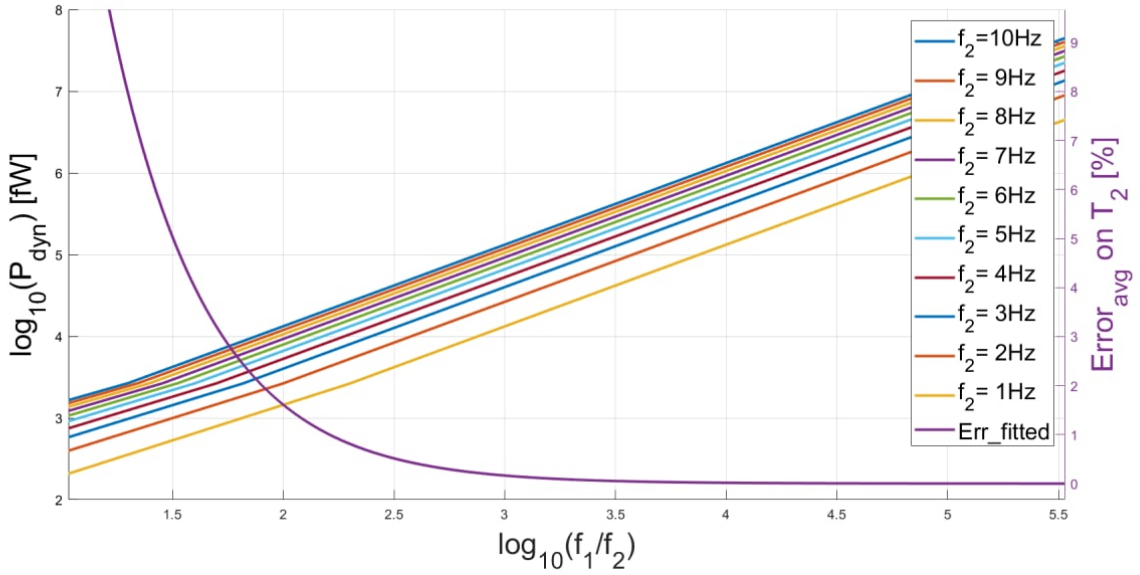


Figure 4.23: Power vs Error trade off plot. Taken from [3].

Real-time logic(RTL) synthesis of a D flip-flop is used to verify the power consumption of the system as a function of the frequency ratio with the results shown in Fig. 4.23. The colored lines observed are increasing frequency ratios. Each of these lines show a linear increase in the power consumption for an increase in the frequency. A shift upwards is seen for each variation in the lower frequency increment as the dynamic power consumption increases. This is due to the lower frequency signal

essentially determining the on-off states of the mixer, and increases the dynamic power as a larger amount of periods are calculated for a fixed timeframe.

The plot of the average error is shown in order to compare the trade off. Equation 4.6.2.2 describes the optimum operating point for a power vs error trade off. This is helpful to the designers who can tolerate low levels of error to allow for a more power-efficient system.

$$1.5 < log_{10}\left(\frac{f_1}{f_2}\right) < 2$$

Table 4.1: Comparison of DAPPER with state-of-the-art

Paper	Technology (nm)	Supply (V)	Power (μW)	Input Referred Noise	Dynamic Range (dB)	Size (mm^2)	Trans. Mech.	Conc. Trans.
[4]	350	3.3	9300	0.47 pA	156 (amp.)	10.08	Amp.	No
[5]	350	3.3	5830	0.044 pA	169 (amp.)	0.3	Amp.	No
[1]	NA	3.3	3600	21.6 mV	NA	140	Pot.	No
[6]	65	0.9	0.97	0.5 mV (pot.) 2.5 nA (amp.)	43 (pot.) 30.1 (amp.)	1.275	Amp.&Pot.	No
[7]	180	1.8	5220	204 fA	140.8 @ 10kHz(amp.)	0.091	Amp.	No
[8]	350	1.4	92	1.8 μV	66 (pot.)	2.1	Pot.	No
[9]	NA	2.8-3.6	990	1.6 μV (pot.) 0.05 nA (amp.)	121(pot.) 155 (amp.)	15.12	Amp.& Pot.	No
This Work	180	1.4	40	1.7 μV (pot.) 44.6 fA (amp.)	62 (pot.) 87 (amp.)	0.098	Amp.&Pot.	Yes

*Trans.Mech. = Transmission Mechanism, Pot. = Potentiometry, Amp. = Amperometry

4.7 Chapter Summary

A comparison with state-of-the-art is presented in Table. 5.2 demonstrating the innovative aspect of this work in providing concurrent dual transduction methodologies. There is a system that utilises both amperometry and potentiometry but does so in different time periods [6]. This work would allow for the real-time calibration of analytes, and the application of a shared reference electrode creates the possibility of a system that uses one less electrode than the conventional topology of amperometry and potentiometry.

An analog front-end chip capable of simultaneous readings of potentiometry and amperometry is presented along with the design of each system block. The system mixes both the outputs through the use of a D flip-flop. The mixed output consists of two frequencies that vary according to the input current and voltage that can be transmitted wirelessly through backscattering. Simulation results are presented to demonstrate the performance and functionality of the chip, and show both a linear DC input current range and a DC voltage input range.

Electrical and electrochemical measurements are also shown to discuss the overall functionality of chip for concurrent sensing. The test setup consists of a motherboard and a daughterboard that is used for providing the reference voltages to the IC. The electrical measurements characterise the amperometric and potentiometric readings. The amperometric readings correlate closely with the

simulated results, while the potentiometric readings differ slightly with a change in gradient from -11.4Hz/V (Simulated) to -6.6Hz/V (Actual). This is postulated to be due to the process variations involving the large capacitors in the current starved oscillator.

The electrochemical measurements show that it is possible to measure both potentiometry and amperometry concurrently, and is based on the experiments previously done in Chapter 3. An increase in the amperometric output for the system is observed for increasing concentrations of peroxide while the potentiometric output remains constant. Similarly, an increase in current values is seen for increasing values of peroxide.

This experiment could be improved upon by designing sensors that trigger a significant change for both the potentiometric and amperometric sensors. At the moment, the ISE sensors are still large compared to on-chip sensors. Having smaller electrode surfaces would likely allow for an observable change in the pH for smaller changes in the concentration. This would be the next step in the development of DAPPER.

The errors arising from mixing two frequencies with a D flip-flop is also formally addressed in this chapter. The error arising from varying input frequency ratios and the error arising from a phase shift is discussed in this chapter. The VHDL simulations show that errors reduce with increasing frequency ratios, and provide an exponential expression relating the error to the frequency ratio. This expression is then utilised to formulate a relationship between the power consumption and the error. This would be helpful for future designers to develop data transmission techniques based on mixing two frequency signals on a single channel.

References

[1] D. Ma, C. Mason, and S. Ghoreishizadeh. “A wireless system for continuous in-mouth pH monitoring”. In: *2017 IEEE Biomedical Circuits and Systems Conference, BioCAS 2017-Proceedings*. IEEE. 2018.

[2] D. Jinfeng et al. “Study on the output characteristics of a D flip-flop differential mixer”. In: *Proceedings 2011 International Conference on Transportation, Mechanical, and Electrical Engineering (TMEE)*. IEEE. 2011, pp. 1552–1555.

[3] G. Emmolo et al. “Multiple Input, Single Output Frequency Mixing Communication Technique for Low Power Data Transmission”. In: *2021 IEEE International Symposium on Medical Measurements and Applications (MeMeA)*. 2021, pp. 1–6.

[4] S. S. Ghoreishizadeh et al. “A differential electrochemical readout ASIC with heterogeneous integration of bio-nano sensors for amperometric sensing”. In: *IEEE transactions on biomedical circuits and systems* 11.5 (2017), pp. 1148–1159.

[5] W. O. Ting and S. S. Ghoreishizadeh. “Autonomous readout ASIC with 169dB input dynamic range for amperometric measurement”. In: *2018 25th IEEE International Conference on Electronics, Circuits and Systems (ICECS)*. IEEE. 2018, pp. 869–872.

[6] H. Jiang et al. “A Sub-1 μW multiparameter injectable BioMote for continuous alcohol monitoring”. In: *2018 IEEE Custom Integrated Circuits Conference (CICC)*. IEEE. 2018, pp. 1–4.

[7] S. Dai et al. “A 155-dB dynamic range current measurement front end for electrochemical biosensing”. In: *IEEE transactions on biomedical circuits and systems* 10.5 (2016), pp. 935–944.

[8] L. B. Leene et al. “Autonomous SoC for Neural Local Field Potential Recording in mm-Scale Wireless Implants”. In: *Circuits and Systems (ISCAS), 2018 IEEE International Symposium on*. IEEE. 2018, pp. 1–5.

[9] A. Devices. *AD5940-41 Datasheet*. Oct. 2020.

Chapter 5

SPACEMan: Wireless SoC for Concurrent Potentiometry and Amperometry

5.1 Introduction

This chapter describes the implementation of SPACEMan, a wireless system with concurrent potentiometric and amperometric measurement circuits that can be utilised in the future for saliva, sweat or point of care diagnostics. This system is designed with the vision of simpler interfaces for biofluid analysis. With a complete system-on-chip including electrochemical sensing, power management and data transmission, conventional interfaces like wirebonds will no longer be required in post-processing steps. The results in this work was published in IEEE ISCAS 2021[1], with Yiyang Chen contributing to the simulations of the wireless power blocks in this design, which similarly was published in IEEE ISCAS 2021 [2].

5.2 System Architecture

Fig. 5.1 describes the overall system architecture. A pcb-based 433MHz receiver coil is inductively coupled with a transmitter coil for both power and data transfer. This 3x3mm coil is based on the design by Feng [1], with the frequency chosen for optimal power delivery and specific absorption rate.

A resonant LC (L_R and C_{R1}) tank converts the received power to an AC voltage, which is then converted to a DC voltage through the use of a rectifier. A band-gap reference is then utilised to ensure that the output voltage is constant at 1.2V, before a low-dropout regulator is applied to step the voltage to 1.4V. This power supply is used for a power-on-reset circuit, as well as the front-end sensor. On

[1] **D. Ma**, Y. Chen, S. S. Ghoreishizadeh and P. Georgiou, "SPACEMan: Wireless SoC for Concurrent Potentiometry and Amperometry," 2021 IEEE International Symposium on Circuits and Systems (ISCAS), 2021, pp. 1-5, doi: 10.1109/ISCAS51556.2021.9401312.

[2] Y. Chen, **D. Ma** and P. Georgiou, "A Wireless Power Management Unit with a Novel Self-Tuned LDO for System-On-Chip Sensors," 2021 IEEE International Symposium on Circuits and Systems (ISCAS), 2021, pp. 1-5, doi: 10.1109/ISCAS51556.2021.9401217.

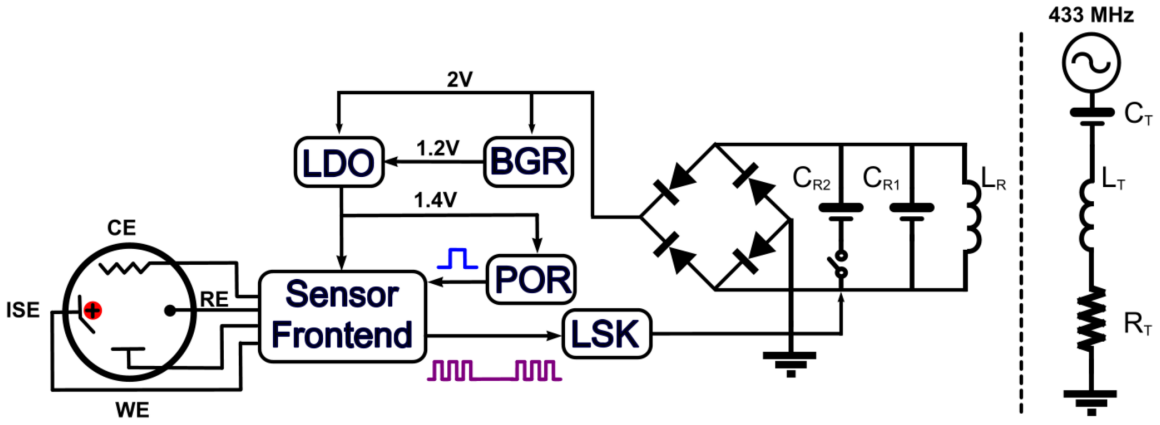


Figure 5.1: System Architecture of SPACEMan, with four electrodes, a sensor frontend, a power management system to supply power wirelessly with a data transmission system for transmitting sensed data. L_R is an external coil not included in SPACEMan's architecture.

power up, the power-on-reset circuit outputs a pulse that adjusts the state of the front-end sensor. The front-end sensor is utilised for concurrent amperometric and potentiometric sensing, and transduces a varying frequency from the sensed current and voltage values. These two frequencies are then mixed with a D flip-flop, before being transmitted via the load-shift keying circuit at the receiver coil.

5.3 Implementation

SPACEMan is implemented in TSMC 0.18μm BCD2 technology with the system broken down to 4 key modules described in this section.

5.3.1 Concurrent Amperometric and Potentiometric Sensing Front End

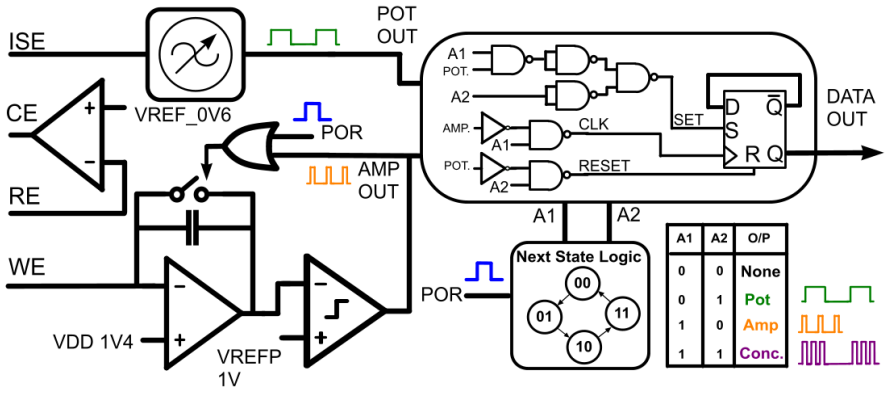


Figure 5.2: DAPPER system architecture for dual amperometric and potentiometric sensing. A state machine implements the possibility of outputting either single potentiometry, amperometry, or concurrent sensing.

The overall system along with the transmitted signals is shown in Fig. 5.2. The front end consists of

five main blocks: (1) A potentiometric circuit consisting of a voltage controlled oscillator and a voltage buffer; (2) An amperometric circuit consisting of a switched-capacitor integrator and a comparator in a feedback loop; (3) A state machine with a SR D-flip-flop for mixing the signals together triggered by the POR; (4) Amplifiers utilised for supplying the counter and the reference electrodes; (5) A POR circuit for starting up the system/changing states when power is received.

The principle of operation is as follows: An amplifier in negative feedback drives CE and RE with a reference voltage. This provides the reference required for both the potentiometric and amperometric circuits. The sensed voltage on the ISE is detected by the potentiometric circuit. A range of input voltage from 0.3V to 1V is converted into a frequency range of 1-9Hz. At the same time, the sensed current input from the WE is detected by the amperometric circuit for an input range of 80pA to 1μA. The switched capacitor integrator and the comparator in a feedback loop converts this current into a frequency range of 400Hz - 400kHz. This circuit is an optimised form of DAPPER presented in Chapter 4 with a lower power consumption of 62% lower power at the cost of reducing input current range from the previous 250pA - 5.6μA range to 80pA - 1μA.

5.3.2 State Machine and Downlink Communication

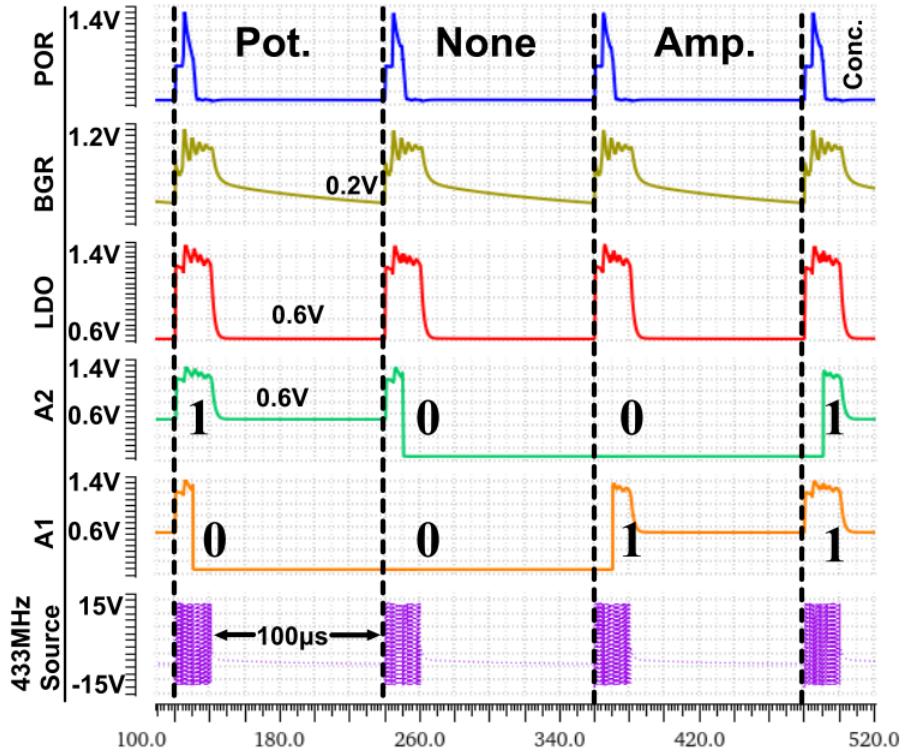


Figure 5.3: Post-layout simulation of how the states are triggered. Pot. refers to potentiometric only, None refers to no output, Amp. refers to amperometric only, and Conc. refers to concurrent output. A 100μs pause in the transmission of the 433 MHz source causes the LDO to drop to 0.6V due to the presence of C_{R1}, that maintains a voltage at the output. The BGR which triggers the POR decreases to 0.2V. When the transmission begins again, the logic high on A1 and A2 goes back up to 1.4V just before the POR pulse triggers the next state.

The introduction of a state machine is utilised to externally control the outputs of the sensor front-

end. This serves to add an additional layer of control to determine the output state of the circuit to be switched between amperometric only, potentiometric only, concurrent output and no output. This is desirable for reconfiguring the circuit for multiple uses. This switching is done through a pulse generated from the POR, and allows the user to switch the output states of the circuit. The truth table shown in Fig. 5.2 describes the output bits for each state. Bits A1 and A2 set the type of output to bel sent to the D flip-flop with set-reset inputs. Based on the set state, the input to the LSK will be (1) POT OUT, (2) AMP OUT halved, or (3) AMP OUT modulated by POT OUT.

The frequencies of signals POT OUT and AMP OUT are chosen to be at least a magnitude of 20$\times$ apart to reduce any errors from mixing the signals. This also allows the user to easily determine the output state of the circuit by looking at the range of frequencies at the LSK. This signal is then transmitted via LSK through to a base-station.

The states are triggered through turning the energy source off for 100 μs as shown in Fig. 5.3. The POR pulses are clocked into a latched logic circuit that changes bits A1 and A2 for varying the states. (1) When the source is off, a 100μs pause causes the BGR voltage to drop to 0.2V. The LDO voltage which powers the circuits goes down to 0.6V, which is followed by the logic bits A1 and A2 if they are in a high state. (2) When the source is switched on, the LDO's fast response time of 100ns ensures that the bits A1 and A2 go up to their logic high voltage of 1.4V. The BGR goes up to 1.2V moments later, triggering the POR pulse to go to 1.4V. This triggers the logic state to switch dependent on the output code. If the circuit is held off for more than 1.47ms, bits A1 and A2 will revert back to logic lows. At that point in time, the charge on C_{R1} is lost - resulting in the logic circuits not retaining the information on the previous state. The next state logic is coded using gray encoding for a simpler state machine, with only an inverter and 2 D flip-flops required for the latching.

Multiple inputs and single channel output systems conventionally utilise downlink techniques such as code-division multiple access (CDMA) or frequency-division multiple access (FDMA). These methods either require decoders or phase-locked loop circuits, which are power intensive. The chosen method employed in this work uses significantly less power due to its simplicity of implementation. However, this chosen method comes with several limitations, namely: (1) The timing of the pauses has to be calculated accurately. Too long, and the state logic circuit will not change. Too short, and the POR pulse will not be high enough to trigger a state change. (2) The circuit is susceptible to process variation. As the timing is key, it is important the POR pulse is triggered when the VDD is back to the normal state.

A POR circuit is applied to provide a pulse for DAPPER to start, as well as trigger the state change circuit. Lastly, stable reference voltages are generated through the use of potential dividers from the 1.4V supply.

5.3.3 Power Management System

The background in Chapter 2 discussed the background behind the various blocks required for wireless power and data transmission. This section would go into the details for the implemented circuits and discuss the rationale behind each chosen design, along with their simulations. The power management

system consists of 3 main blocks: A full-wave bridge rectifier, a high power supply rejection ratio (PSRR) BGR, and a LDO.

5.3.3.1 Rectifier Topology

The bridge rectifier serves the purpose of providing a 2V DC supply voltage from the 433MHz signal. As the process plays a huge role in the efficiency of the rectifier, the topologies for the basic diode-connected, cross coupled, bootstrapped and bulk biased topologies are simulated and compared using TSMC180 technology. Their voltage conversion ratio (VCR) and power conversion efficiency (PCE) is compared to obtain a metric of comparison.

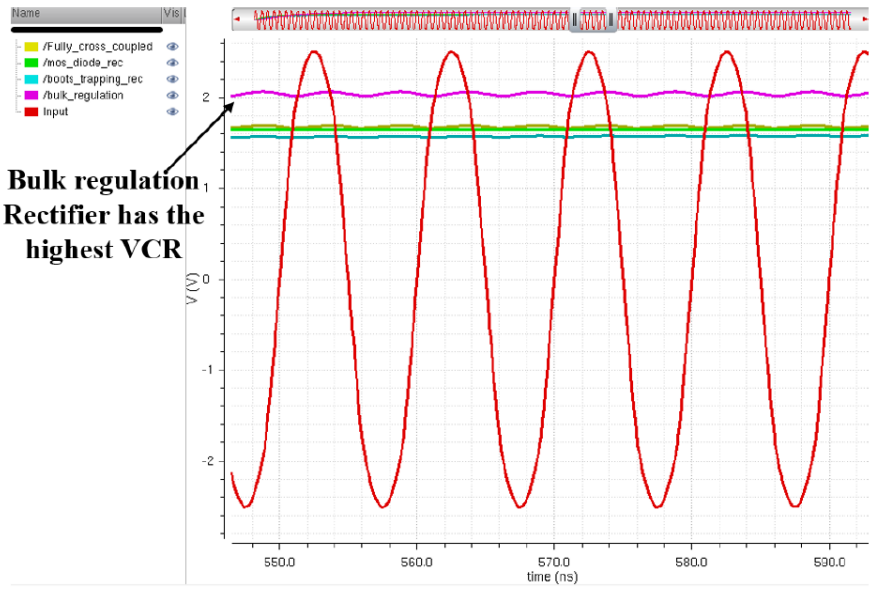


Figure 5.4: Simulation of various rectifier topologies [2]

Fig. 5.4 describes the output simulation for all the 4 rectifier topologies for a fixed transistor sizes of 20μm/250nm. They are driven with a sine wave signal with an expected rms value of 3V and the output voltage is measured. The results are shown in Table 5.1. The bulk regulated rectifier shows the highest VCR, however it was also found that the PTE were all less than 20% at an input frequency of 433MHz.

The TSMC180 package included a schottky diode in its library which was tested. A range of ratios of the width and length of the transistors were simulated to find the sizing that would allow for the maximum PTE and VCR. This was found to be a width of 16 μm and a length of 4μm, with a voltage drop across each diode of 250mV. This is implemented with 4 Schottky diodes with a simulated power transfer efficiency (PTE) of 60%. This was chosen above the other topologies to prioritise PTE.

Table 5.1: Performance Comparison of Various Rectifier Topologies

Type	Vout(V)	VCR(%)
Diode-Connected	1.73	57
Fully Cross-Coupled	1.6	53.4
Bootstrapped	1.4	46.7
Bulk Regulated	2.156	71.87

5.3.3.2 BGR Topology

The BGR circuit has the requirement of supplying a stable reference voltage in the presence of a high supply voltage fluctuation (2.05V - 2.1V) caused by the LSK. The chosen BGR designed for the circuit is inspired by the work in [3]. The four blocks in the circuit are described as the BGR core, opamp, ripple tracking and startup circuitry. The BGR core consists of the standard proportional to absolute temperature (PTAT) circuit from which a two stage opamp amplifies the reference voltage. It achieves a high PSRR of -60dB at 100kHz, with a 1mV output voltage deviation.

The novelty arises from the ripple tracking block, where the output of the opamp is fed into the gate terminals of M1 and M2 through M4 and the diode connected transistor M3. M3 here has a low input impedance $\frac{1}{gm_3}$, which results in the PSRR at the v_g node to be:

$$A_{dd} = \frac{v_g}{v_{dd}} = \frac{r_{ds4}}{\frac{1}{gm_3} + r_{ds4}} \approx 1 \tag{5.1}$$

By tracking the supply ripple and feeding this back into the BGR core, the PSRR is kept high due to the constant drain current and V_{gs} of current mirrors M1 and M2. Lastly, the startup circuit is utilised to keep M1 and M2 in saturation during the power up phase.

It is important to note that the additional ripple tracking stage results in a loss of stability of the circuit due to the opamp now becoming a three-stage opamp. To prevent the circuit from going into positive feedback, the gains at transistors M3-6 are reduced for stability.

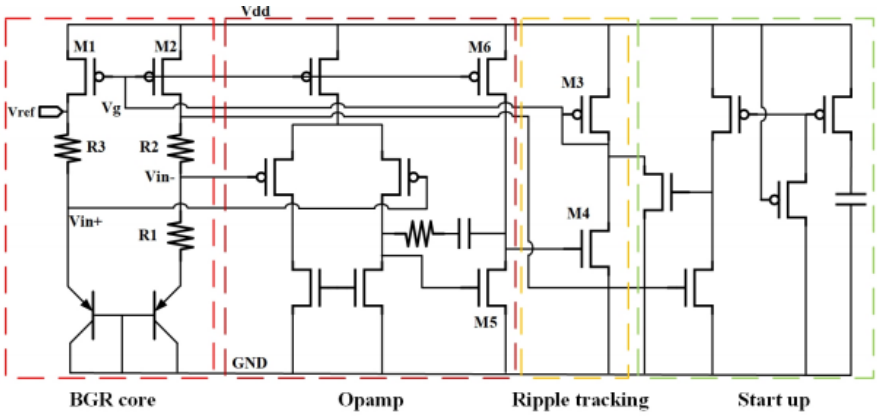


Figure 5.5: Bandgap Reference Circuit used in this work. Taken from [2]

5.3.3.3 LDO Topology

The LDO is used to provide the voltage supply to the system. The proposed circuit is a self-tuning LDO shown in Fig. 5.6 that is capable of dynamically adjusting the current when the input voltage changes and is inspired by [4]. This circuit uses three inputs: the reference voltage, the input unregulated power supply and the LSK signal for tuning the output regulated voltage. The biasing current is increased whenever the a high power consumption is needed - which is synchronised to the output of the system. The steady state current remains low, which allows the power consumption to remain low. The increased current allows for an improvement in the slew rate as seen in Fig. 5.7. As the input voltage decreases from 2.11V to 2.04V, the bias current increases from 100pA to 100muA, allowing the response time to reduce from 1.5μs as seen in the conventional LDO to 100ns for the proposed LDO. The output ripple of the LDO is also reduced to 5mV from 20mV.

This architecture requires a precise synchronisation between the output LSK and input supply, which in practice is difficult to achieve.

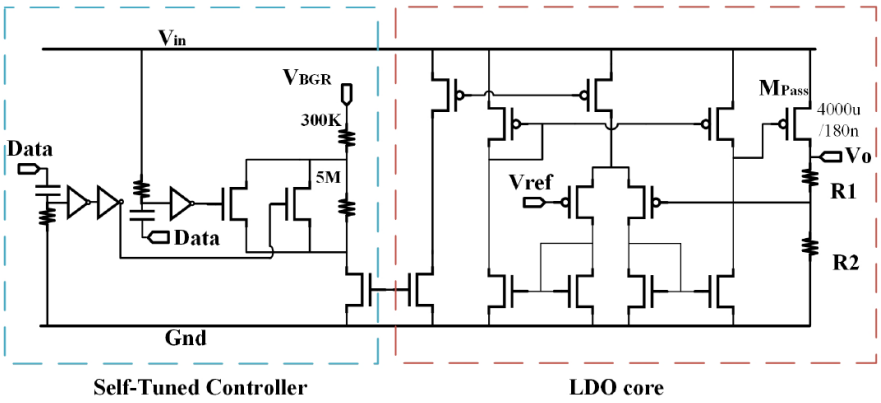


Figure 5.6: Proposed Self-Tuned LDO circuit

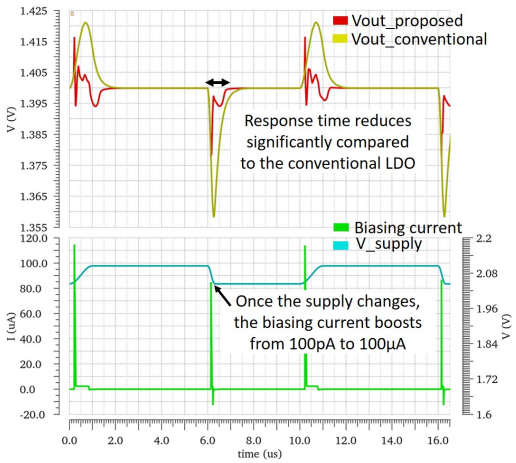


Figure 5.7: Simulated line transient response of the conventional LDO vs self-tuned LDO circuit, with the voltage plot above and current plot below. This displays an improved response time of 100ns from 1.5μs for negative supply variations, and 2μs to 1μs for positive supply variations.

5.3.4 Data Management

The data transmission scheme is chosen as LSK above other known methods due to its simplicity, low area and relatively high power efficiency. The principle behind this circuit is based on shifting the resonant frequency of the LC tank. This can be easily implemented by shorting a parallel capacitor C_{R2}. However, it is important to note the effects of the size of C_{R2} on the system. If C_{R2} is too large, the supply voltage ripple will be high - which lowers the PTE of the system. On the other hand, if C_{R2} is too low, the impedance change will not be high enough to be observed on the transmitter side. A trade-off is chosen between power efficiency and voltage shift.

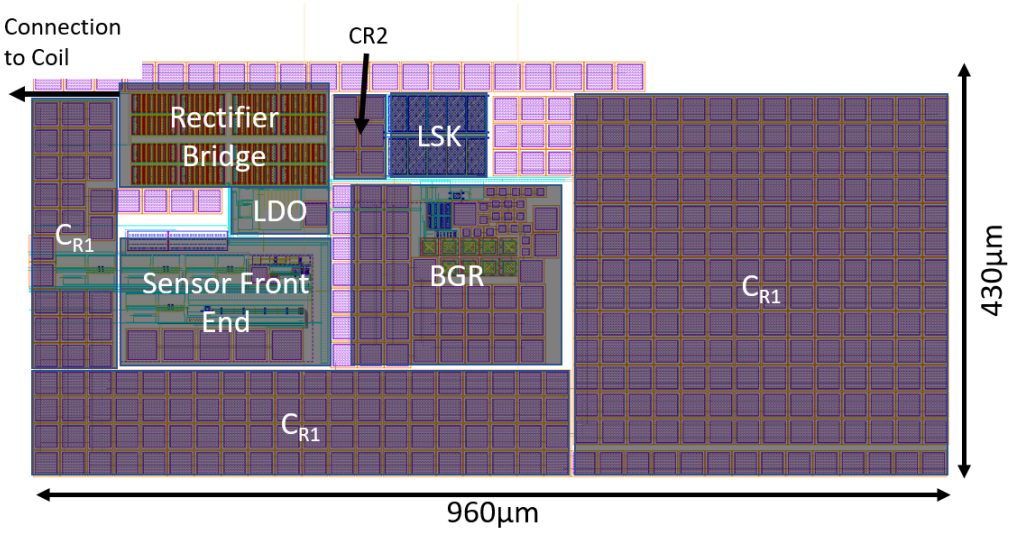


Figure 5.8: Layout of SPACEMan presenting the BGR, LSK, LDO, Rectifier Bridge and Sensor Front End. Note the relative size of C_{R1} compared to the rest of the electronics.

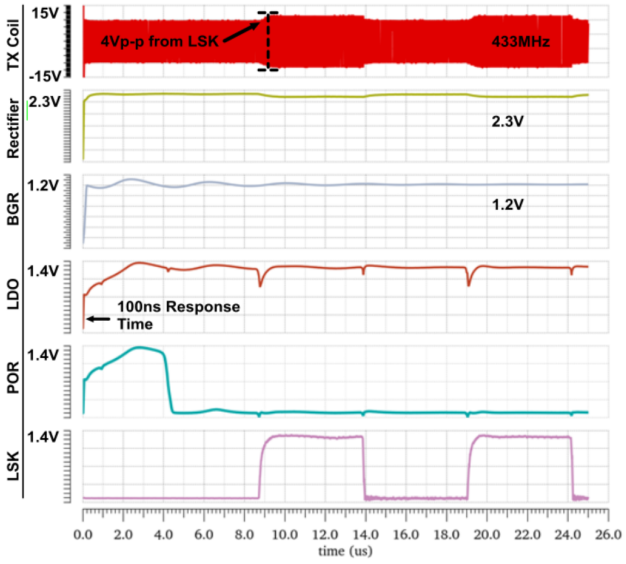


Figure 5.9: Timing Diagram of the first 26μs upon startup showing the most important voltages in the power management circuit at startup. The transmitter coil is driven by a 3V$_{p-p}$ sinewave at 400kHz using a voltage boost and power amplifier previously published in [1]. The coupling factor of the inductive link was set to 0.216 in the simulations in line with [1].

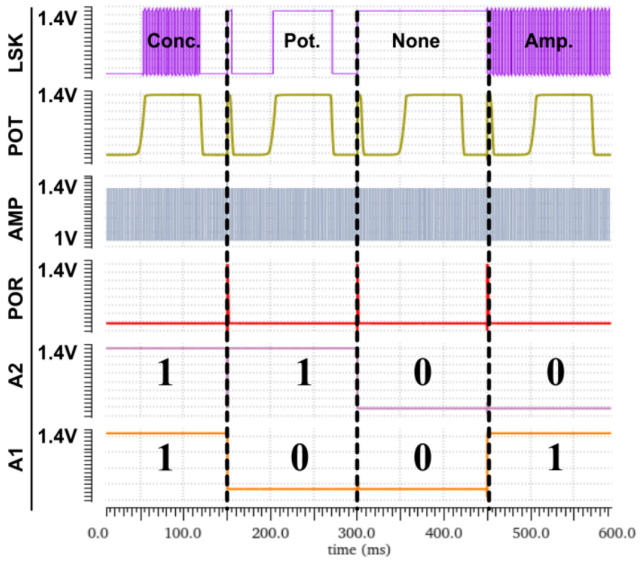


Figure 5.10: Simulated voltage levels at the input and output of the state machine from start up to t=600ms. The following test inputs are used in the simulation setup: input current to amperometry circuit: 80pA. Input voltage to potentiometric circuit: 0.3V. The inductive link connection of the power management circuit is bypassed and instead an ideal voltage source (2V) is used to power on the LDO, BGR, POR, LSK and Sensor Frontend circuits to speed up the simulations.

5.4 Simulation Results

The circuit was designed and simulated on commercially available TSMC 180nm technology. The overall layout presented in Fig. 5.8 shows the core system area of 0.41mm^2.

The amperometric circuit has a linear range for an input of 80pA to 1μA, with an output frequency of 400Hz@80pA to 2.4kHz@1μA. The circuit draws a maximum power of 10.4μW@400kHz. The potentiometric circuit has an input of 0.3-1V based on the possible voltages measured with an IrOx electrode [5]. The linear range of the circuit ranges from 9.27Hz@0.3V to 1.51Hz@1V. This circuit has a maximum power consumption of 4μW@9.27Hz.

Fig. 5.9 describes the process on startup. The Tx coil demonstrates the transmitted 433MHz signal used to power SPACEMan. The transmitted LSK data can be seen as an additional 4V$_{p-p}$ modulation on the transmitted 433MHz signal. This modulated voltage is used to decode the LSK data on the transmitter side. The rectifier transmits a stable 2.3V supply, along with the BGR at 1.2V. The LDO maintains a stable 1.4V supply, although ripples occur at points where the front end sensor transmits a high pulse. The POR circuit showcases a pulse upon startup. This starts up the circuit after a propagation delay of roughly 3.5μs, after which the front-end system begins transmitting the output data through to the LSK circuit.

Fig. 5.10 showcases the input/output characteristics of the state machine up to 600ms. The amperometric and potentiometric circuits transduce their frequencies based on a simulated input of 0.3V (9Hz) and 80pA (400Hz). The inductive link connection is bypassed to provide an ideal 2V source to power on the LDO, BGR, POR, LSK and Sensor Frontend to speed up the simulation. The 4 possible states are described in the figure.

5.5 Measurements

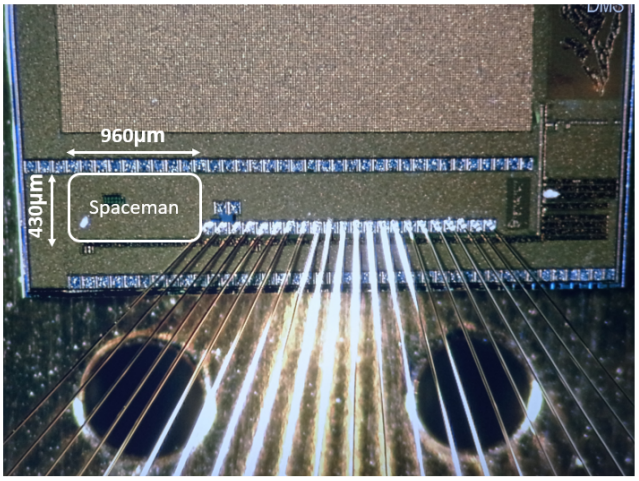


Figure 5.11: Micrograph of Spaceman fabricated in TSMC180BCD technology along with the bonded pads.

Spaceman is fabricated in TSMC 0.18μm BCD2 technology as shown in Fig. 5.11. The chip is wire-bonded to a daughterboard and connected to an external coil on the motherboard similar to Fig. 4.9 in Chapter 4 and shown in the left image of Fig. 5.13.

5.5.1 Experimental Setup

The experimental setup for Spaceman is shown in Fig. 5.12. The signal generator (Rohde & Schwarz SML03) is used to provide a 433MHz signal to the transmitter. The signal generator allows for variations of the frequency(Hz) and power (dB), which is extremely helpful for obtaining the peak resonance frequency of the circuit. The power amplifier(Analog Devices HMC1099) is a specifically chosen for its RF capabilities and can be seen in the left image of Fig. 5.13. This amplifier has a small signal gain of around 18.5dB at a frequency range of 400-700MHz. The supply current for the amplifier is around 100mA at a supply of 28V. Lastly, a PCB fabricated antenna is used for the transmission of the signal.

5.5.2 Electrical Measurements

The first measurements were to observe the minimum distance at which the board can be powered up and with the setup shown in the right image of Fig. 5.13. It was found that the rectifier would output a max voltage at 2.344V at a distance of 4mm, after which the voltage would decrease quickly. At 6mm, the voltage at the output of the rectifier would drop below 1V.

During the measurements, it was found that the output measurement of the LDO was not showing any significant voltage values. The output of the LDO was powering the sensor front-end, which was

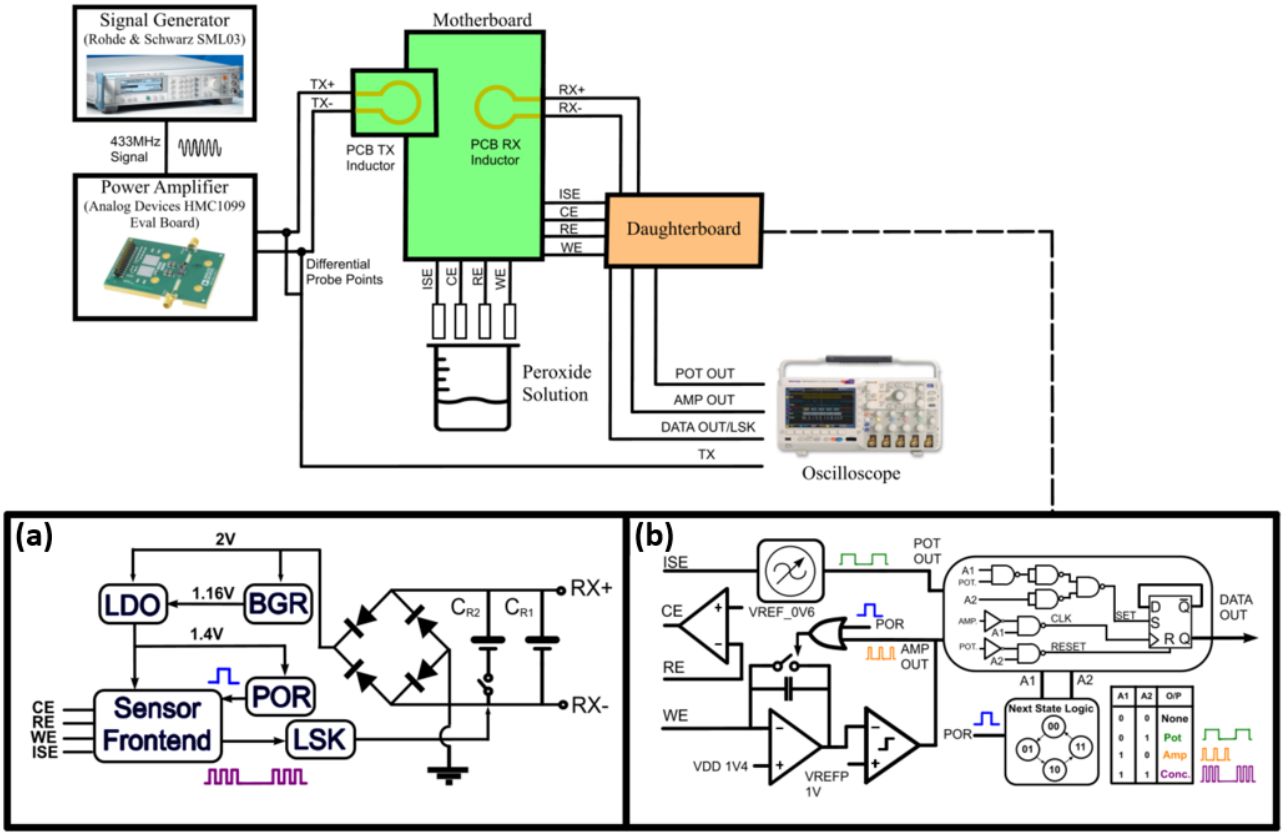


Figure 5.12: Experimental setup for Spaceman consisting of the transmitter. This consists of 3 key equipment: the signal generator, the power amplifier as well as the antenna for transmission.

connected to both the amperometry and potentiometry outputs. The potentiometry output was functioning, however the amperometry output was unable to show any discernible output. Upon further review, this could be due to the re-tweaked integrator reference voltage, that was now connected to the supply voltage (LDO). To circumvent this, an external embedded system was used to recreate the amperometric front end, from which the input was driven into the comparator output test point.

The power supply measurements are shown in Fig. 5.14 with the output voltage of the rectifier and BGR voltage described. The output of the rectifier is 2.344V with a 500mV ripple, while the output of the BGR is 1.12V with a 50mV ripple.

The sensor front-end signals can be seen in Fig. 5.15 and Fig. 5.15. A 0.3V input is driven into the ISE electrode input for an output of 8Hz, while the external amperometric system is driven at 35nA for an output of around 40kHZ. The left image of Fig. 5.15 shows the mixing at the D flip-flop works as expected, while the zoomed in signals in the right image of Fig. 5.15 shows the halving of the amperometry signal after the D flip-flop.

The transmitted 433MHz signal from the rectifier is measured with a differential probe across the antenna coil(RF+ and RF-) to observe the wireless data transmission. The signals observed are shown in Fig. 5.16a, Fig. 5.16b and Fig. 5.16c. The 20kHz signal output from the LSK modulates the TX signal by around 200mV$_{p-p}$. The figures show the LSK transition and also shows a delay of around 80ns before the modulation occurs.

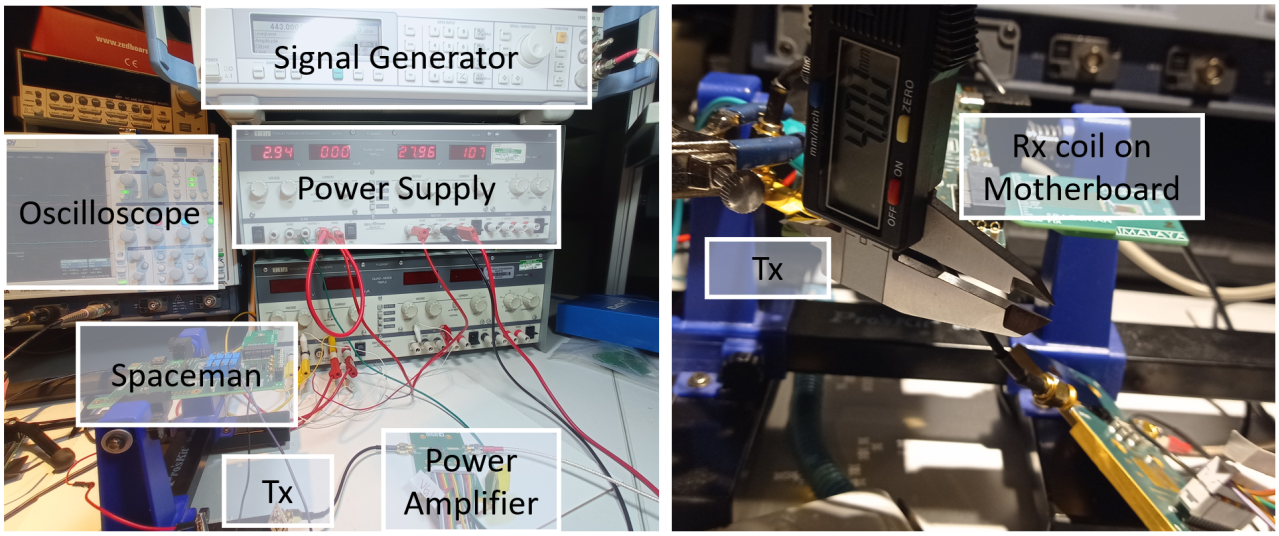


Figure 5.13: Left: Overall Setup of the experiment with the motherboard and Spaceman, the power amplifier and the signal generator. Right: Distance measurements to obtain the furthest possible power-on distance.

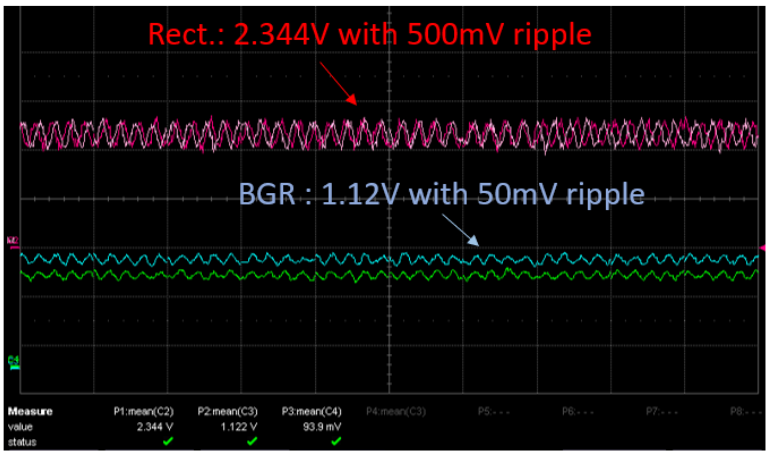


Figure 5.14: Different voltage supplies captured in Spaceman. The rectifier output is shown along with the BGR with a low output ripple. Note that the LDO output voltage is not available.

The booted startup was also tested and observed to work, with the states changing from the amperometric output, potentiometric output, concurrent and no output detected.

5.5.3 Electrochemical Measurements

The system is validated for a wireless potentiometric system, with the ISE output tested for different pH values. An Ag/AgCl reference electrode is used with a voltage of 0.6V is applied at the reference with the output frequency for various pH values shown in Fig. 5.18. The figure shows that the frequency increases fairly linearly for increasing values of the pH. The slight difference in the sensitivity as compared to Tahu is due to some variations in the capacitor sizing of the potentiometric circuit, but is fundamentally the same system.

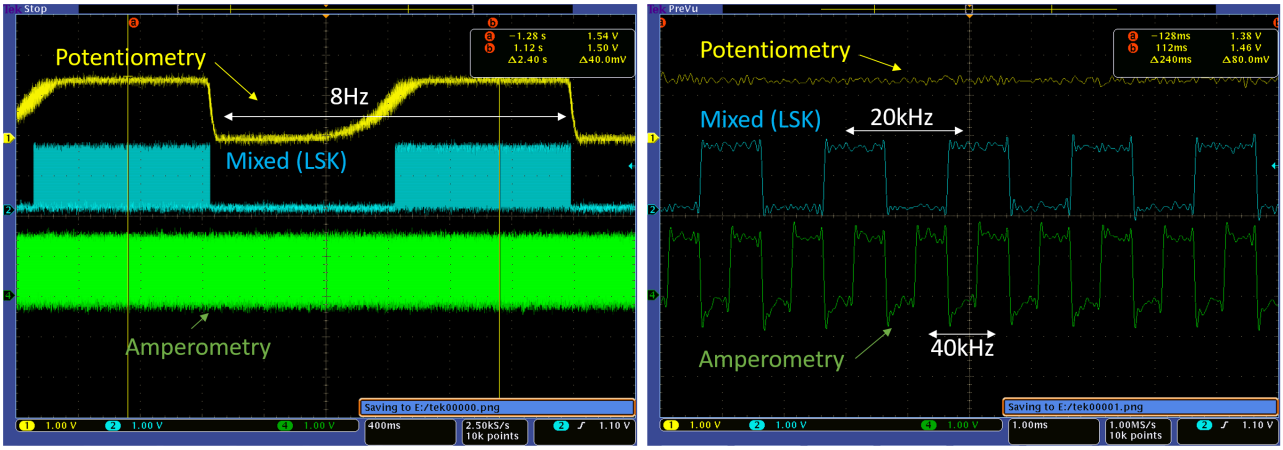


Figure 5.15: Left: Frontend Tests for Spaceman. The amperometric signal is driven by an external embedded circuit, while the potentiometric signal is driven internally by the voltage oscillator. The mixed voltage is fed directly to the load-shift keying. Right:Zoomed-in image of the amperometry and LSK showing the frequency halved by the D flip-flop mixing.

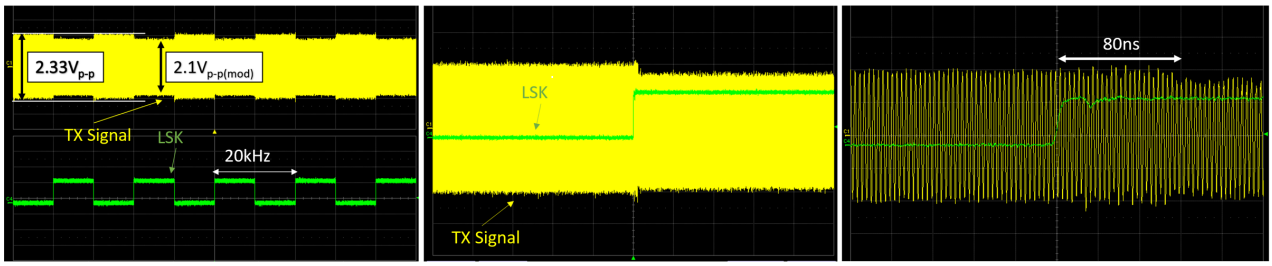


Figure 5.16: A: Measurements taken at the transmitter and the LSK signals showing the LSK modulation of the output signal. B:Zoomed in image of the transition between the low and high phase of the LSK showing the change in the TX signal amplitude. C: Further zoomed-in signal shows that there is a delay of around 80ns before the modulation occurs.

Table. 5.2 compares the system characteristics to other SoC systems. The small size of the core electronics, as well as the simplicity of application makes it particularly versatile compared to other work.

5.6 Chapter Summary

This chapter discusses the development of the three key blocks for the wireless system; the rectifier, the BGR, and the LDO. The mechanisms of the three different circuits are shown in this chapter along with the simulations that support their functionality. The development of the novel self-tuning LDO is also discussed in this chapter. This LDO regulates its power supply based on the output of the system.

This work describes a miniaturised low powered system-on-chip for wireless sensing of potentiometry and amperometry. This system is able to do both sensing techniques at a low power, while transmitting the data wirelessly to a base station. The core focus of this system prioritises the sensor front end, which operates at a low power of 18 μW. A novel downlink system is used to switch the output states,

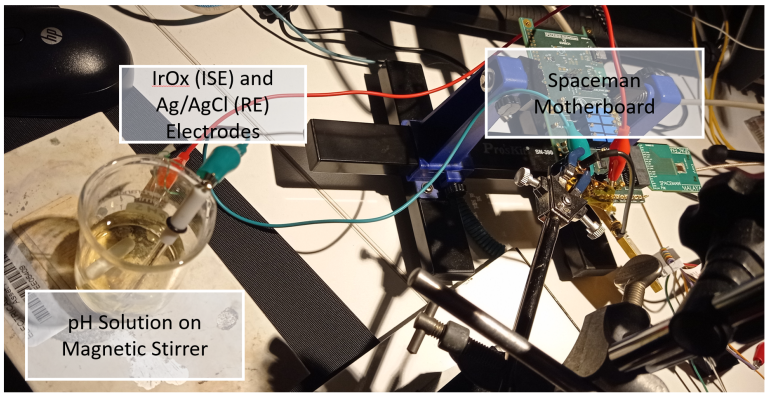


Figure 5.17: Electrochemical Measurement setup showcasing the pH solution under test on a magnetic stirrer, the ISE and RE electrodes connected to the motherboard

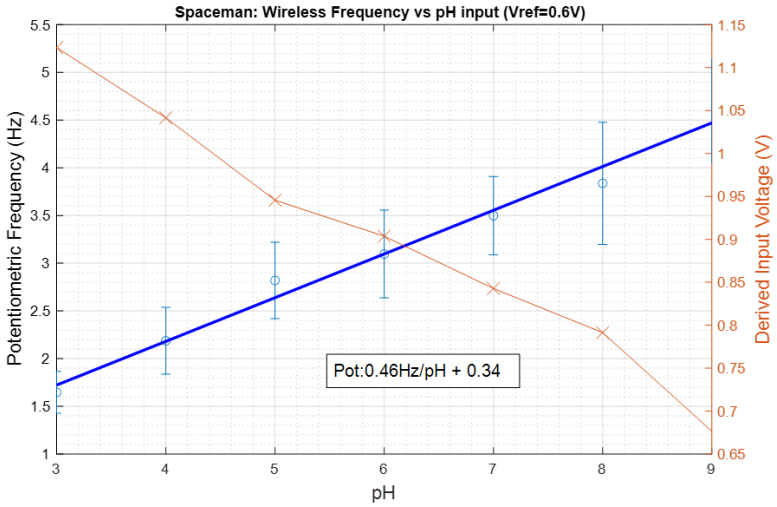


Figure 5.18: Frequency measured at the output of the transmitter of various pH values.

along with a power and data management system for powering the circuits. The simulations provided in this chapter showcase the functionality of the state machine as well as the power-on sequence.

The electrical measurements show the powering on distance as well as the functionality of the wireless power blocks of the fabricated IC. The experimental setup is used to transmit power and obtain transmitted data signals. This is verified and proven in this chapter.

The electrochemical measurements are also taken for the potentiometric output. The output readings are transmitted wirelessly and obtained. This showcases the overall use for the IC as a wireless electrochemical sensor. The versatility and adaptability of this chip makes it a particularly valuable asset in future implementations of wearable devices.

Table 5.2: Comparison of Spaceman with state-of-the-art

Paper	This Work	[6]	[7]
Technology (nm)	180	65	350
Supply (V)	1.4	0.9	1.4
Power (μW)	18	0.97	92
Dynamic Range (dB)	62 (pot.) 87 (amp.)	43(pot.) 30.1 (amp.)	66 (pot.)
Size (mm^2)	0.41	1.275	2.1
Uplink Type	LSK	LSK	LSK
Downlink Type	POR	NA	NA
Trans. Mech.	Amp. & Pot.	Amp. & Pot.	Pot.
Data Rate	400kHz	NA	825Hz

* Amp.= Amperometry, Pot. = Potentiometry, Trans. Mech. = Transmission Mechanism

References

[1] P. Feng. “Completely wireless infrastructure for distributed mm-sized neural implants”. In: *PhD Thesis* (2020).

[2] C. Yiyang. “Body Dust: A Wireless Electrochemical Sensor for In-vivo Glucose and pH Monitoring”. PhD thesis. 2020.

[3] M.-C. Lee and S.-Z. Chang. “Implementation of a High PSRR Low Power CMOS Bandgap Voltage Reference Circuit”. In: *2018 Progress in Electromagnetics Research Symposium (PIERS-Toyama)*. 2018, pp. 2121–2128.

[4] M. Ho and K. N. Leung. “Dynamic Bias-Current Boosting Technique for Ultralow-Power Low-Dropout Regulator in Biomedical Applications”. In: *IEEE Transactions on Circuits and Systems II: Express Briefs* 58.3 (2011), pp. 174–178.

[5] D. Ma, C. Mason, and S. Ghoreishizadeh. “A wireless system for continuous in-mouth pH monitoring”. In: *2017 IEEE Biomedical Circuits and Systems Conference, BioCAS 2017-Proceedings*. IEEE. 2018.

[6] H. Jiang et al. “A Sub-1 μW multiparameter injectable BioMote for continuous alcohol monitoring”. In: *2018 IEEE Custom Integrated Circuits Conference (CICC)*. IEEE. 2018, pp. 1–4.

[7] L. B. Leene et al. “Autonomous SoC for Neural Local Field Potential Recording in mm-Scale Wireless Implants”. In: *Circuits and Systems (ISCAS), 2018 IEEE International Symposium on*. IEEE. 2018, pp. 1–5.

Chapter 6

Conclusion

This thesis looks towards the future of monolithic integration of wireless electrochemical sensors onto a single package. An overview into the various circuits required for the electrochemical configuration, the sensor front-end and the wireless power and data blocks are provided for an evaluation into their use for a monolithic system.

The exploration of a new electrode configuration for concurrently sensing potentiometry and amperometry is explored in this work. The tests show that it is possible to use a shared reference electrode for concurrent sensing, and is applied in the development of the sensor front-end. This gives rise to the possibilities of new electrode configurations for amperometry and potentiometry and allows for a

A novel sensor front-end that is capable of concurrently utilising potentiometry and amperometry is presented in this thesis. The tests show that this design is capable of performing concurrent sensing and is then used to form the basis of the sensor front-end in the final platform. The errors involved in mixing the signals are also properly analysed to understand the trade-offs between the frequency ratio and power consumption of the system.

A final platform with the sensor front-end, wireless power and data transmission along with a state machine is developed. This system is used to show the possibility of sending wireless electrochemical data, and leads to a future where chips could simply be put into packages without any wirebonding required.

6.1 Original Contributions

This work spans a number of different fields, and breaks new ground in some of them. The contributions are summarised as the following:

1. An overview into the basic structures required for a monolithic electrochemical sensor is provided to identify the necessary blocks needed. This background is key to determine the future design of any wireless electrochemical sensor.

2. The theoretical basis for concurrent sensing of amperometry and potentiometry is analysed in great detail, which reveals that potentiometry can still be performed in the presence of cell current. An experiment is designed to empirically determine the differences between concurrent sensing of amperometry and potentiometry against the conventional set-ups which shows that a shared reference electrode set-up could be utilised for electrochemical sensing.

3. The development of a concurrent amperometric and potentiometric circuit with a singular output for backscattering is developed. Prior work in the field has examples of circuits that are capable of potentiometric and amperometric that switch in time, but are not capable of performing both techniques concurrently. The circuit is verified through electrical tests showing its functionality, and electrochemical tests showing its ability to concurrently perform potentiometry and amperometry.

4. This work also discusses the development of a novel wireless block, the self-tuning LDO, and also delves further in-depth on the errors arising from mixing two frequencies on a single channel. The error and power consumption trade-off is shown to be inversely correlated, and an expression for the error is developed. This would be helpful for future designers who utilise low-power data transmission techniques that transmit multiple frequencies on a single channel.

5. The design of an overall system with the wireless power and data management system is completed. The system is used to showcase the wireless powering components and to also display the transmission of sensed data wirelessly. This is the first example of a wirelessly powered electrochemical sensor that is capable of concurrent sensing of potentiometry and amperometry.

6.2 Ongoing Work

There remains ongoing work in progress that extend beyond this thesis.

6.2.1 Integration for in-vivo tests

The current test setup for Spaceman utilises a daughterboard with multiple testpoints in order to validate and characterise each system block on the chip. With the exception of the LDO, the power supply for the BGR and rectifier is working well. Current work involves minimising the footprint of the testboard would be to have a small PCB with a fabricated coil along with testpoints for the potentiometric circuit. The ISE, RE, RF+ and RF- pads are wirebonded onto this PCB, which can be sized down to 2mm by 2mm. This board could be easily integrated into wearable patches or in-mouth platforms for in-vivo tests. Once this is complete, the coil could be fabricated on CMOS for a fully monolithic solution.

6.2.2 Electroplating and Microfludics

Another step in the development would be to develop on-chip sensors for use with the system. Currently, the sensors utilised are in the form of wires or large planar electrodes. Electroplating sensors

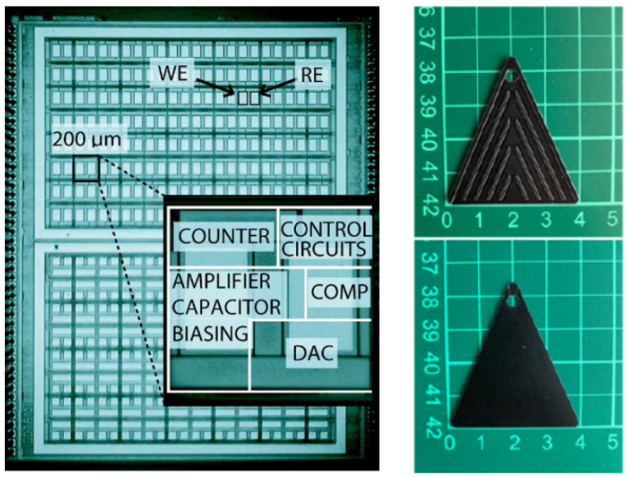


Figure 6.1: Left: CMOS integrated potentiostat developed for on-chip sensing by Nazari et al. Taken from [1]. Right: Soft epidermal sweat patch developed for sweat collection.

on CMOS is an exciting area of research that needs to be explored for future designs. The left image in Fig. 6.1 displays an integrated CMOS potentiostat for on-chip sensing by Nazari et al[1].

Recent work has also been done on a wearable sweat patch with microfludics. This sweat patch is capable of integrating an IC with on-chip sensing capabilities while collecting sweat and can be seen in the right image of Fig. 6.1. This patch directs sweat to a single point, from which a CMOS IC could be used to measure biomarkers. A future application of Spaceman would be to deposit aptamer on gold surface electrodes and utilise the amperometric output for the detection of antibiotics in sweat. This work has been done in collaboration with Wang Tingyu, who completed her MSc project at Imperial in 2022, and is currently undertaken by Li Yiluo, who will be finishing her MSc project in 2022.

6.2.3 Transmitter

Ongoing work has also focused on the development of a portable transmitter for Spaceman. An example setup of the transmitter can be seen in Fig. 6.2. The system consists of the signal generator for a 433MHz output, the previously utilised power amplifier and an antenna for transmission. In addition, a LSK decoder circuit would be used to decode the LSK signals for the frequency, while a bluetooth transmitter would be used to either send these signals to a smartphone app or back to a test platform. This work is currently undertaken by Isabella Breslin, who is finishing her MEng project in 2022.

6.2.4 Platform

The test platform was envisioned to be a Raspberry Pi connected modular system in Fig. 6.3. A Raspberry Pi was chosen in order to make the system accessible and easy to operate for new users. The motherboards that were designed to be interfaced with a raspberry pi. A graphical user interface

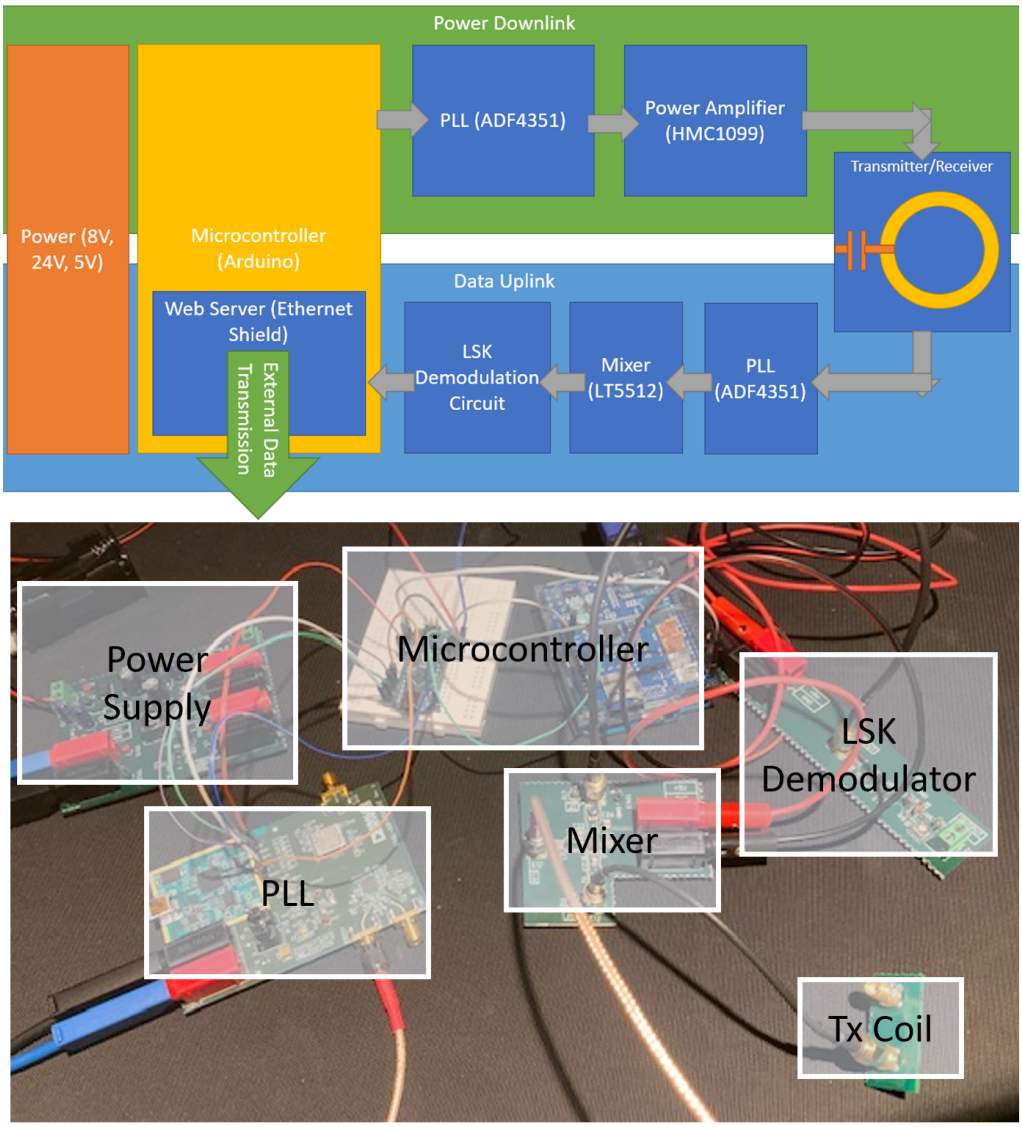


Figure 6.2: Above: System diagram of portable transmitter being developed for Spaceman. This system includes a power downlink consisting of a phase-locked loop and power amplifier, as well as a data uplink consisting of a phase-locked loop, mixer and a LSK demodulation circuit. Below: Individual PCBs being put together for the various parts of the data uplink system.

(GUI) has been developed through the use of digital edge counting in micropython. This is useful to view the measured frequency signals in real-time on a monitor, and also having a portable system that can be moved around quickly.

Future plans include utilising the bluetooth peripherals on the pi to compare the wirelessly transmitted LSK signals from the portable transmitter system in Fig. 6.2 to compare and contrast both signals from each end for debugging. This work is currently undertaken by Xu Yuting, who is finishing his MEng project in 2022.

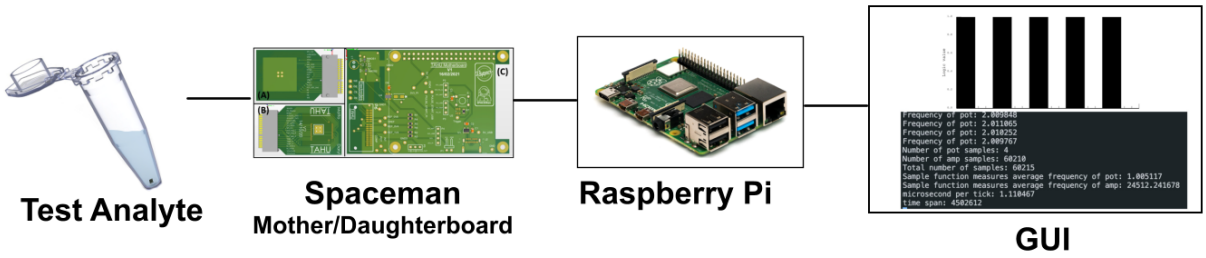


Figure 6.3: Rasperry PI based platform for use with Spaceman Testing

6.3 Final Thoughts

The current industry for mass market wearable devices can be classed into two key areas. The first group are purely electronic devices that measure electrical signals such as Fitbit, Apple Watch or Samsung Health Monitor Smartwatch. These devices rely on CMOS technology such as infrared LEDs and photodiodes for measuring the heartrate, or an accelerometer to monitor your walking pace or to report an accidental fall. These devices rely on the reliability and reproducibility of these electronic sensors to mass produce these wearable devices at scale.



Figure 6.4: Dexcom G6 glucose sensor starter kit from [2].

The second group of wearable devices are sensors that utilise a form of chemical testing that measures

either saliva, sweat or interstitial fluid. An example would be the Dexcom G6 that utilises interstitial fluid to monitor the glucose level of a patient. These sensors can be used for up to 10 days and consist of a wired sensor that is inserted into the patient. These sensors require a specific inserter to inject the sensor into the patient. The overall market price for the starter kit seen in Fig. 6.4 is £159 for 3 sensors and an applicator, along with a transmitter for a month's usage.

Mass production of electrochemical sensors that are reliable at an effective cost price would allow for a closer step towards affordable diagnostics kits for the common man. This would mean the possibility of measurements of biomarkers at the fingertips of every user, allowing for a range of treatments to be done at the point-of-care and by the individual. To achieve this, these electrochemical sensors must be reliable, easily reproducible, with simplified post-processing required for reduced cost of production.

This thesis has looked into the development of one such electrochemical sensor. The approach has been to utilise the reproducibility of CMOS manufacturing and reducing post-processing by removing the need for wirebonding the CMOS ICs onto PCBs. However, there remains more work needed to ensure that such a sensor is utilised.

First, the development of a reproducible process for depositing the required electrodes onto the surface of the CMOS is needed to ensure that the sensors can be manufactured at scale. The calibration of the sensors should ideally be done in the same process wirelessly. An example would be to selectively deposit material on the surface, before placing the IC in a solution for wireless calibration. Once this is complete, the sensors can be used in a multitude of environments.

Second, an investigation into the noise levels of these sensors at such sizes has to be investigated. Smaller CMOS sensors are helpful to lower the cost of manufacturing as well being easily embedded into wearable devices. However, this also means that the measurement region for the biomarkers would likely be in the pA - μA or pV - μV ranges. At these levels, it is likely that noise would become a larger factor in obtaining the biosignals. To circumvent this, it is important to characterise the possible noise at these sensor sizes, and develop effective filtering methods to obtain the true signal.

These two research areas would be extremely key fields to enhance the state of wearable devices in the future, and would impact the nature of our interaction with medical devices forever.